Dijet Photoproduction at High Transverse Energies

Joost Vossebeld

Dijet Photoproduction at High Transverse Energies

Dijet Photoproduction at High Transverse Energies

ACADEMISCH PROEFSCHRIFT

ter verkrijging van de graad van doctor
aan de Universiteit van Amsterdam
op gezag van de Rector Magnificus
Prof. Dr. J. J. M. Franse
ten overstaan van een door het college voor promoties ingestelde
commissie, in het openbaar te verdedigen in de Aula der Universiteit
op dinsdag 7 september 1999 te 13.00 uur

door

Joost Herman Vossebeld
geboren te Haaksbergen

Promotor: Prof. Dr. J. J. Engelen
Co-Promotor: Dr. H. G. J. M. Tiecke

Faculteit der Wiskunde, Informatica, Natuur- en Sterrenkunde

The work described in this thesis is part of the research programme of 'het Nationaal Instituut voor Kernfysica en Hoge–Energie Fysica (NIKHEF)' in Amsterdam, the Netherlands. The author was financially supported by 'de Stichting voor Fundamenteel Onderzoek der Materie (FOM)', which is funded by 'de Nederlandse Organisatie voor Wetenschappelijk Onderzoek (NWO)'.

Contents

Chapter 1

Introduction

Processes governed by the strong or nuclear force behave very differently from those governed by other forces. This is largely due to the remarkable feature that the coupling between strongly interacting particles is large when these objects are separated by a large distance and weak when the distance is small. This behaviour is reflected in the running of the strong coupling constant, α_s, which is small at short distances and big at large distances.

For high energy scattering it is, in general, not possible to calculate exactly the cross section of a given process. At present, the best tool available to perform calculations, is a perturbative expansion in powers of the coupling constant, of the interaction under consideration. For the electromagnetic and weak forces, where the coupling constants are much smaller than 1, this technique allows for calculations of cross sections with a phenomenal precision. In strong interactions, however, when the distance between the interacting particles is large, the coupling constant α_s is large and the perturbative expansion breaks down. This means that long range strong correlations are not calculable. As a consequence, the confrontation of quantum chromodynamics (QCD), the theory that governs the strong interaction, with experimental results is complicated. Measurements have to be defined in such a way, that the sensitivity to long range correlations is small. This requires great care in the definition of measurements and in their interpretation.

A typical QCD process that can be measured, e.g. at the HERA ep collider in Hamburg, is the photoproduction of jets, $\gamma+p \longrightarrow jet(s)+X$, where the quasi real photon has been radiated from the electron beam. Two processes contribute: the direct process in which the photon couples directly to a parton inside the proton and the resolved process where the photon acts as a source of partons, one of which scatters off a parton in the proton. The photoproduction of jets is governed by both the electromagnetic and the strong force. As electromagnetic interactions are well understood, the confrontation of jet photoproduction measurements with QCD predictions, constitutes a quantitative test of this theory and yields information on the partonic structures of the proton and the photon.

This thesis presents a study of photon-proton interactions[1] with two high transverse energy jets in the final state. We use a sample of ep interactions recorded with the ZEUS detector in 1995 and corresponding to an integrated luminosity of 6.3 pb^{-1}. The dijet photoproduc-

[1]The analysis presented in this thesis has been published in [1]. Initial results from an analysis, similar to the one presented in this thesis, have been presented in [2].

tion cross section, which is measured as a function of the transverse energies and the angles of the jets, is confronted with next-to-leading order quantum chromodynamics (NLO QCD) predictions.

In addition, at the end of this thesis preliminary results are presented of an ongoing analysis using data collected in 1996 and 1997. These data correspond to a larger luminosity than the data collected in 1995 and will be used to extend the study of dijet photoproduction to higher transverse energies of the jets.

Chapter 2

The physics of hadrons

The idea that hadrons are particles composed of smaller entities emerged in the sixties when it was shown that the many baryons and mesons, known at that time, could be classified according to the naïve quark model proposed by Gell-Mann and Zweig [3, 4]. This model is based on the SU(3) symmetry group and states that hadrons are built up from quarks that come in three different flavours. The three quark flavours correspond to the fundamental representation of the SU(3) group. Baryons are considered to be three-quark states while mesons are quark-anti-quark states. The SU(3) symmetry in the quark model is not an exact symmetry, indicated by the fact, for example, that hadrons belonging to the same irreducible representation, have different masses. A big success was the observation of the Ω^- baryon [5], of which the quark model predicted the existence. In the framework of the quark model, the Pauli exclusion principle leads to the need for a new quantum number. This can be seen from the Ω^- for example, which consists of three quarks with identical flavours and with their spins aligned. This situation is forbidden by the Pauli principle unless another quantum number exists, that makes the wave function of the Ω^- again anti-symmetric under the exchange of two quarks. This new quantum number, called colour, has led to the formulation of the theory of quantum chromodynamics (QCD) [6], that governs the strong or nuclear force. QCD is a non-Abelian Yang-Mills gauge theory that describes the force between coloured particles. Like the quark model, the theory of QCD is based on the SU(3) symmetry group, where in this case, the fundamental representation of the symmetry group corresponds to three colours. The symmetry of colour is an exact symmetry. The vector bosons that exchange the colour force are called gluons.

In 1971 experiments by a SLAC/MIT collaboration [7] showed that the cross section for deep inelastic lepton-hadron scattering, in the region where resonances no longer play a role, is, within experimental uncertainties, independent of the momentum transfer in the interaction, if the standard dependence due to the photon propagator is taken into account. This property, called scaling, had been predicted by Bjorken [8] and leads to models in which hadrons are built up from free pointlike constituents, referred to as partons. These partons could be identified with the quarks introduced by Gell-Mann and Zweig.

2.1 Quantum chromodynamics

For a detailed introduction to the theory of QCD an extensive literature is available [9]. In this section only its main aspects and implications are discussed. An important feature of QCD is the charge screening behaviour in this theory. This behaviour is opposite to the screening behaviour of e.g. the electromagnetic force. For an electron, due to vacuum polarisation, the effective charge decreases with increasing distance. For a coloured particle exactly the opposite occurs. The effective colour charge is small at short distances and increases when the distance becomes larger. This property is called anti-screening and explains the notions of asymptotic freedom and colour confinement, i.e. the existence of relatively free quarks inside hadrons that are nevertheless confined to these hadrons.

2.1.1 The running coupling constant

The properties of asymptotic freedom and colour confinement are described, quantitatively, by the running of the effective strong coupling constant α_s, which decreases with increasing momentum transfer and increases with decreasing momentum transfer. In lowest order the running of α_s is described by the formula:

$$\alpha_s(\mu_r^2) = \frac{12\pi}{(33 - 2N_f) \ln \frac{\mu_r^2}{\Lambda_{QCD}^2}}, \tag{2.1}$$

where μ_r is the renormalisation scale, which is usually taken to be the momentum transfer in the interaction, N_f is the number of active quark flavours in the interaction and Λ_{QCD} is a parameter that has to be determined experimentally. The formula shows that α_s decreases when μ_r is large and increases when μ_r becomes small. Large values of μ_r correspond to short distance interactions and small values of μ_r to large distance interactions. From the formula it is clear that only when $\mu_r^2 \gg \Lambda_{QCD}^2$ the coupling constant is much smaller than 1 and perturbation theory becomes applicable. For smaller values of μ_r^2 the perturbative approach breaks down. There are possibilities to extend QCD calculations to lower scales μ_r^2 by a resummation of important diagrams to infinite order. For very low μ_r^2 values, however, no method of performing realistic calculations is available as yet.

2.1.2 The dynamics of QCD interactions

QCD processes in which a hard scale is involved, i.e. short distance interactions, are calculable in perturbative QCD. In real life, these short distance interactions are always accompanied by large distance interactions, which are not calculable. In a hard QCD scattering process for example, there are always soft processes in the initial and final state that ensure that the incoming and outgoing particles are colour neutral at large distances.

In figure 2.1 a schematic picture is given of the processes that play a role in a typical interaction governed by the strong force. In this case the interaction is between two hadrons. The basic picture is that of a parton inside hadron A interacting with a parton inside hadron B. The outgoing partons fragment into hadrons in the final state.

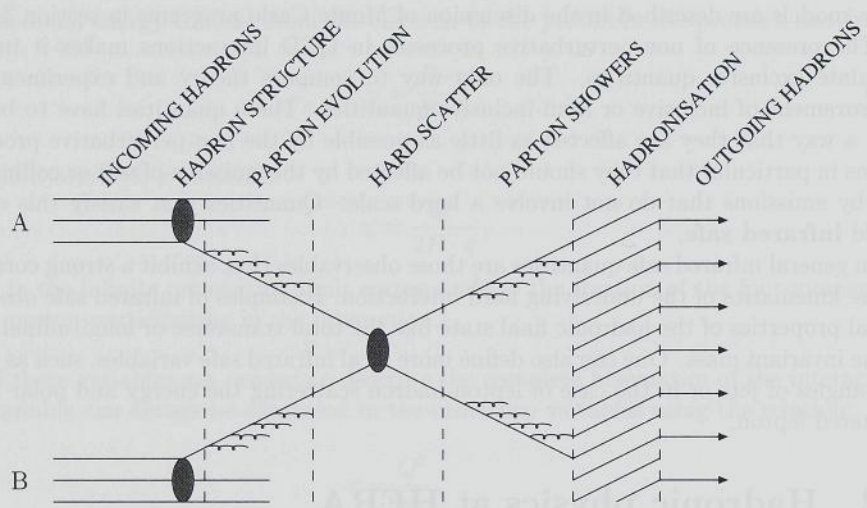

Figure 2.1: Schematic representation of the processes involved in a typical hard QCD interaction.

To understand these processes in terms of QCD it is interesting to see how the different aspects of the interaction are dealt with in QCD calculations.

The **parton density functions (PDF's)** of hadrons, often denoted as $f_p^{hadron}(x, \mu)$, represent the number of partons inside the hadron carrying a fraction x of the hadronic momentum when the hadron is probed at a given scale μ. Hadronic PDF's are not calculable a priori in terms of QCD. They have to be determined experimentally. QCD does predict, however, how the PDF's evolve as a function of the scale at which the hadron is probed. This evolution is governed by the DGLAP [10] **parton evolution** equations, that incorporate the probability of a quark to split into a quark and a gluon and of a gluon to split into a quark and an anti-quark or into a gluon pair. The calculation of the evolution of parton densities using splitting functions, is in effect a resummation of the dominant terms in the perturbative expansion, which are the terms containing large logarithms of μ^2, to infinite order in α_s.

The evolution equations are used to evolve parton density functions, which have been determined for a certain input scale μ_0, up to the factorisation scale, μ_f, which is the scale that separates the structure of the hadron from the hard interaction. μ_f is usually taken equal to the momentum transfer in the hard interaction.

The **hard interaction** itself involves a hard scale and can therefore be calculated in a fixed order perturbative expansion. The partons that are produced in the hard interaction will emit more partons. As long as the transverse momentum involved in these emissions is sufficiently high the **parton showers** are calculable, similar to the parton evolution in the initial state, by a resummation of dominant logarithmic terms to infinite order in α_s.

Finally the partons in the final state have to form hadrons again. This process, referred to as the **hadronisation** stage, involves no hard scale and is not calculable. At present only phenomenological models exist to describe the hadronisation of partons into hadrons. Two of

these models are described in the discussion of Monte Carlo programs in section 3.3.1.

The presence of non-perturbative processes in QCD interactions makes it impossible to calculate exclusive quantities. The only way to compare theory and experiment is via the measurement of inclusive or semi-inclusive quantities. These quantities have to be defined in such a way that they are affected as little as possible by the non-perturbative processes. This means in particular that they should not be affected by the emission of soft or collinear partons, i.e. by emissions that do not involve a hard scale. Quantities that satisfy this criterion are called **infrared safe**.

In general infrared safe quantities are those observables that exhibit a strong correspondence to the kinematics of the underlying hard interaction. Examples of infrared safe observables are global properties of the hadronic final state like the total transverse or longitudinal momentum or the invariant mass. One can also define more local infrared safe variables, such as the energies and angles of jets or in the case of lepton-hadron scattering the energy and polar angle of the scattered lepton.

2.2 Hadronic physics at HERA

There is a rich field of hadronic physics that can be studied at an ep collider like HERA. Some of these topics are discussed below.

2.2.1 Deep inelastic ep scattering

Without making any assumptions about the underlying physics, deep inelastic electron-proton scattering [1], $ep \longrightarrow eX$, can be schematically depicted as in figure 2.2

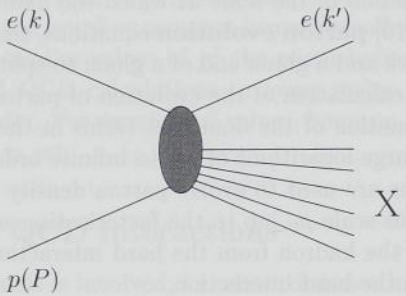

Figure 2.2: Generic diagram of deep inelastic electron-proton scattering.

To describe the kinematics of a deep inelastic ep scattering event 3 variables are used:

- the negative squared four-momentum transfer from the electron to the proton

$$Q^2 = -q^2 = -(k - k')^2 , \tag{2.2}$$

[1] For the purpose of simplicity, in this section, we shall refer to electrons, when we mean electrons or positrons.

- the fractional energy transfer from the electron to the proton in the proton's rest frame

$$y = \frac{P \cdot q}{P \cdot k}, \tag{2.3}$$

- and the Bjorken [8] x variable:

$$x = \frac{Q^2}{2P \cdot q}, \tag{2.4}$$

which in the infinite momentum limit corresponds to the fraction of the four-momentum of the proton participating in the interaction.

Only two of these variables are needed to describe the complete kinematics of the interaction. The third variable can always be expressed in the other two variables using the relation:

$$x = \frac{Q^2}{ys}, \tag{2.5}$$

where s is the squared centre-of-mass energy of the ep system.

The cross section for deep inelastic ep scattering can be written as:

$$\frac{\mathrm{d}^2\sigma(e^{\pm}p)}{\mathrm{d}x\mathrm{d}Q^2} = \frac{4\pi\alpha^2}{xQ^4}\left[y^2 x F_1^p + (1-y)F_2^p \mp (y - \frac{y^2}{2})xF_3^p\right]. \tag{2.6}$$

The structure functions, F_1, F_2 and F_3, can be interpreted in terms of the parton density functions of the proton. Although, as we discussed above, parton density functions of hadrons are not calculable, QCD does predict how they evolve with the scale at which the hadron is probed, in this case Q^2. An interesting feature of the DGLAP [10] parton evolution equations is that they predict a violation of the scaling behaviour expected in the free parton model. This scaling violation is due to the radiation of gluons, which in turn fluctuate into more gluons and into quark anti-quark pairs. This effect depletes the quark densities at high x and increases them at low values of x. Scaling violations have been observed experimentally.

The extension of the measurement of the structure functions of the proton, in particular of F_2, over a large kinematic range, is one of the physics goals of HERA. The confrontation of these measurements with parton evolution equations constitutes a thorough test of the dynamics of perturbative QCD.

A related field of study at HERA is that of charged current deep inelastic scattering. In charged current interactions the exchanged boson is a W boson and the lepton in the final state is a neutrino. Charged current interactions at HERA can provide complementary information on the quark densities in the proton.

2.2.2 Photoproduction

In an ep collider like HERA the electron beam is accompanied by quasi real photons that travel collinear to the beam. Interactions of these photons with the protons form an additional field

of study at HERA. The probability that an electron radiates a photon with given virtuality Q^2 and fractional energy z is given by the Equivalent Photon Approximation (EPA) [11]:

$$f_\gamma^e(z, Q^2) = \frac{\alpha_{em}}{2\pi Q^2}\left[\frac{1+(1-z)^2}{z} - 2\frac{1-z}{z}\frac{Q^2_{min}}{Q^2}\right], \tag{2.7}$$

where the Q^2_{min} is the lowest virtuality that can be obtained:

$$Q^2_{min} = m_e^2\frac{z^2}{1-z}. \tag{2.8}$$

For photoproduction events, i.e. for photon-proton interactions where the photon is quasi-real, the photon spectrum can be calculated by integrating the EPA equation from the minimum to the maximum Q^2 value attainable. This is known as the Weizsäcker Williams Approximation (WWA) [11]:

$$f_\gamma^e(z) = \frac{\alpha_{em}}{2\pi}\left[\frac{1+(1-z)^2}{z}\ln\frac{Q^2_{max}}{Q^2_{min}} - 2\frac{(1-z)}{z}\left(1 - \frac{Q^2_{min}}{Q^2_{max}}\right)\right]. \tag{2.9}$$

In photoproduction the hard scale of the interaction is given by the transverse energy of the outgoing partons. In leading order perturbation theory, two processes contribute to the photoproduction of jets: the direct process in which the photon couples directly to a parton in the proton and the resolved process where the photon acts as a source of partons, one of which scatters off a parton in the proton. These processes are schematically depicted in figure 2.3. The signature of the two processes differs in the presence of a photon remnant in resolved events. Beyond the leading order direct and resolved processes are no longer distinctly separable.

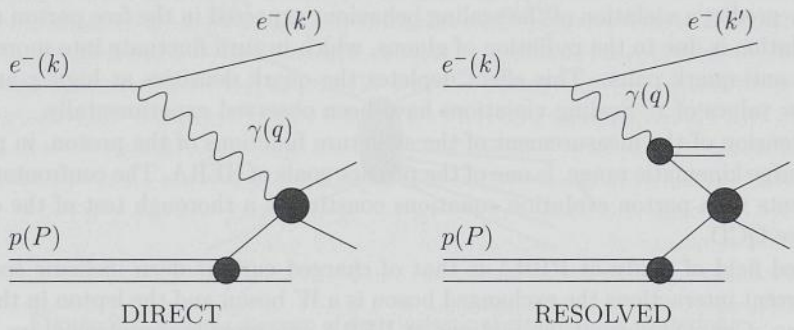

Figure 2.3: Generic diagrams of direct and resolved photoproduction.

The resolved process occurs because the photon can exhibit a hadronic structure. The cross section for photoproduction is thus sensitive to the hadronic structures of both the proton and the photon.

2.3 The hadronic structure of the photon

The electromagnetic coupling of the photon to charged particles allows it to fluctuate into a quark anti-quark ($q\bar{q}$) pair. In an interaction between a photon and another particle, that is sufficiently hard to make the interaction time comparable to, or even shorter than, the typical lifetime of a $q\bar{q}$ fluctuation of the photon, there is a chance that the hard interaction is not with the photon as a whole, but rather with a parton inside the photon. The partonic structure of the photon can be separated in two contributions, following from the fact that the photon can couple both to bound and unbound $q\bar{q}$ pairs.

- When the photon couples to a bound $q\bar{q}$ state, this state must have the same quantum numbers as the photon. Such states are the light vector mesons: ρ, ω and ϕ. The process is referred to as vector meson fluctuations of the photon. Because the mesons have low masses these fluctuations cannot be calculated in perturbation theory. It turns out they can be described rather well by the phenomenological Vector meson Dominance Model (VDM) [12].

- The coupling of the photon to an unbound $q\bar{q}$-pair adds an extra component to the partonic structure of the photon, which is called the anomalous component. This anomalous component is particularly interesting since it is in principle calculable in perturbative QCD.

Like for hadrons, the structure of the photon can be evolved with the probing scale μ using parton evolution equations, in which one additional term appears that accounts for the splitting of the photon into a $q\bar{q}$ pair. The partonic structure of the photon gained much interest when in 1977 Edward Witten [13] argued that, in the framework of perturbative QCD, the deep inelastic structure functions of the photon behave very differently from the structure functions of hadrons. As stated earlier, the structure functions of hadrons cannot be known a priori, but have to be determined from experiment. Only the behaviour as a function of the probing scale, i.e the scaling violation, is calculable. The structure functions of the photon, at large enough scales for the VDM component to play no role, are completely determined. In particular, unlike hadronic parton densities, they peak at fractional momenta near 1. The scaling behaviour of the photon is also very different from that of hadrons. Due to the fact that the parton densities of the photon are fed by the $\gamma \longrightarrow q\bar{q}$ splitting process, the parton densities in the photon rise slowly as a function of the scale [14].

Precise knowledge of the partonic structure of the photon is of great interest. First of all as a test of perturbative QCD, since this knowledge imposes constraints on different QCD inspired approaches used to produce parametrisations for the parton density functions in the photon. Secondly because more precise knowledge of the partonic structure of the photon improves the accuracy of theoretical predictions for various processes.

2.3.1 Photon structure at e^+e^- colliders

Currently most of our knowledge on the hadronic structure of the photon comes from e^+e^- experiments where deep inelastic $e\gamma$ scattering is studied. The measurement of F_2^γ is a direct

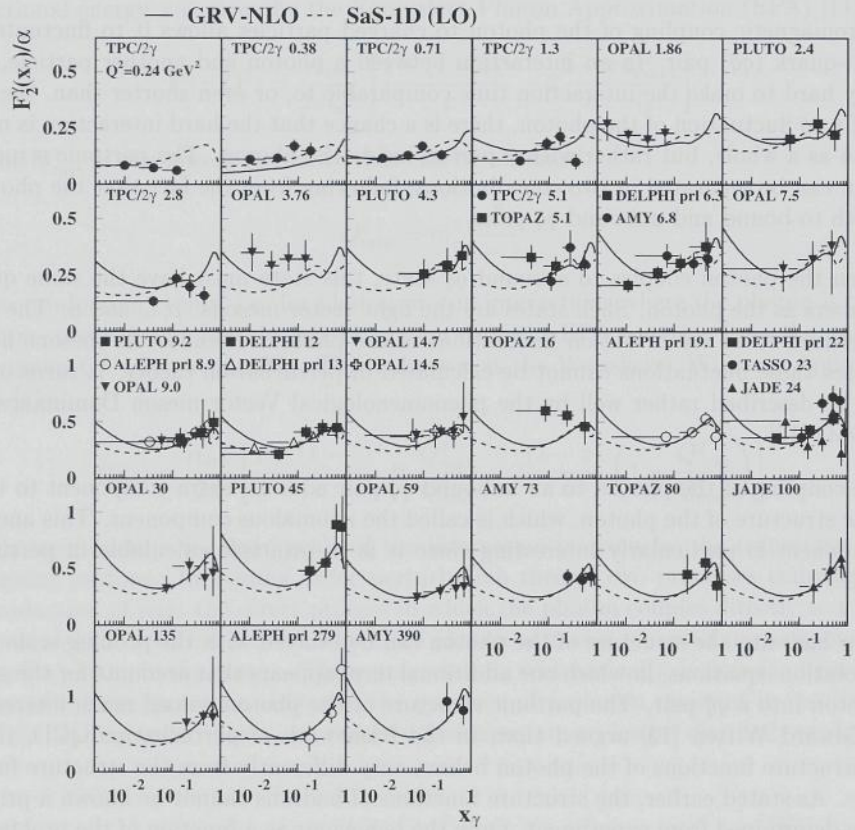

Figure 2.4: Compilation of the available experimental data on F_2^γ as a function of x_γ for increasing Q^2 values. Taken from [15].

measurement of the quark densities in the photon. In figure 2.4 a compilation of F_2^γ measurements from various e^+e^- experiments [16, 17, 18, 19] is shown. The data cover a range in Q^2 from 0.24 to 390 GeV^2 and in x_γ from 0.001 to 1. At x_γ values above 0.5 experimental uncertainties are large and the structure function F_2^γ is not strongly constrained.

In leading order, deep inelastic $e\gamma$ scattering is only sensitive to the quark densities in the photon. The gluon density which dominates the photon structure at low x_γ is not constrained very much by these data.

2.3.2 Photon structure at HERA

Jet photoproduction measurements at HERA have the potential to provide new information on the photon structure in the regions that are hard to measure in e^+e^- scattering experiments.

The gluon density

In comparison to F_2^γ measurements in e^+e^- experiments, jet photoproduction has a direct sensitivity to the gluon density in the photon, since it contributes already at leading order to the cross section. For protons the gluon density can be determined from the scaling violations of F_2, in combination with the momentum sum rule. For photons, however, because of the presence of the direct contribution, no simple momentum sum rule applies and the determination of the gluon density from F_2^γ data becomes very difficult. In jet photoproduction measurements there is a direct sensitivity to the gluon density in the photon. This sensitivity is concentrated at low x_γ values where the gluon content of the photon dominates the cross section. This corresponds to relatively low transverse energy jets at very forward angles. Due to non-perturbative effects this is a very difficult region to interpret measured cross sections. The measurement of jet photoproduction involving heavy (charm) quarks is more promising in this respect, since in resolved photoproduction events containing a charm quark, non-perturbative effects are expected to be suppressed because the charm mass provides an extra hard scale. In addition, in resolved charm photoproduction the gluon content in the photon contributes strongly to the cross section. Photoproduction involving heavy quarks is not discussed in this thesis, but has been measured by both HERA experiments ZEUS [20] and H1 [21].

The quark density at high x_γ

As stated above the currently available F_2^γ data have large experimental uncertainties at high x_γ values. Because of the high cross section, jet photoproduction measurements are sensitive to the quark densities up to very high x_γ. Moreover, because of the high centre-of-mass energy available, the photon can be probed at higher scales than the scales attainable at e^+e^- experiments.

2.3.3 Available parametrisations of the photon structure

The available parametrisations of the hadronic structure of the photon are discussed. In this thesis we compare next-to-leading order (NLO) QCD calculations to data (see chapter 3). For theoretical consistency, a NLO parametrisation of the photon structure has to be used in these calculations. Not many parametrisations are available for the next-to-leading order parton density functions of the photon. In this thesis the available PDF's will be used to compare data and theory.

Glück, Reya & Vogt

The GRV-HO [22, 23] next-to-leading order parametrisation of the parton densities in the photon is based on a DGLAP parton evolution, that starts from a valence-like VDM based

input distribution at a very low input scale ($Q_0^2 = 0.25$ GeV^2). The philosophy is that at such a low input scale the anomalous component of the photon structure can be generated dynamically by the evolution equations and the input distributions only require a VDM component. The VDM component is approximated by the valence quark parton density distributions of the pion [24]. There is only one adjustable parameter in these input distributions, κ, which fixes the normalisation of the VDM component. This parameter is set at $\kappa = 1.6$ after comparison to data from experiments at the e^+e^- colliders: PETRA [19], PEP [18] and TRISTAN [17]. The GRV parametrisation of the photon structure is given in the DIS$_\gamma$ factorisation scheme [22].

Gordon & Storrow

The GS96-HO [25] next-to-leading order parametrisation of the partonic structure of the photon is evolved from input distributions that contain both a VDM and an anomalous component. The input scale is taken as $Q_0^2 = 3$ GeV^2. The input distributions contain a number of adjustable parameters, that are fixed in a fit to F_2^γ data from PETRA, PEP, TRISTAN and LEP1 experiments and to e^+e^- jet data from TRISTAN experiments [26]. In the fit only data with $Q^2 \geq Q_0^2$ is used. The GS96 parametrisation of the photon structure is given in the $\overline{\text{MS}}$ factorisation scheme [27].

Aurenche, Fontannaz & Guillet

The AFG-HO [28] next-to-leading order parametrisation of the photon structure is similar to the one from Glück, Reya and Vogt. The anomalous component is assumed to vanish at the input scale, which is chosen to be $Q_0^2 = 0.5$ GeV^2. The VDM input distributions for the valence quarks, the sea quarks and the gluon are taken from the pion [29]. The normalisation is fixed from the comparison of the total photon-proton and proton-proton cross sections. The AFG parametrisation of the photon structure is given in the $\overline{\text{MS}}$ scheme.

Comparison of the parametrisations

In figure 2.5 the next-to-leading order gluon and quark densities in the photon, as given by the GRV-HO, GS96-HO and AFG-HO parametrisations of the photon structure, are shown as a function of x_γ at the scale $\mu^2 = 225$ GeV^2, which corresponds roughly to the scale in the processes measured in this thesis. The quark and gluon densities are multiplied by a factor x_γ/α_{em}. Below $x_\gamma = 0.5$, where they are most strongly constrained by experiment, the quark densities of the different parametrisations are very similar. For the quark densities at $x_\gamma > 0.5$ and for the gluon densities there are significant differences between the parametrisations, reflecting the lack of experimental constraints in these areas.

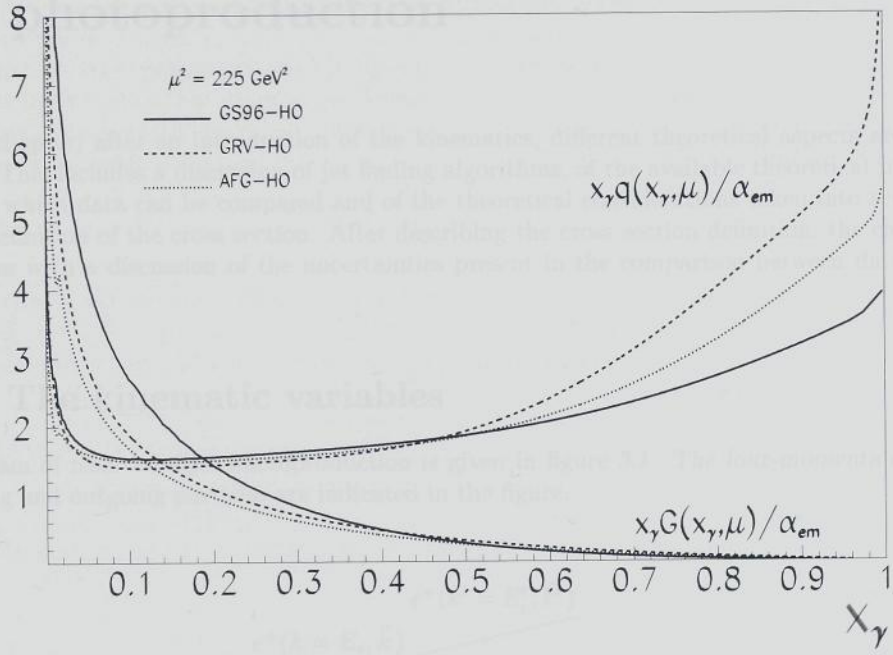

Figure 2.5: Quark and gluon density distributions in the photon at a factorisation scale $\mu^2 = 225$ GeV^2, as given by different parametrisations of the next-to-leading order hadronic structure of the photon. All parton densities are given in the $\overline{\text{MS}}$ factorisation scheme.

Chapter 3

Jet photoproduction

In this chapter, after an introduction of the kinematics, different theoretical aspects are discussed. This includes a discussion of jet finding algorithms, of the available theoretical predictions to which data can be compared and of the theoretical considerations taken into account in the definition of the cross section. After describing the cross section definition, the chapter concludes with a discussion of the uncertainties present in the comparison between data and theory.

3.1 The kinematic variables

A diagram of resolved dijet photoproduction is given in figure 3.1. The four-momenta of the incoming and outgoing particles are indicated in the figure.

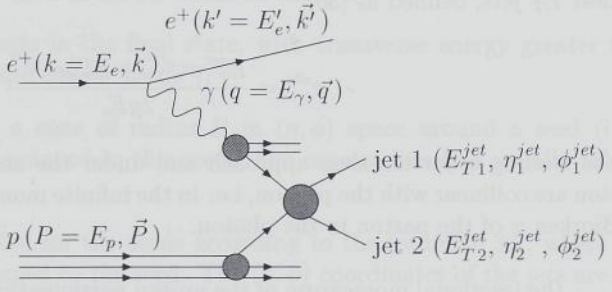

Figure 3.1: Generic diagram of a resolved dijet photoproduction event.

The kinematic variables, relevant to the present analysis, are[1]:

[1] As the processes we are dealing with involve high momenta, the masses of incoming particles and of particles in the final state are neglected throughout this thesis.

- E_T^{jet}, η^{jet} and ϕ^{jet}: the transverse energy, the pseudorapidity[2] and the azimuthal angle of the jets.

- Q^2: the virtuality of the exchanged photon, which is defined as:

$$Q^2 = -q^2 = -(k - k')^2 , \tag{3.1}$$

- y: the fractional energy transfer from the positron to the proton in the proton's rest frame, also referred to as the inelasticity. y is defined as:

$$y = \frac{q \cdot P}{k \cdot P} . \tag{3.2}$$

This formula can be rewritten as:

$$y = 1 - \frac{E'_e}{2E_e}(1 - \cos\theta'_e) , \tag{3.3}$$

where θ' is the scattering angle of the positron, defined with respect to the positive z axis. In the photoproduction limit ($\theta'_e \to 180°$) formula 3.3 reduces to $y = \frac{E_e - E'_e}{E_e} = \frac{E_\gamma}{E_e}$, where E_γ is the energy of the exchanged photon. y is related to $W_{\gamma p}$, the centre-of-mass energy of the γp-system, via:

$$W_{\gamma p} = \sqrt{ys} , \tag{3.4}$$

where s is the squared centre-of-mass energy in the positron-proton system.

- x_γ^{obs}: the fractional momentum of the photon participating in the production of the two highest E_T jets, defined as [30]:

$$x_\gamma^{obs} = \frac{E_{T1}^{jet} e^{-\eta_1^{jet}} + E_{T2}^{jet} e^{-\eta_2^{jet}}}{2yE_e} . \tag{3.5}$$

In the leading order massless approach and under the assumption that partons in the photon are collinear with the photon, i.e. in the infinite momentum limit, x_γ^{obs} is equivalent to Bjorken x of the parton in the photon.

- x_{proton}^{obs}: the fractional momentum of the proton participating in the production of the two highest E_T jets, defined as:

$$x_{proton}^{obs} = \frac{E_{T1}^{jet} e^{\eta_1^{jet}} + E_{T2}^{jet} e^{\eta_2^{jet}}}{2E_p} . \tag{3.6}$$

[2]The pseudorapidity is defined as: $\eta = -\ln\left(\tan\frac{\theta}{2}\right)$, where θ is the polar angle with respect to the proton beam direction, hereafter referred to as forward.

3.2 The reconstruction of jets

To determine the dynamics of the subprocess in a hadronic interaction, particles in the final state are grouped into jets. The properties of these jets are expected to correspond closely to the kinematics of the partons produced in the hard subprocess. This correspondence, referred to as "Local Parton Hadron Duality" (LPHD), can only be satisfied when the applied algorithm to define jets is infrared safe, i.e. when the outcome of the algorithm is insensitive to the emission of soft or collinear partons.

Two classes of algorithms are available to define jets: cone algorithms and clustering algorithms. A description of two algorithms belonging to these classes is given below. Jet finding algorithms are in general applied to a set of objects that represents the final state. These objects can be: the cells or clusters of cells in the calorimeter in which energy was deposited or the hadrons in the final state as predicted by a Monte Carlo event generator. For both algorithms, jet properties are calculated following the Snowmass convention [31], according to which the transverse energy and the angles of a jet are calculated with the formulae:

$$\begin{aligned} E_T^{jet} &= \sum_i E_T^i \,, \\ \eta^{jet} &= \sum_i \eta^i E_T^i / \sum_i E_T^i \,, \\ \phi^{jet} &= \sum_i \phi^i E_T^i / \sum_i E_T^i \,, \end{aligned} \tag{3.7}$$

where the sum runs over all objects i assigned to a jet.

3.2.1 Cone algorithm

The cone algorithm commonly used in ZEUS works as follows:

1 First a subset of all objects in the final state, with transverse energy greater than 300 MeV, is selected. These are called "seeds".

2 Then all objects within a cone of radius R in (η, ϕ) space around a seed (i.e. with $\sqrt{\Delta\eta^2 + \Delta\phi^2} < R$), are assigned to this seed. The cone radius R is usually taken to be 0.7 or 1.

3 Jet variables are calculated for the seeds according to the formulae 3.7, where the sum runs over all objects assigned to the seed. The (η, ϕ) coordinates of the jets are taken as a new set of seeds.

4 Steps 2 and 3 are repeated until convergence is reached: this is considered to be the case when after a new iteration all objects are still assigned to the same jets.

5 Finally, overlapping jets are merged when the shared fraction of the transverse energy is greater than 75%. When the shared transverse energy is less, the objects in the overlap region are assigned to the nearest jet.

3.2.2 k_T clustering algorithm

The clustering algorithm used in ZEUS is the longitudinal invariant k_T-clustering algorithm [32], which we run in the inclusive mode [33] according to the following recipe:

1 For every pair of objects in the final state (i, j) a distance parameter is defined:

$$d_{ij} = min(E_i^2, E_j^2) R_{ij}^2 , \tag{3.8}$$

where $R_{ij}^2 = \Delta\eta_{ij}^2 + \Delta\phi_{ij}^2$.

2 For every single object, i, the distance to the beam is defined as:

$$d_i = E_{Ti}^2 R^2, \tag{3.9}$$

where R is chosen to be 1.

3 If of all values d_{ij} and d_i, d_{kl} is the smallest, the objects k and l are merged according to the formulae 3.7, if however d_k is the smallest of all values, then object k is removed from the sample and added to the list of jets.

4 Steps 1 to 3 are repeated until for every object i, $d_i < min(d_{ij})$.

The objects remaining when the procedure is finished are the jets.

3.2.3 Theoretical considerations on jet algorithms

For comparisons between data and theory, jet algorithms have to be applied to different sets of four-momenta representing the hadronic final state. These can be the four-momenta of the energy deposits in the detector, of the real final state hadrons or of the outgoing partons from the hard subprocess. A suitable jet algorithm should not be sensitive to the type of objects to which it is applied.

The first and second set of objects mentioned, consist of many four-momenta that have to be combined into jets, whereas the third set, in general, consists of the four-momenta of only 2 or 3 outgoing partons. This situation is known to cause problems for cone algorithms. It is clear that the number of objects in the final state plays an important role in the selection of seeds and in the merging of jets. An example of a problematic configuration is the situation where two jets in the final state are separated by just less than $2R$ in (η, ϕ) space (see figure 3.2). In a final state with many objects these two jets will be recognised as separate jets. In a final state of only a few partons the situation is unclear. Although it is clearly natural to consider the two partons as separate jets, both partons fit into a single cone of radius R and should therefore be combined. Solutions have been devised to cure these problems [34, 35]. The most widely applied solution implies the introduction of the parameter R_{sep}, when the jet algorithm is run on a small number of particles. R_{sep} is the maximum separation between two partons that can still be combined into one jet. The value of this parameter, however, has to be tuned to data.

The k_T clustering algorithm is considered to be theoretically more sound. It does not involve the choice of seed cells and the merging of jets is unambiguous. This makes the latter

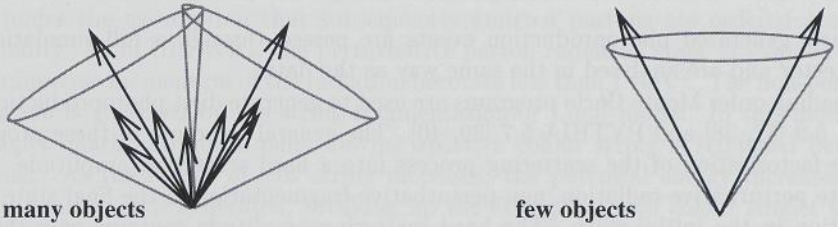

Figure 3.2: Example of configurations of four-momenta, for which the assignment of jets can be ambiguous for cone algorithms. On the left, a configuration is shown which contains many four-momenta, while on the right a very similar configuration is shown consisting of only two four-momenta.

algorithm preferable when data are compared to theoretical predictions, like for example NLO QCD calculations. For this reason the jet cross sections measured in this thesis have been determined using the k_T clustering algorithm.

3.3 Theoretical predictions

The aim of the measurement presented in this thesis is to make a quantitative comparison between a measurement of jet photoproduction and the corresponding QCD predictions. Such a comparison represents a quantitative test of perturbative QCD and may also provide new information on the hadronic structure of the photon.

At present experimental results on jet photoproduction can be compared to two classes of theoretical predictions:

- fixed order perturbative QCD calculations which are currently available up to and including the next-to-leading order $\mathcal{O}(\alpha\alpha_s^2)$.

- Monte Carlo event generators, which contain leading order matrix elements, a resummation of soft gluon radiation and some phenomenological treatment of the fragmentation of partons into hadrons.

For jet photoproduction cross sections it has been shown that NLO corrections are sizeable, see e.g. [36]. Therefore NLO QCD calculations represent the most suitable theoretical predictions to make quantitative comparisons to. Leading order Monte Carlo programs, although unable to reproduce the absolute normalisation of the cross section, describe very well the shape of differential cross sections and other distributions, like the η^{jet} distributions, the x_γ^{obs} distribution or the energy flow in events. This is no surprise, since leading and next-to-leading order calculations for dijet photoproduction have been found to differ in the normalisation but very little in the shape [36]. For this reason, Monte Carlo programs, containing only leading order matrix elements, are suitable for the unfolding of detector effects from the measured cross sections and for the study of systematic uncertainties.

3.3.1 Monte Carlo models

Monte Carlo generated photoproduction events are passed through a full simulation of the ZEUS detector and are analysed in the same way as the data.

Two leading order Monte Carlo programs are used to generate dijet photoproduction events, HERWIG 5.9 [37, 38] and PYTHIA 5.7 [39, 40]. The general structure of these programs assumes the factorisation of the scattering process into a hard scattering amplitude, final and initial state perturbative radiation, non-perturbative fragmentation in the final state and parton evolution in the initial state. The hard scattering amplitude contains only the leading order matrix elements. Differences between the two Monte Carlos lie in the treatment of the perturbative radiation and the non-perturbative fragmentation. The most important features of the two Monte Carlo models are discussed below.

For both generators event samples corresponding to direct and resolved photoproduction are generated separately. The parton density functions for the proton and the photon are the CTEQ3-LO [41] and the GRV-LO [22, 23] parametrisations, respectively.

HERWIG 5.9

The HERWIG 5.9 Monte Carlo uses the equivalent photon approximation [11] (EPA) to generate the spectrum of photons radiated from the incoming positron.

Parton radiations from the incoming and outgoing partons of the hard subprocess are resummed under the assumption of angular ordering of the subsequently emitted partons. The parton emissions are continued until the squared transverse momentum of the radiated partons becomes too low and perturbative QCD is no longer applicable. This limit is chosen around 1 GeV^2.

The non-perturbative fragmentation in the final state is governed by the phenomenological cluster fragmentation model. First, all gluons produced in the perturbative parton shower are split into quark anti-quark or diquark anti-diquark pairs. Then, quarks are combined with their nearest neighbouring anti-quark or diquark, to form colour singlet clusters. When these clusters are light, they are taken to be hadrons. Heavier clusters are allowed to decay into lighter hadrons.

In general the philosophy of HERWIG is to describe the perturbative stage in as much detail as possible. Local Parton Hadron Duality should then ensure that observables sensitive to the hard parton dynamics, i.e. infrared safe observables, are not affected by the final non-perturbative stage. This should allow the fragmentation to be governed by a relatively simple model. As a consequence of this approach the HERWIG Monte Carlo contains very few tunable parameters and has therefore high predictive power.

PYTHIA 5.7

The PYTHIA 5.7 Monte Carlo uses the Weizsäcker Williams Approximation [11] (WWA) to generate the spectrum of photons radiated from the incoming positron. As the Weizsäcker Williams Approximation provides only the y dependence of the photon spectrum, and not the Q^2 dependence, the latter has to be implemented ad hoc. We will discuss this issue in more detail in section 6.3.2.

Parton emissions from the incoming and outgoing partons of the hard subprocess are resummed under the assumption that subsequently emitted partons are ordered according to their virtuality. As in HERWIG, the perturbative parton radiation stage is stopped when the squared transverse momentum of the radiation becomes less than 1 GeV^2. The non-perturbative fragmentation is governed by the string fragmentation or Lund model. In this model, for all colour singlet quark anti-quark pairs moving apart, a colour string is stretched between the two partons. As the length of this string increases, the potential energy increases. A new quark anti-quark pair is generated, breaking up the string into two colour singlet strings. If the invariant mass of these strings is high enough they can again be split up. This procedure continues until a set of on-shell hadrons is formed.

Other Monte Carlo models

Neutral and charged current deep inelastic scattering Monte Carlo samples are used to study background contaminations of the dijet photoproduction sample. Both samples are generated using the DJANGO program. This program connects the event generator LEPTO, which can be used for both NC-DIS and CC-DIS processes, to HERACLES, which simulates electroweak radiative corrections, and ARIADNE, for the simulation of the fragmentation. For the NC-DIS sample the GRV parametrisation of the parton densities in the proton was used and for the CC-DIS sample the CTEQ4M [42] parametrisation was used.

Reweighting the Monte Carlo samples

As mentioned earlier, the photoproduction Monte Carlo models contain only the leading order contributions to the hard scattering. As a result of this, they underestimate the absolute jet cross sections. To obtain a good description of the data, the resolved and direct contributions in the Monte Carlo models are scaled. The required scale factors are determined from a fit to the measured x_γ^{obs} spectrum (see section 6.3.1). The outcome of this fit is that for HERWIG (PYTHIA) the direct component is scaled by a factor 1.92 (1.26) and the resolved component by 1.78 (1.31). For the remainder of this thesis all HERWIG and PYTHIA predictions shown include these scale factors.

3.3.2 Jet photoproduction in next-to-leading order

Currently, NLO QCD calculations incorporate our best knowledge of jet photoproduction. These calculations are available from several theoretical groups: M. Klasen et al. [36, 43], B. Harris et al. [44], S. Frixione et al. [45] and P. Aurenche et al. [46]. Calculations performed by different groups have been compared in [47] and were found to agree within 5%. The programs calculate jet cross sections up to order $\mathcal{O}(\alpha\alpha_s^2)$. Jets are identified by applying a jet algorithm to the outgoing partons. The renormalisation and factorisation scales in the calculations are taken to be equal to the highest transverse jet energy in an event. The value of Λ_{QCD} is taken to match that of the parton density functions used for the proton. All calculations include 5 quark flavours, which are treated as massless quarks. In the calculations the renormalisation and factorisation scales are chosen equal to the transverse energy of the highest transverse energy jet.

The main difference between the available NLO QCD calculations lies in the treatment of infrared and collinear singularities, which appear through the radiation of very soft or collinear gluons. Two methods are used:

- the **phase-space-slicing** or **cone method** in which one or more cutoff parameters are introduced to separate the regions in phase space that contain singularities. These phase space regions are then calculated analytically in the singular limit, rather than being integrated over. The remaining phase space that contains no more singularities is integrated over numerically. When the different regions are added together all dependence on the unphysical cutoff parameters should drop out. The cutoff parameters must be chosen sufficiently small to achieve this. Different variables are used to separate the singular regions: M. Klasen et al. [48] employ an invariant mass cutoff to separate both the soft and collinear regions, B. Harris [49] et al. and P. Aurenche et al. [46] use two distinct parameters to separate the soft and collinear regions.

- the **subtraction method** in which singularities are cancelled by subtracting appropriate soft and collinear counterterms [50]. This method is applied in the calculations of S. Frixione et al..

3.4 Definition of the measurement

In this thesis we present a measurement of dijet photoproduction. This process is particularly suited to study the structure of the photon, because the reconstruction of two jets in the final state allows for the determination of the fractional momentum of the photon participating in the hard interaction, using the formula 3.5.

To make a meaningful comparison between data and NLO QCD predictions, the measurement must be defined in such a way that non-perturbative effects, which are not included in these predictions, play a small role. To assure this, first of all, a hard scale must be present in the measured process. This scale is provided by the transverse energy of jets produced in the interaction. Yet, even in a process in which a hard scale is present, non-perturbative effects can play a role. These effects are:

- the fragmentation of partons into hadrons,

- underlying events, i.e. soft or hard interactions between partons inside the colliding particles other than the partons involved in the primary hard scatter.

The definition of the cross section presented in this thesis tries to avoid the sensitivity to the effects discussed above. It builds on the improved understanding of jet photoproduction and comparisons to NLO QCD, gained in previous analyses ([30] and [51] to [55]), and on a significant theoretical effort in the recent past ([32] to [36], [43] to [50] and [56] to [59]).

The cross section is subjected to a set of conditions, designed to minimise theoretical uncertainties:

- The cross section is determined for photoproduction events with relatively high transverse energy jets. A previous jet photoproduction analysis [53] has shown that for $E_T^{jets} >$

11 GeV, the dijet cross section agrees with NLO QCD predictions, within the experimental uncertainties. At lower transverse energies the dijet cross section for $x_\gamma^{obs} < 0.75$ is above the theoretical predictions. This is ascribed to the effect of underlying events that add to the transverse energy of jets.

- An asymmetric cut is applied on the transverse energy of the two highest transverse energy jets. The application of a symmetric cut poses a stability problem for some of the available NLO QCD calculations [56].

- Symmetrisation of the cross section with respect to the pseudorapidity of the two highest transverse energy jets has been claimed to remove infrared instabilities in the NLO QCD calculations [57]. The reason is that since in leading order both jets have equal transverse energy, the identification of the highest transverse energy or leading jet is sensitive to soft radiation effects. Therefore the pseudorapidity of the jet identified as that having the highest transverse energy is an infrared unsafe variable. The transverse energy of the leading jet itself is not infrared unsafe since it will change only marginally due to soft radiation. The symmetrisation procedure entails analysing each event twice, as explained below.

- Jets are defined using the longitudinal invariant k_T-clustering algorithm [32] in the inclusive mode [33], where the parameter R is chosen equal to 1. This algorithm provides a jet reconstruction that is suitable for comparisons between data and theory (as discussed in section 3.2).

The dijet photoproduction cross section presented in this thesis refers to events in which at least two jets, as defined by the k_T-clustering algorithm, are found in the hadronic final state. These jets are required to have pseudorapidities between -1 and 2, transverse energy of the highest transverse energy jet, $E_{T\,leading}^{jet}$, greater than 14 GeV and the transverse energy of the second highest transverse energy jet, $E_{T\,second}^{jet}$, greater than 11 GeV. The cross section is given in the kinematic region defined by: $Q^2 < 1$ GeV^2 and $0.20 < y < 0.85$.

This cross section is measured as a function of three variables: $E_{T\,leading}^{jet}$, η_1^{jet} and η_2^{jet}. The cross section is symmetrised with respect to the pseudorapidities of the two jets. Every event contributes twice to the cross section, once with $\eta_1^{jet} = \eta_{leading}^{jet}$ and $\eta_2^{jet} = \eta_{second}^{jet}$ and a second time with $\eta_1^{jet} = \eta_{second}^{jet}$ and $\eta_2^{jet} = \eta_{leading}^{jet}$.

The cross section is determined for the full range of x_γ^{obs} values and for a direct photoproduction enriched region with $x_\gamma^{obs} > 0.75$. The cross section as a function of the pseudorapidity of the jets is also measured in a narrower band of y values between 0.50 and 0.85, where the sensitivity to the photon structure is expected to be higher, as will be explained in section 8.2.

In the kinematic regime of the measurement defined above, the fractional momentum x at which partons inside the proton are probed lies predominantly in the region between 10^{-2} and 10^{-1}. At these x values the parton densities in the proton are strongly constrained by measurements of the structure function F_2^p in deep inelastic lepton-proton scattering [60]. The fractional momentum x_γ at which partons in the photon are probed lies between 0.1 and 1.

As discussed in chapter 2, at high x_γ values the quark densities in the photon are not strongly constrained by F_2^γ data obtained from $\gamma\gamma^*$ scattering in e^+e^- experiments [16, 17, 18, 19]. In

kinematic regions, where NLO QCD calculations should describe the data, the comparison of the data to these calculations can put additional constraints on the parton density distributions in the photon at high x_γ values and at higher scales than attainable at e^+e^- experiments.

3.5 Uncertainties in the comparison of data to NLO QCD

Jet measurements at the Tevatron [61] $p\bar{p}$ collider, although generally in good agreement with NLO QCD, show discrepancies in the ratio between jet cross sections at different centre-of-mass energies. These may be connected to non-perturbative effects, like underlying events or fragmentation [62]. A number of these effects, which may also be of relevance to the present study, are investigated in this section. In section 6.3, where we compare distributions of a sample of dijet events to the corresponding Monte Carlo predictions, we discuss the effect of possible underlying events.

3.5.1 Fragmentation

One of the main uncertainties is the effect on the cross section due to the fragmentation of partons into hadrons. Measured cross sections are only corrected for detector effects and therefore refer to the hadrons in the final state. The NLO calculations do not contain parton-to-hadron fragmentation and thus refer to the outgoing partons of the calculated diagrams. This parton level cross section is not directly observable and it is therefore not desirable to correct the measured cross sections to that for the outgoing partons (**parton level**), since this would introduce model dependencies in the data.

Although jet cross sections are mainly sensitive to the dynamics of the hard subprocess it is inevitable that the parton-to-hadron fragmentation has some effects on the measured jet cross sections. From theory such effects are expected to become smaller when the cross section refers to jets with higher transverse energies.

We discuss two studies into hadronisation effects that have been performed for the dijet cross section, as defined in section 3.4. The studies are based on the leading order Monte Carlo models HERWIG 5.9 [37, 38] and PYTHIA 5.7 [39, 40]. It needs to be stressed that these studies give merely an estimate of how large hadronisation effects can be, since the estimate relies on a model to describe the fragmentation and also since the set of final state partons is only an approximation of the outgoing partons in a NLO calculation.

In a study using the HERWIG and PYTHIA Monte Carlo photoproduction models, the cross section for jets of hadrons was compared to that for jets of partons produced in the two-to-two hard subprocess and in the parton showers (see figure 3.3). The change in the jet cross section due to the parton-to-hadron fragmentation is found to be less than 10% in most of the kinematic regime. Only for events with one or more very backward jets ($\eta^{jet} < -0.5$) was a more sizeable change observed. For these events the cross section is reduced by up to 40% due to fragmentation effects. In a comparable study presented in reference [58] the cross section for jets of hadrons was compared to that for jets of partons produced in the two-to-two hard subprocess. The relative difference between these cross sections was found to be less than 20%, except again for events with very backward jets ($\eta^{jet} < -0.5$), where the change in the cross

section becomes as large as 50%.

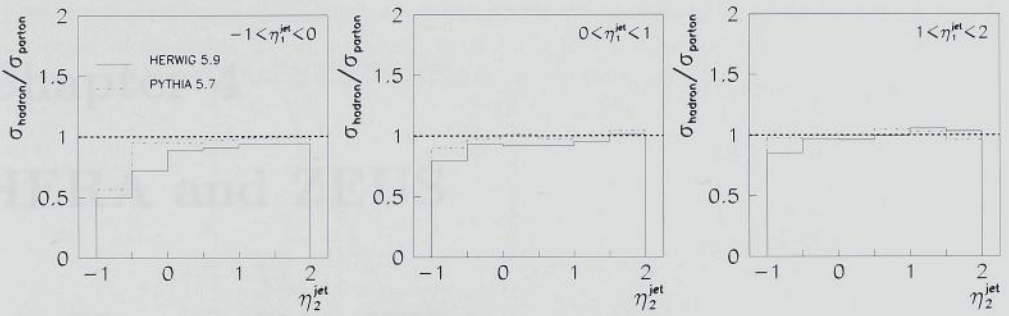

Figure 3.3: The ratio between the dijet cross section based on hadrons and that based on partons as predicted by HERWIG and PYTHIA. The ratio is shown for the dijet cross section as a function of the pseudorapidity of one of the jets while the other jet is restricted to a given pseudorapidity range.

3.5.2 Scale uncertainty

Another theoretical uncertainty is the contribution to the cross section of higher order diagrams which have not been included in the calculations. An indication of the size of these contributions can be obtained by studying the dependence of the calculated cross sections on the renormalisation and factorisation scales. This dependence, which exists for any fixed order calculation, vanishes when all orders are included. The variation of the results, when the scales are varied within a reasonable range, can be used as an estimate of the magnitude of higher order corrections. For the calculations corresponding to the presented cross sections, the scale dependence was found to be less than 15%, when the renormalisation and factorisation scales are varied between half and twice the nominal value [58].

3.5.3 The proton structure

As stated above, in the kinematic regime of the present measurement, the parton densities in the proton are strongly constrained by measurements of the structure function F_2^p in deep inelastic lepton-proton scattering [60]. The largest uncertainty in the proton structure lies in the gluon densities. In figure 3.4 a comparison is made between NLO results, determined with the NLO code from Frixione et al. [45], using the **low**, **central** and **high gluon** density parametrisations from the MRST group [63], where **low**, **central** and **high** refers to the gluon density at very high x values ($x > 0.2$). In the x region of interest to the present analysis ($0.01 < x < 0.1$) the behaviour of the gluon densities tends to be opposite, i.e. the **low gluon** parametrisation gives the highest gluon density in this region. The variation in the calculated cross sections, due to the variation in the gluon density, was found to be about 6%.

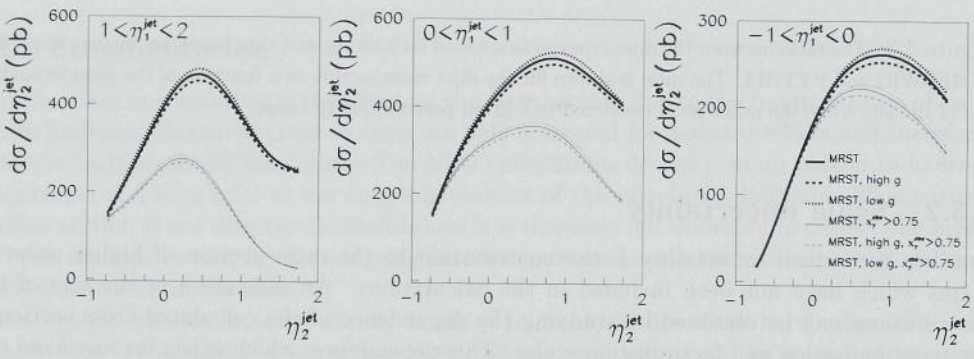

Figure 3.4: The dijet photoproduction cross section, calculated in NLO QCD using the MRST central, high and low gluon parametrisations of the proton structure. The cross section was calculated for the full x_γ^{obs} range and for a region with $x_\gamma^{obs} > 0.75$.

Chapter 4

HERA and ZEUS

4.1 The *ep* collider HERA

The HERA accelerator at the DESY laboratory in Hamburg is the first and so far only colliding beams facility in the world where electrons or positrons are collided with protons. The accelerator, situated under the "Volkspark" in Hamburg, has a circumference of 6.3 km and is located 25 m below ground level. The layout of HERA and the main parameters of the accelerator are given in figure 4.1.

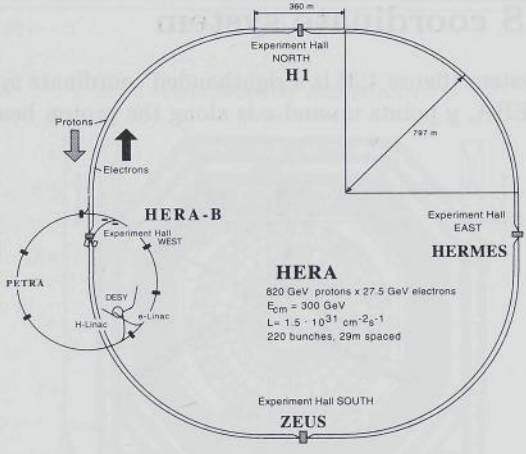

Figure 4.1: Layout of the HERA accelerator at DESY.

There are four experimental halls along the HERA ring. Since the startup of HERA in 1992 two detectors measure interactions of the colliding beams: H1 and ZEUS. Both are multipurpose detectors covering almost the full solid angle. Additional experiments are HERMES and HERA-B. At HERMES interactions between polarised beam electrons and a stationary

polarised gas target are studied. At HERA-B the proton beam collides with a stationary target to study CP violation in the decay of B-mesons.

Since the startup in 1992 the luminosity delivered by HERA has increased gradually. Figure 4.2 shows the accumulated luminosity for each year up to April 1999, as a function of time.

	Luminosity (pb^{-1})	
Year	e^-p	e^+p
1992	0.03	-
1993	1.1	-
1994	1.1	5.1
1995	-	12.3
1996	-	17.2
1997	-	36.4
1998	8.1	-
1999	12.3	-

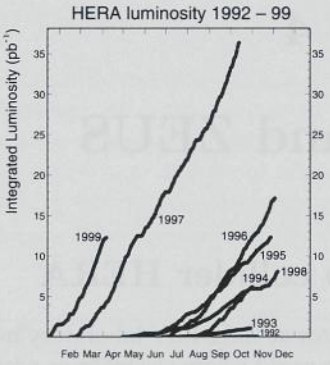

Figure 4.2: Overview of the luminosity delivered by HERA from 1992 up to April 1999.

4.2 The ZEUS coordinate system

The ZEUS coordinate system (figure 4.3) is a righthanded coordinate system in which x points towards the centre of HERA, y points up and z is along the proton beam direction.

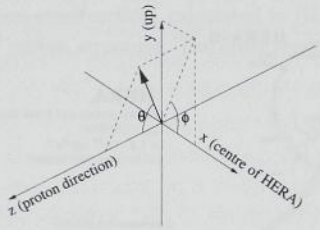

Figure 4.3: The ZEUS coordinate system.

4.3 The ZEUS detector

The ZEUS detector is a multi-purpose detector located in the south hall of HERA. The detector covers almost the full solid angle. The major components of the ZEUS detector are the inner

tracking detectors, situated in the 1.4 T magnetic field of a superconducting solenoid, the uranium-scintillator calorimeter, muon detection chambers and the luminosity monitor. In addition various dedicated detectors extend the measurement of very forward or very backward going particles. A cross sectional view of the ZEUS detector is given in figure 4.4. A detailed description of the detector can be found in [64]. In this section we discuss the components of the detector relevant to the present analysis of jet photoproduction.

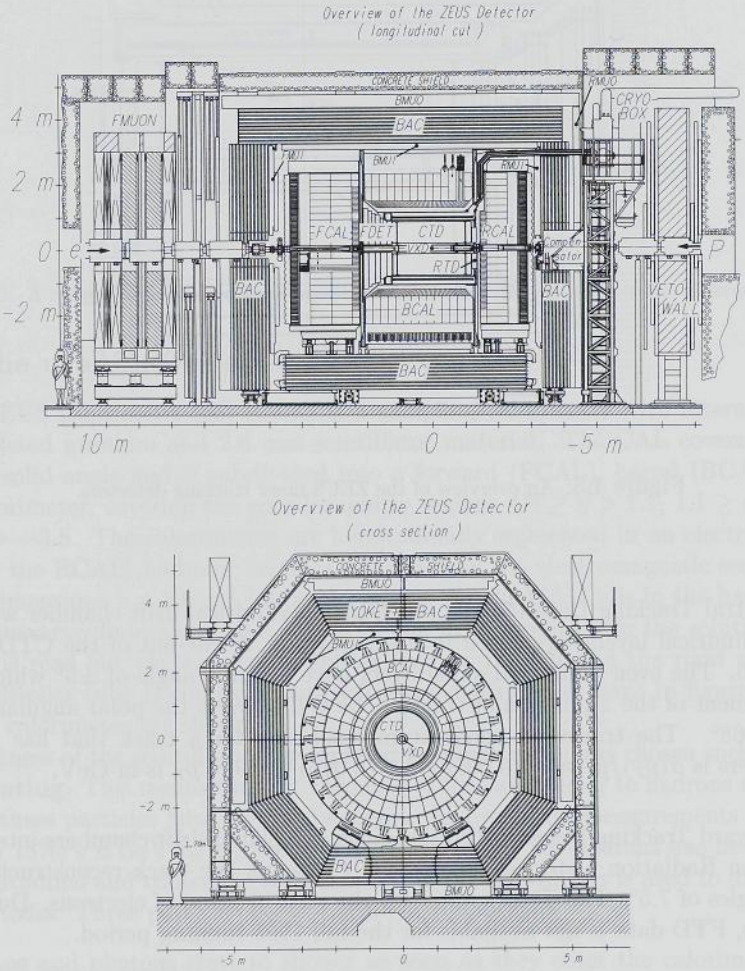

Figure 4.4: The ZEUS detector in yz and xy view.

4.3.1 The tracking detectors

The ZEUS inner tracking system consists of forward, central and rear tracking detectors, as shown in a schematic overview in figure 4.5.

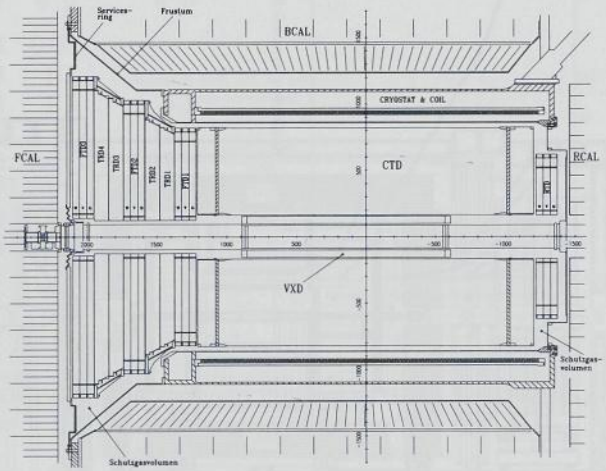

Figure 4.5: An overview of the ZEUS inner tracking detectors.

- The Central Tracking Detector [65] (CTD) is a cylindrical drift chamber which consists of 72 cylindrical layers, organised in 9 superlayers. A cut out of the CTD is shown in figure 4.6. The even numbered superlayers have a stereo angle of $\pm 5°$ which allows the measurement of the z position of tracks. The CTD covers the polar angular region from 11° to 168°. The transverse momentum resolution for a track that has traversed all superlayers is $\sigma(p_T)/p_T \approx \sqrt{(0.005 p_T)^2 + (0.016)^2}$, where p_T is in GeV.

- The Forward Tracking Detector (FTD) consists of planar drift chambers interleaved with Transition Radiation Detectors (TRD's). It extends the track reconstruction down to polar angles of 7.5°. The TRD's allow for the identification of electrons. Due to readout problems, FTD data is not available for the full 1995 running period.

- The Rear Tracking Detector (RTD) is a planar drift chamber which consists of three layers of drift cells with their wires oriented at 0°, +60° and −60° with respect to the horizontal plane. The RTD improves the accuracy of the tracking in the backward direction and covers the polar angular region between 160° and 170°.

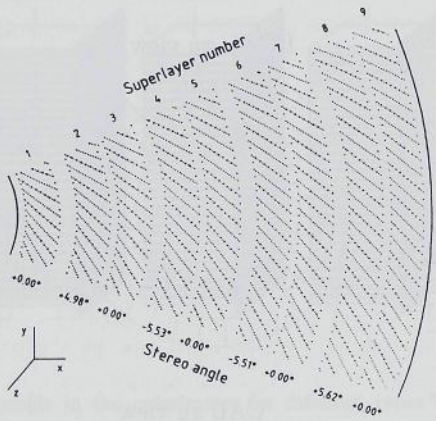

Figure 4.6: A cross sectional view of a slice of the CTD showing the wires of the different superlayers

4.3.2 The uranium calorimeter

The main ZEUS calorimeter [66] (CAL) is a sampling calorimeter with alternating layers of 3.3 mm depleted uranium and 2.6 mm scintillator material. The CAL covers almost 99.9% of the total solid angle and is subdivided into a forward (FCAL), barrel (BCAL) and a rear (RCAL) calorimeter, covering the pseudorapidity regions $4.3 \geq \eta > 1.1$, $1.1 \geq \eta > -0.75$ and $-0.75 \geq \eta > -3.8$. The calorimeters are longitudinally segmented in an electromagnetic and two (one for the RCAL) hadronic sections. The cells in the electromagnetic sections have the transverse dimensions 5×20 cm^2 (10×20 cm^2 for the RCAL). Cells in the hadronic sections have the transverse dimensions 20×20 cm^2. The light produced in the scintillator material of each cell is read out via wavelength shifter bars on the left and the right side of the cell. A photo-multiplier tube is connected to each wavelength shifter bar. In figure 4.7 schematic views of the calorimeter are shown.

The thickness of the scintillator and depleted uranium layers was chosen such that the CAL is **compensating**. This means that the response of the calorimeter to hadrons and electrons is equal when these particles have identical energies. In test beam measurements [67], an energy resolution of $18\%/\sqrt{E\,\mathrm{GeV}}$ for electrons and $35\%/\sqrt{E\,\mathrm{GeV}}$ for hadrons has been obtained.

The longitudinal and transverse segmentation of the calorimeter is used to identify different types of particles. Three particle classes can be distinguished:

- electrons and photons start to shower as soon as they enter the calorimeter. They are identified in the calorimeter by the limited shower size both longitudinally and laterally,
- hadrons start to shower later and produce deeper and wider showers,
- muons loose energy in the CAL mostly through ionisation. The deposited energy is largely

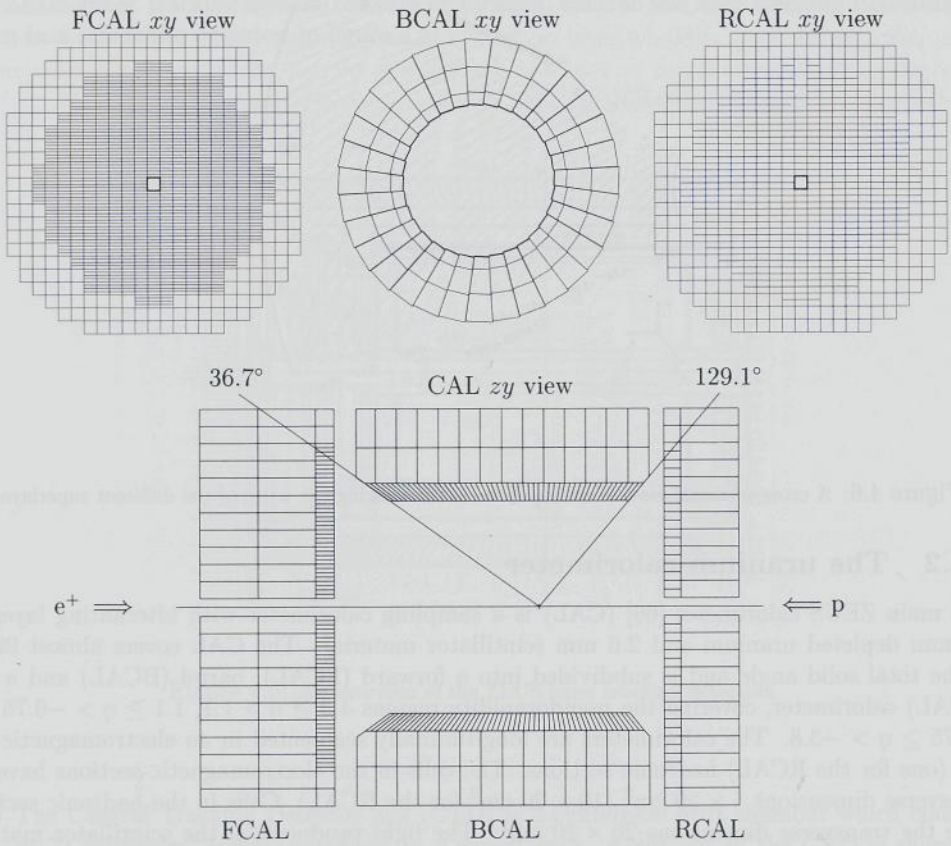

Figure 4.7: Schematic representation of the uranium calorimeter from different viewpoints.

independent of the momentum of the muon. The energy deposited in each calorimeter section is referred to as a Minimum Ionising Particle (MIP) signal.

Typical shower profiles for these particle classes are shown in figure 4.8.

The F and RCAL presampling detectors

In 1995 presampling detectors were installed on the front surfaces of the F and RCAL [68]. The two presamplers consist of 576 scintillator tiles in total, with dimensions $20 \times 20 \times 0.5$ cm^3. The tiles cover the area of the F and RCAL surface that is not shadowed by the BCAL for particles originating from the nominal interaction region. The coverage is shown in figure 4.9.

The presamplers measure the shower multiplicity of a particle entering the calorimeter. This

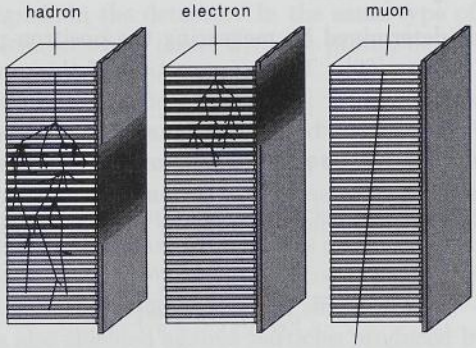

Figure 4.8: Typical shower profile in the calorimeter for different types of particles. The uranium and scintillator layers of the CAL and one of the wave length shifter bars are shown.

multiplicity is correlated to the energy loss of the particle in the inactive material in front of the CAL and can be used to correct the energy measured in the CAL for these losses. In chapter 5 the energy correction for NC-DIS scattered positrons in the RCAL, using the RCAL presampler is discussed.

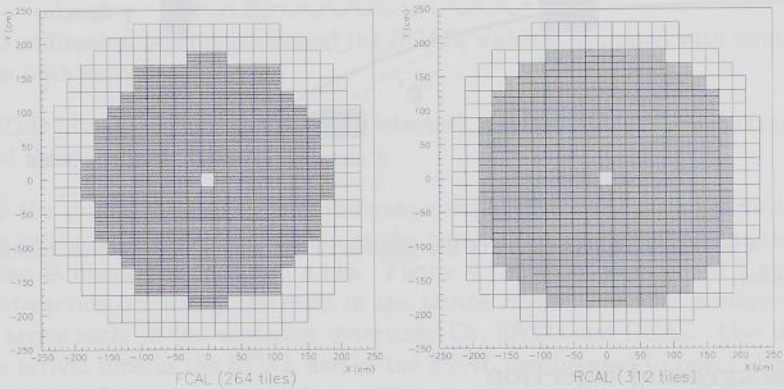

Figure 4.9: Coverage of the presamplers in front of the F and RCAL. The lines indicate the calorimeter cells and the shaded area indicates the area covered with presampler tiles.

4.3.3 The luminosity monitor

The luminosity in ZEUS is determined by measuring the positron-proton Bremsstrahlung or Bethe-Heitler process $ep \rightarrow ep\gamma$ [69]. The cross section of this process is known to a high accuracy [70]. The luminosity monitor [71] consists of a photon and an electron calorimeter positioned downstream of the positron beam (see figure 4.10). Although initially intended as a coincidence measurement, due to the poor understanding of the acceptance of the electron calorimeter, the bremsstrahlung cross section is currently determined from the count rate of photons above a certain energy threshold (E_γ^{th}) in the photon calorimeter. The luminosity is calculated as:

$$\mathfrak{L} = \frac{R_{ep}(E_\gamma > E_\gamma^{th})}{\sigma_{ep}^{acc}(E_\gamma > E_\gamma^{th})}, \tag{4.1}$$

where $R_{ep}(E_\gamma > E_\gamma^{th})$ is the photon rate and $\sigma_{ep}^{acc}(E_\gamma^{th})$ is the acceptance corrected cross section for these photons to be produced.

The photon calorimeter is a lead-scintillator sampling calorimeter with a 1 radiation length thick carbon filter in front to shield the detector from direct synchrotron radiation and a presampler to correct the measured energies for losses in dead material. The accuracy of the luminosity measurement for the 1995 running period was 1.1%.

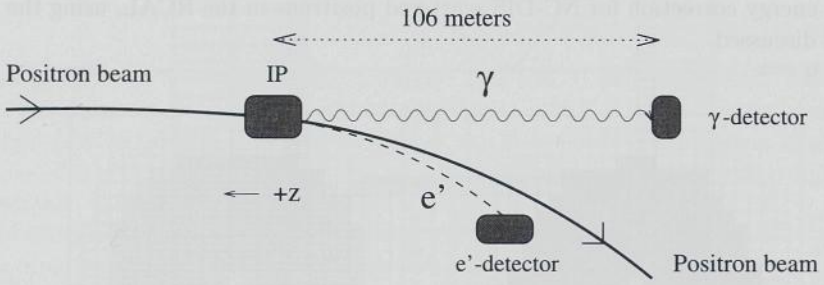

Figure 4.10: A schematic representation of the position of the photon and electron calorimeters of the luminosity monitor.

4.3.4 Background rejection

Some detectors of which the data is not used in the present analysis, nevertheless play an important role in the background rejection at the trigger level. We discuss different background sources and the detectors used to reject them.

Besides processes originating from ep interactions there are several processes observed in the ZEUS detector that originate from other sources. We shall refer to these as non-physics processes. The two main sources of such processes are:

- interactions of beam particles with residual gas in the beam pipe or with the beam pipe wall. These interactions, referred to as **beam gas** interactions, can occur in the proton

beam as well as in the positron beam. When they occur close to or inside the detector they can produce signals in the detector. In the same type of process, via the decay of pions, muons are produced which travel with the proton beam in what is called the beam halo. These are referred to as **halo muons**,

- a second source of non-physics backgrounds are cosmic interactions in the atmosphere in which muons are produced. These **cosmic muons** can deposit energy in the detector.

The strategy applied to reduce the non-physics backgrounds in the collected data is twofold. First of all the detector is shielded against the particles produced in these non-physics processes. The background from cosmic muons is strongly reduced because the ZEUS detector is located 25 m below ground level and the detector itself is shielded with $\sim$ 1 m of concrete and an iron yoke. The detector is also shielded against particles produced by the beams in the HERA tunnel. The Veto-wall, a 87 cm thick iron wall with a 95×95 cm^2 hole for the beam pipe and magnets, is positioned 7 m upstream in the proton direction and shields the detector from the proton beam halo.

The second strategy applied to reduce non-physics backgrounds is to reject them at the trigger level. For example: the Veto-wall is equipped with scintillator counters on both sides. At the trigger level, coincidences in these counters are used to reject halo muons.

The most important information used to reject non-physics backgrounds is the timing information of the following detectors:

- different calorimeter sections like e.g. the FCAL, the RCAL or the upper or lower half of the BCAL,
- the C5 collimator, positioned behind the RCAL, which is equipped with scintillator counters on both sides,
- the SRTD (Small angle Rear Tracking Detector), a scintillator strip hodoscope positioned around the rear beam hole.

In ZEUS the timing measurement of different components is calibrated in such a way that for particles produced in an ep interaction at the nominal interaction point the timing is zero. This situation is illustrated in figure 4.11a. Figure 4.11b is an example of a typical proton beam gas interaction occurring upstream in the proton beam. Particles produced in such an interaction arrive early in the upstream detectors: C5, SRTD and RCAL. Also the difference between the arrival time in the RCAL and in the FCAL can be used to reject these events. In figure 4.11c a typical cosmic muon is shown. To reject these events the difference between the arrival time in the upper and the lower half of the BCAL is used.

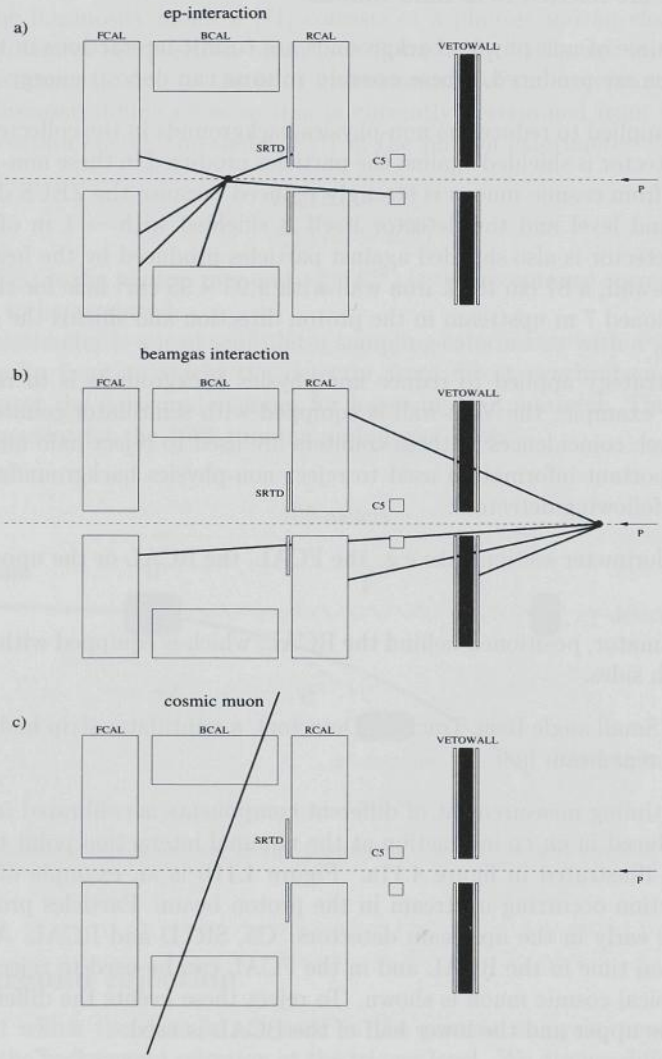

Figure 4.11: Typical signature of: an *ep* interaction at the nominal interaction point (a), an upstream proton beam gas interaction (b) and a cosmic muon (c).

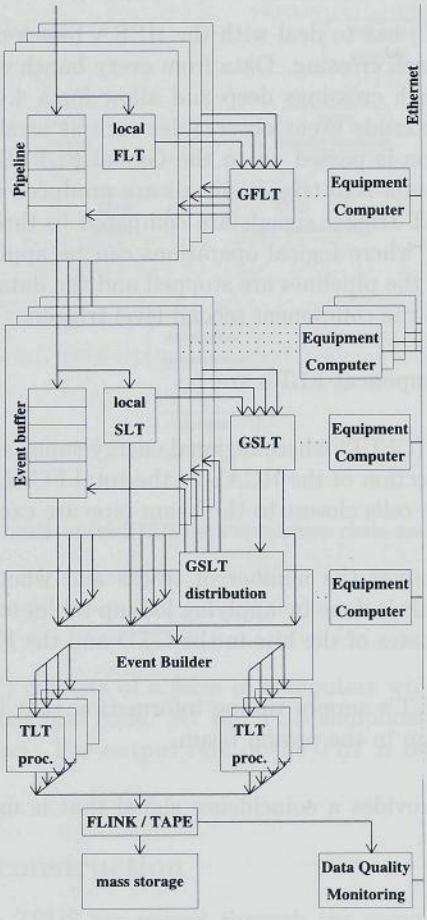

Figure 4.12: Layout of the ZEUS trigger and data acquisition chain.

4.3.5 The trigger and data acquisition chain

The ZEUS data acquisition system has to deal with the HERA bunch crossing rate of over 10 MHz. The corresponding rate of non-zero signals produced in the detector lies between 10 and 200 kHz. Of these events no more than 10 per second are accepted by the ZEUS trigger chain and stored on tape. These conditions require a multi-level trigger system, starting with fast electronics mounted on the detector, with which a crude first event selection is made and ending with an almost complete online event reconstruction. A schematic diagram of the trigger and data acquisition chain is shown in figure 4.12.

First Level Trigger

The first level trigger (FLT) has to deal with the HERA bunch crossing rate of 10 MHz, corresponding to 96 ns per bunch crossing. Data from every bunch crossing is stored in pipelines. These pipelines are 46 bunch crossings deep and allow for a 4.4 μs latency per event. The component FLT's calculate crude event observables such as local energy sums and timing information. This information is passed on to the Global FLT (GFLT) in the form of trigger signals. The rate at which non-zero trigger signals are produced in the detector is between 10 and 200 kHz. At the GFLT trigger signals are compared to thresholds. A global decision is reached in the GFLT Box, where logical operations can be applied to the trigger data. If a positive decision is reached the pipelines are stopped and the data is moved to the second level trigger event buffers and to the component second level triggers. The maximum output rate of the FLT is 1 kHz.

The most important component FLT's are:

- the Calorimeter FLT (CFLT) where regional energy sums, such as the summed energy in the electromagnetic section of the RCAL or the total FCAL energy, are determined. For most energy sums the cells closest to the beam pipe are excluded.

- the CTD-FLT determines the number of tracks and whether they originate from the interaction region. This is done by applying lookup tables to two dimensional projections of the r and z coordinates of the hits in the CTD and the FTD.

- the SRTD and C5 FLT's supply timing information that is used to reject interactions that occurred upstream in the proton beam.

- the Veto-wall FLT provides a coincidence signal that is used to reject halo muon and beam gas interactions.

Second Level Trigger

Like the FLT, the second level trigger (SLT) is divided in component SLT's and in a Global SLT (GSLT). The component SLT's provide information on global energy sums like E_T or $E - P_Z$ (CAL-SLT), on tracks, on the timing of the event and on the interaction vertex (CTD-SLT). For the determination of this information a few milliseconds are available. The information is sent to the Global SLT (GSLT) where more detailed algorithms can be applied to the data than on the GFLT. The maximum output rate of the SLT is 60 Hz.

The Event builder

The GSLT decision is passed to the event builder. When an event is accepted the event builder collects the data from all components and puts it in the standard ZEUS format. The full data is then passed to the TLT.

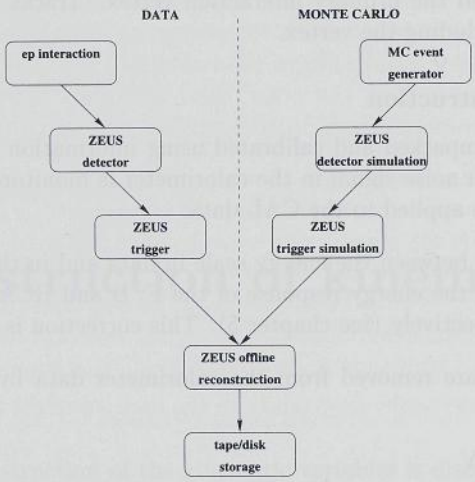

Figure 4.13: Schematic representation of the ZEUS data acquisition chain and the corresponding Monte Carlo software chain.

Third Level Trigger

The third level trigger (TLT) consists of a farm of computers which run an almost complete version of the offline reconstruction code. At the TLT complicated algorithms like electron finders and jet finders, are run. The output rate of the TLT is between 3 and 10 Hz. These events are stored to tape.

4.3.6 The offline reconstruction

Offline the data collected in ZEUS are passed through the reconstruction software package, which contains the reconstruction codes of the different detectors. In figure 4.13 a schematic overview is given of the complete data acquisition chain, on the one hand, and the corresponding software chain through which Monte Carlo simulated events are passed, on the other hand.

The offline reconstruction is largely identical for both cases. Based on the raw detector information, the reconstruction codes of the detectors determine tracks, calorimeter clusters etc. For each event a set of tables is filled containing all relevant information. This information is used in the analyses to run reconstruction jobs or to study events using event-display programs.

The tracking reconstruction

In the reconstruction code, tracks are determined based on the combined data from the CTD, the RTD and the FTD. The reconstruction code starts with pattern recognition on the hits in the detectors. The obtained tracks are fitted to a 5 parameter helix. When all tracks are

fitted the code tries to find the primary interaction vertex. Tracks that are compatible with this vertex are refitted including the vertex.

The calorimeter reconstruction

Raw calorimeter data is unpacked and calibrated using information from regularly taken test runs in which the uranium noise signal in the calorimeter is monitored. Apart from this a set of correction procedures is applied to the CAL data:

- known discrepancies between the energy scale in data and in the detector simulation are fixed by multiplying the energy response of the F, B and RCAL with the factors 1.000, 1.050 and 1.025 respectively (see chapter 5). This correction is only applied to the data;
- noise contributions are removed from the calorimeter data by removing the signals of isolated cells when:
  - $E_{emc} < 100$ MeV
  - $E_{hac} < 150$ MeV
  - $E < 700$ MeV & $|I_{cell}| > 0.70$ where I_{cell} is the fractional difference between the signal in the left and in the right photo multiplier connected to the same cell.

  Furthermore signals from cells that are known to be particularly noisy are removed when they are within three standard deviations from the average noise level observed in that cell;
- in some cases calorimeter energy deposits can be faked by "sparks" in the electronics. To reject sparks, cells with energy greater than 700 MeV and $|I_{cell}| > 0.90$ are removed.

Chapter 5

The reconstruction of kinematic variables

In this section the reconstruction of the kinematic variables is discussed. Within ZEUS, photoproduction events are defined through the requirement that the scattered positron is not detected in the uranium calorimeter. As a consequence the kinematic reconstruction relies completely on the measurement of the hadrons in the final state. The accurate measurement of energy deposits belonging to the hadronic final state is thus of great importance, especially since the differential cross section we measure has a steep dependence on the transverse energy of the jets. This means uncertainties in the hadronic energy measurement lead to large uncertainties in the measured cross section.

There are several sources of uncertainty in the measurement of the energies in the final state:

- the absolute energy response of the calorimeter. Studies on the energy response of the calorimeter to the scattered positron in NC-DIS events [72] have revealed a difference between the measured positron energy and the simulated response. This has resulted in a set of correction factors, which are: 1.000, 1.050 and 1.025 for the F, B and RCAL, respectively. These factors are applied to all energy deposits in both the EMC and the HAC sections of the CAL. The uncertainty in the absolute energy scale of the calorimeter after applying these factors is estimated to be 1 to 3% for the scattered positron, depending on where in the CAL its energy is deposited, and 5% for hadrons.

- energy losses in inactive materials in front of the CAL. Construction materials of the inner tracking system, the beam pipe and the solenoid amount to 1 to 3 radiation lengths of dead material, which a particle has to traverse before reaching the front surface of the CAL. Since many particles in the final state have low energies, the energy losses in dead material can be relatively large. These energy losses are difficult to implement accurately in the detector simulation.

- the transition regions between the F, B and RCAL. The energy response for particles entering these regions is not well simulated.

With the large statistics accumulated in 1995, it has become possible to perform detailed studies on the hadronic energy response. For the present analysis an energy correction method was developed that on the one hand reduces the sensitivity to the accurate simulation of the calorimeter energy response and on the other hand optimises the resolution of the energy measurement. A twofold strategy is used to achieve this:

- where possible tracking information is used. This strongly reduces the sensitivity to energy losses in the inactive material in front of the CAL.
- energy correction functions for particles in the hadronic final state are determined independently for data and for Monte Carlo events passed through the ZEUS detector simulation, on the basis of kinematic constraints.

It will be shown that a combination of these strategies improves the energy resolution significantly and reduces the energy scale uncertainty in the hadronic final state to $\pm 3\%$.

5.1 A combination of track and calorimeter information

We discuss the procedure used to combine track and calorimeter information. This procedure will be applied to clusters defined from the energy deposited in calorimeter cells and from tracks measured with the inner tracking detectors.

Calorimeter cells in which energy was deposited are clustered into **cone islands** [73]. These are defined in two steps:

- first, by the iterative combination of cells with their highest energy neighbours, local islands are defined in the EMC, HAC1 and HAC2 sections of the CAL,
- the thus obtained islands are then clustered in (θ, ϕ) space, starting from the HAC2 islands and working inwards towards the centre of the detector.

From the tracking detectors only tracks originating from the interaction vertex are used, since only those tracks can be unambiguously identified as particles produced in the primary interaction.

The basic strategy used to combine the tracks and cone islands is the following:

- for charged particles within the acceptance of the tracking detectors and with low or intermediate momentum we want to use the tracking detector information,
- for neutral particles, particles outside the tracking acceptance or particles with high momenta, the energy measured by the calorimeter should be used.

This ensures that in all cases the most reliable source of information is used. Naturally there are difficult cases: e.g. when neutral and charged particles overlap in the calorimeter. Especially for such cases, it is important that the combination of tracking and calorimeter information is such that double counting or the complete removal of energy are avoided. This requires a detailed matching between cone islands and tracks and a set of rules to determine when the track momentum is used and when the island energy is used.

An algorithm that combines calorimeter and tracking information has been developed within ZEUS [73]. To ensure a good momentum measurement, selected tracks are required to:

- originate from the primary vertex,
- have a transverse momentum between 0.1 GeV and 30 GeV,
- have traversed at least 3 superlayers of the CTD.

A track is considered to be matched to a cone island when the distance of closest approach between track and island is less than 20 cm or less than the radius of the island. Note that more than one track can be matched to one cone island and vice versa. The momenta of tracks that are not matched to an island or the energy of islands not matched to a track, are retained. When track and island are found to match the track momentum will be used when:

- $\sigma(P)/P < \sigma(E)/E$, i.e. the resolution of the track momentum is better than that of the island energy, where the track resolution is taken as $\sigma(P)/P = \sqrt{(0.005p_T)^2 + (0.016)^2}$ and the calorimeter resolution as $\sigma(E)/E = 25\%/\sqrt{E(\mathrm{GeV})}$ ($\sigma(E)/E = 40\%/\sqrt{E(\mathrm{GeV})}$) for electromagnetic (hadronic) islands.
- $E/P < 0.8 + \sigma(E/P)$, which avoids throwing away neutral energy that overlaps with the energy deposited by a charged particle. $\sigma(E/P)$ is defined through $\sigma(E/P)/(E/P) = \sqrt{(\sigma(E)/E)^2 + (\sigma(P)/P)^2}$.

When these requirements are not fulfilled the island energy is used. The resulting objects are called ZUFOs.

In figure 5.1 the transverse energy flow in dijet photoproduction events, measured with ZUFOs, is shown as a function of the polar angle θ. The shaded area indicates the amount of transverse energy measured with tracks. In the central region of the detector between 20 and 40% of the transverse energy is measured with tracks. In figure 5.2 the same transverse energy flow is shown as a function of the transverse energy of the ZUFOs in three angular regions corresponding to the F, B and RCAL. According to expectation, the use of track information is strongest at low transverse energies.

It is clear that a significant part of the ZUFOs still consists of calorimeter information. This is due to cases in which no track was found pointing to an island, e.g. for a neutral particle, or when a track was found that did not satisfy the quality criteria. For these "calorimeter"-ZUFOs a correction is required for energy losses in the inactive material in front of the CAL.

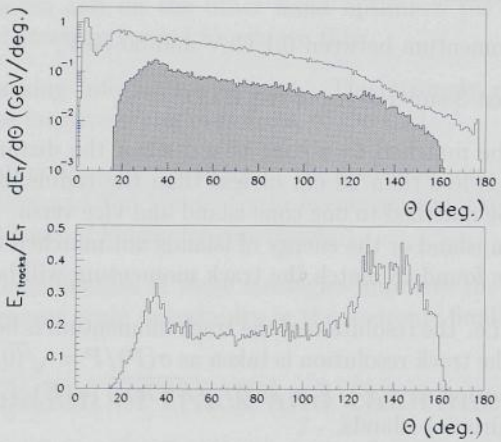

Figure 5.1: The transverse energy flow in dijet photoproduction events, measured with ZUFOs, as a function of θ. The shaded histogram indicates the amount of transverse energy measured with tracks. The lower figure shows the fraction of the transverse energy flow measured using tracks.

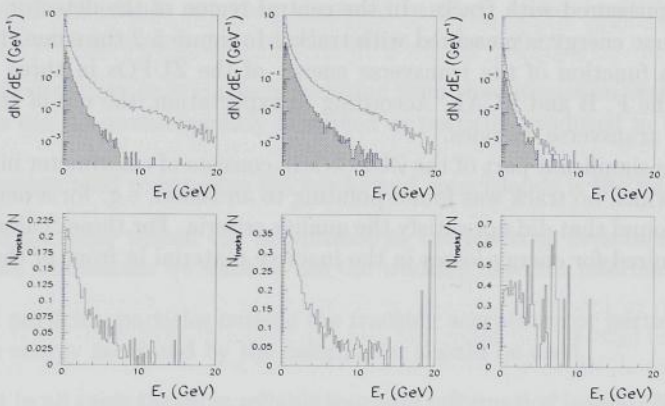

Figure 5.2: The average transverse energy distribution of ZUFOs in dijet photoproduction events, in angular bins corresponding to the F, B and RCAL. The hatched histograms indicate the amount of transverse energy measured with tracks. The lower figures show the fraction of the transverse energy flow measured with tracks.

5.2 Determination of hadronic energy corrections

The use of track information reduces the sensitivity to differences between the CAL energy scale in the data and in the detector simulation. However the large fraction of ZUFOs, for which the energy is still measured by the calorimeter, require a correction for energy losses in the materials in front of the CAL. To reduce further the sensitivity to energy scale differences between the data and the simulation, these corrections have been determined for data and Monte Carlo independently.

A method is presented that exploits energy and momentum conservation to determine energy correction functions for the particles in the final state. The method makes use of the fact that, in ZEUS, the energy measurement of the scattered positron, in particular in some restricted regions, is much better understood than the measurement of the energies in the hadronic final state. In a fit procedure to NC-DIS data and Monte Carlo samples, this situation is exploited to constrain the hadronic energies.

The fit minimises the difference between the transverse momentum, P_T, of the hadronic final state and the scattered positron. It also minimises the difference between y determined from the hadronic final state and from the scattered positron. When the procedure is applied to ZUFOs, energy correction functions are determined only for "calorimeter"-ZUFOs, assuming that track momenta are measured with sufficient accuracy already.

5.2.1 Input samples for the fit

The fit is performed on high Q^2 NC-DIS data and Monte Carlo events. The Monte Carlo sample was generated with the DJANGO event generator, interfaced to ARIADNE for the simulations of the fragmentation stage (see section 3.3.1). Two subsamples, of the data and the Monte Carlo, serve as input for the fit:

- sample 1 consists of low y events for which most of the hadronic energy flow is in the forward direction. The cuts defining sample 1 are given in table 5.1.

Sample 1
$20\ \text{GeV} < E'_e < 28\ \text{GeV}$
$130^\circ < \theta'_e < 149^\circ$

Table 5.1:

For these events the relative difference between the transverse momentum of the positron and of the final state hadrons is minimised in the fit. The transverse momentum of the positron is given by:

$$P_{T\,elec} = |E'_e \sin\theta'_e|\,, \tag{5.1}$$

and that of the hadrons by:

$$P_{T\,had} = |\sum_{hadrons} E \sin\theta|\,. \tag{5.2}$$

- sample 2 consists of high y events. Like P_T, y can be reconstructed both from the scattered positron and from the hadrons in the final state. The determination of y from the scattered positron uses the formula 3.3. For the reconstruction of y from the hadrons in the final state the Jacquet-Blondel formula [74] is used:

$$y_{JB} = \frac{\sum_{hadrons}(E - P_z)}{2E_e}. \tag{5.3}$$

Compared to P_T, y is more sensitive to hadronic energy deposited in the backward direction. Sample 2 is defined by the cuts given in table 5.2 (γ_{had} is defined below in formula 5.6).

Sample 2
15 GeV $< E'_e <$ 20 GeV
$130° < \theta'_e < 155°$
$\gamma_{had} > 57°$

Table 5.2:

For the events in sample 2 the relative difference between y determined from the scattered positron (formula 3.3) and y_{JB} (formula 5.3) is minimised.

As for hadrons, the energy of the scattered positron is affected by energy losses in the materials in front of the CAL. The positron energies are corrected for these losses using the shower multiplicity information measured with the presampler detector in front of the RCAL (see section 4.3.2). Since energy losses in dead material are not well modelled in the Monte Carlo the correction for these energy losses is determined independently for data and for Monte Carlo from the correlation between the presampler response and the energy loss. To determine the energy loss, the positron energy is estimated from the scattering angles of the positron and the struck quark, using the double angle formula [75]:

$$E_{da} = \frac{2E_e(1 - y_{da})}{1 - \cos\theta'_e}, \tag{5.4}$$

which makes use of

$$y_{da} = \frac{\sin\theta'_e(1 - \cos\gamma_{had})}{\sin\gamma_{had} + \sin\theta'_e - \sin(\theta'_e + \gamma_{had})}, \tag{5.5}$$

where γ_{had} is the hadronic scattering angle defined through:

$$\cos\gamma_{had} = \frac{P_{T\,had}^2 - (E - P_z)_{had}^2}{P_{T\,had}^2 + (E - P_z)_{had}^2}. \tag{5.6}$$

To first order the energy of the scattered positron determined with the double angle method is independent of the calorimeter energy scale.

The correlation between the energy loss, $(E_{positron} - E_{da})$, and the presampler response, $E_{presampler}$, of positrons from the samples 1 and 2 is shown in figure 5.3, where $E_{positron}$ is

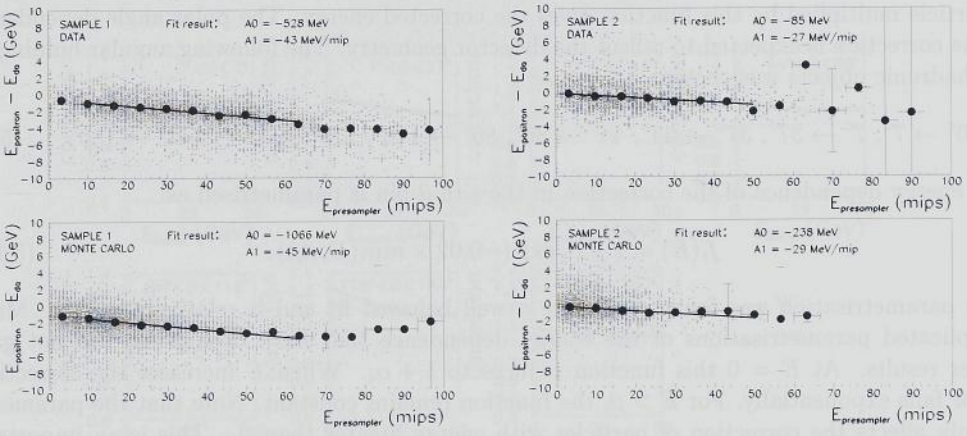

Figure 5.3: The correlation between the energy loss, $(E_{positron} - E_{da})$ and the presampler response, $E_{presampler}$, in units of minimum ionising particles, for positrons from the samples 1 and 2, for data and for Monte Carlo. The intersection point, A_0, and the slope, A_1, indicated in the figure are the result of a straight line fit to the correlation.

the energy of the scattered positron as measured with the CAL. The upper plots show the correlation in data and the lower plots the correlation in the Monte Carlo. A clear correlation is observed between the variables plotted. High signals in the presampler correspond to large energy losses. The intersection point, A_0, and the slope, A_1, indicated in the figure are the result of a straight line fit to the correlation. The corrected positron energy is now defined as:

$$E_{corr} = E_{positron}(1. - A_0 - A_1 E_{presampler}) \,. \tag{5.7}$$

A comparison of the corrected positron energy with the true positron energy in the Monte Carlo and a comparison of the distribution of the corrected positron energies in data and Monte Carlo show that for the two positron samples discussed the corrected positron energies have a bias with respect to the true energies which is less than 1.5%.

5.2.2 The minimisation procedure

The function that is minimised in the fitting procedure has the following form:

$$\sum_{sample\,1} min\left(\left(\frac{P_T^{elec} - P_T^{had}}{P_T^{elec}}\right)^2, 0.2^2\right) + \sum_{sample\,2} min\left(\left(\frac{y^{elec} - y^{had}}{y^{elec}}\right)^2, 0.2^2\right) \,. \tag{5.8}$$

Relative differences bigger than 20% are truncated at this value to prevent too strong an influence in the fit of (poorly measured) events in the tails of the distributions.

The energy correction for energy deposits in the hadronic final state is parametrised as a function of the uncorrected energy and the polar angle of the object. The measured energy of a particle multiplied by this function gives the corrected energy. The polar angle dependence of the correction is expected to reflect the detector geometry. The following angular binning of the hadronic objects was chosen:

$$0^\circ \to 7^\circ,\ 7^\circ \to 37^\circ,\ 37^\circ \to 44^\circ,\ 44^\circ \to 86^\circ,\ 86^\circ \to 118^\circ,\ 118^\circ \to 144^\circ,\ 144^\circ \to 180^\circ \qquad (5.9)$$

The energy dependence of the correction in the i-th θ bin is parametrised as:

$$f_i(E) = 1 + \alpha_i \exp\left(-0.02 \times min(E, \beta_i)\right). \qquad (5.10)$$

This parametrisation was found to ensure a well behaved fit and is relatively simple. More complicated parametrisations of the energy dependence that have been tried, did not give better results. At $E = 0$ this function reduces to $1 + \alpha_i$. When E increases the correction factor falls exponentially. For $E > \beta_i$ the function remains constant. Note that the parameter β_i only affects the correction of particles with energy greater than β_i. This is an important feature of the correction function; since most energy in the final state is carried by particles with relatively low energy, the fit tends to be dominated by the preferred behaviour at low energies.

The minimisation procedure that fixes the 14 (7×2) free parameters in the fit is performed using the package MINUIT [76]. Figure 5.4 shows the correction functions determined for "calorimeter"-ZUFOs in data and Monte Carlo.

5.2.3 Performance of the energy correction on Monte Carlo

Photoproduction Monte Carlo events, in which the true variables are known, are used to test the performance of the correction functions, determined as described above. The HERWIG 5.9 Monte Carlo generator is used for this study. The measured transverse energy of jets is compared to the transverse energy of jets determined from the final state hadrons. We consider the latter as the true transverse energy of a jet. The comparison is made for transverse jet energies determined from uncorrected islands and from uncorrected and corrected ZUFOs. The relative difference between the true and the measured transverse energies is shown in figure 5.5 as a function of η^{jet} and in figure 5.6 as a function of E_T^{jet} in different η^{jet} bins. The shaded bands indicate the resolution in E_T^{jet}. The true transverse jet energy is required to be greater than $11\,GeV$. We find that for jets determined from ZUFOs both the bias and the resolution of the E_T^{jet} measurement are improved. After the ZUFOs have been corrected for energy losses in dead material, as described above, the measured transverse jet energies come even closer to the true values and the resolution is further improved. After correction of the ZUFOs, the transverse energy of jets with pseudorapidity greater than -1, agrees to within 2% with the transverse jet energy at the hadron level. There is also a noticeable improvement in the transverse energy measurement in the transition regions between F and BCAL ($\eta \approx 1$) and between B and RCAL ($\eta \approx -1$).

A similar comparison is made for y_{JB}. In figure 5.7 the relative difference between y_{JB} and y_{true} is plotted as a function of x_γ^{obs}, the fractional momentum of the photon participating in

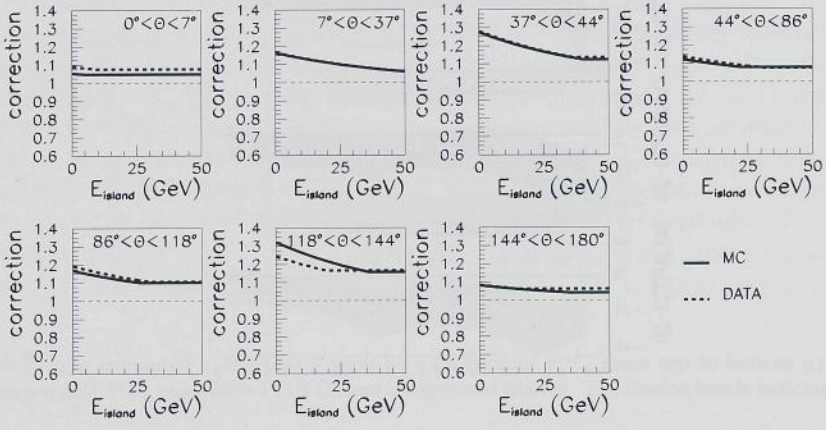

Figure 5.4: Energy correction functions obtained from a minimisation of equation 5.8 for data and Monte Carlo in different θ regions.

the hard interaction. It is particularly interesting to study the reconstruction of y as a function of x_γ^{obs}, because x_γ^{obs} is a measure of the relative contribution to $E - P_z$ coming from the jets, i.e. for an event with $x_\gamma^{obs} \approx 1$ all $E - P_z$ is contained in the jets while for a low x_γ^{obs} event most $E - P_z$ is found outside the jets. y_{JB} has been determined from uncorrected islands and from corrected and uncorrected ZUFOs. With ZUFOs both the bias and the resolution of the y_{JB} measurement are improved. After the correction of the ZUFOs for energy losses, the bias and the resolution in the y_{JB} reconstruction are further improved. The y_{JB} value from corrected ZUFOs still deviates somewhat from the true y value at low x_γ^{obs}. Such a deviation is expected, because at low x_γ^{obs} (i.e. for resolved photoproduction events) some final state hadrons are expected to escape detection because they leave the detector through the backward beam pipe hole.

5.3 Hadronic energy scale uncertainty

It has been established in the previous section that our energy correction method for the hadronic final state performs well on Monte Carlo events. In this section we want to show that the method performs equally well on data. For this purpose a study is presented in which energy dependent variables in data and Monte Carlo are compared to the expected values of these variables determined from the scattering angles in the event. The hadronic final state is reconstructed using uncorrected islands or corrected ZUFOs. The aim of the study is to:

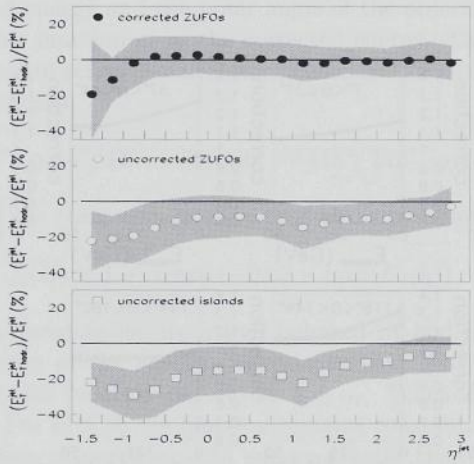

Figure 5.5: The transverse energy of jets compared to the true transverse jet energy, plotted against the pseudorapidity of the jet. From top to bottom the transverse jet energy is calculated using: corrected ZUFOs, uncorrected ZUFOs and uncorrected islands. The shaded bands indicate the resolution in E_T^{jet}.

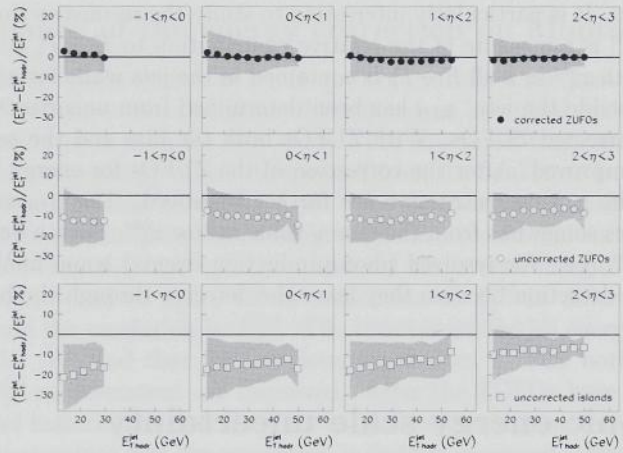

Figure 5.6: The transverse energy of jets compared to the true transverse jet energy, plotted against the true transverse jet energy in different bins of the pseudorapidity. From top to bottom the transverse jet energy is calculated using: corrected ZUFOs, uncorrected ZUFOs and uncorrected islands. The shaded bands indicate the resolution in E_T^{jet}.

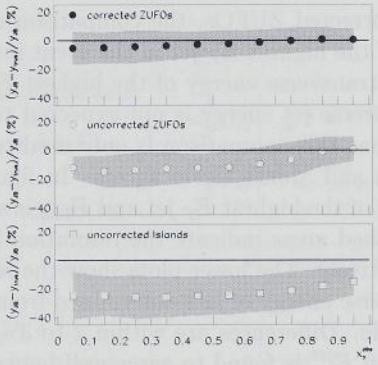

Figure 5.7: y_{JB} compared to the true y value as a function of x_γ^{obs}. From top to bottom y_{JB} is calculated using: corrected ZUFOs, uncorrected ZUFOs and uncorrected islands. The shaded bands indicate the resolution in y_{JB}.

- demonstrate that a scale difference exists between the calorimeter response in the data and in the detector simulation,
- show that this discrepancy is reduced when ZUFOs, subjected to the energy correction method described above, are used.

5.3.1 Comparison of hadronic and double angle variables

A comparison is made between P_T and y determined from the hadronic final state and from the scattering angles in an event. The variables are calculated as described in section 5.2. The hadronic P_T and $E - P_z$ are determined on the basis of uncorrected islands and corrected ZUFOs. The island(s) and track(s) belonging to the scattered positron are excluded. The transverse momentum can be reconstructed with the double angle method using the formula:

$$P_{T\,da} = 2E_e(1 - y_{da})\frac{\sin\theta'_e}{(1 - \cos\theta'_e)}\,. \tag{5.11}$$

To first order variables determined with the double angle method are independent of the calorimeter energy scale. This makes the double angle variables very suitable as reference values when the energy response in data and Monte Carlo is compared. In most of the NC-DIS phase space the variables measured with the double angle method are reconstructed with good resolution and deviate little from the true variables.

In the figure 5.8 and 5.9 the relative difference between the hadronic and the double angle measurement of P_T and y is plotted as a function of γ_{had}, for data and Monte Carlo. Also plotted is the relative difference between data and Monte Carlo. For uncorrected calorimeter information in the BCAL region the energy response in data is 2 to 3% lower than in the Monte Carlo. For corrected ZUFOs data and Monte Carlo agree within 2%.

To test the agreement between data and Monte Carlo for the reconstruction of transverse jet energies measured with corrected ZUFOs, the comparison of $P_{T\,had}$ and $P_{T\,da}$ is repeated using the transverse energy of the highest E_T jet in the event instead of the total hadronic P_T. Although closely related, the transverse energy of the highest E_T jet is not the same quantity as $P_{T\,had}$. Therefore the transverse jet energy is not expected to be balanced precisely by the double angle P_T. We stress that this comparison is only used to check that the transverse jet energy reconstruction in data and Monte Carlo agrees. In figure 5.10 the relative difference between the transverse energy of the highest E_T jet and $P_{T\,da}$ is shown as a function of E_T^{jet} and η^{jet}. The shaded and the dashed areas indicate the resolution in the transverse jet energy in data and Monte Carlo, respectively. The lower plots show the relative difference between data and Monte Carlo. The transverse energy of jets determined from corrected ZUFOs, agrees well between data and Monte Carlo. Differences are within 2 to 3% in the plotted regions of E_T^{jet} and η^{jet}. Also the resolution in E_T^{jet} is found to agree well between data and Monte Carlo.

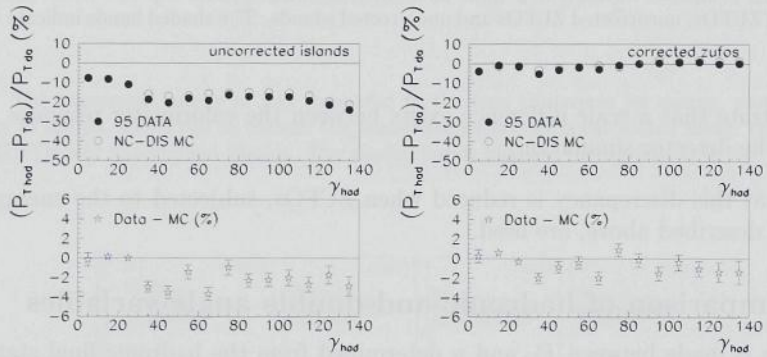

Figure 5.8: The relative difference between P_T reconstructed from the hadronic final state and with the double angle method. In the left figures the hadronic final state is defined from uncorrected islands and in the figures on the right from corrected ZUFOs. The difference is plotted as a function of γ_{had}. The lower plots show the relative difference between data and Monte Carlo. The errors are statistical errors only.

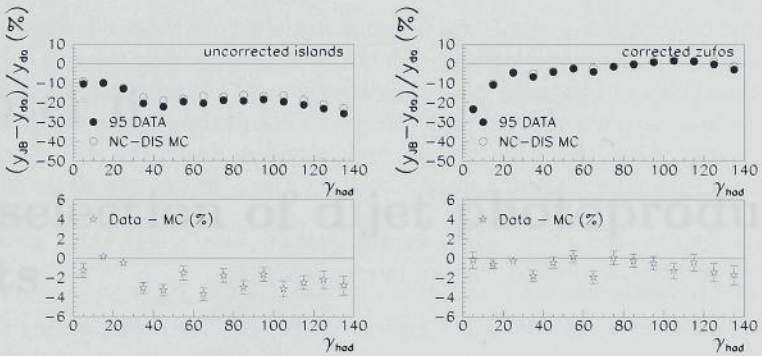

Figure 5.9: The relative difference between y reconstructed from the hadronic final state and with the double angle method. In the left figures the hadronic final state is defined from uncorrected islands and in the figures on the right from corrected ZUFOs. The difference is plotted as a function of γ_{had}. The lower plots show the relative difference between data and Monte Carlo. The errors are statistical errors only.

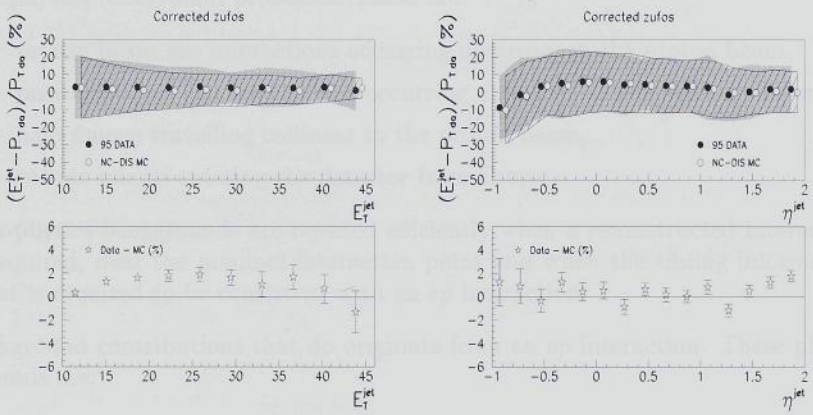

Figure 5.10: The relative difference between E_T^{jet} and $P_{T\,da}$ as a function of E_T^{jet} (left) and η^{jet} (right) for data and Monte Carlo. E_T^{jet} is determined from corrected ZUFOs. The shaded and the dashed areas indicate the resolution in data and Monte Carlo, respectively. The lower plots show the difference between data and Monte Carlo. The errors in the lower plots are statistical only.

Chapter 6

The selection of dijet photoproduction events

For the analysis presented in this thesis data collected with the ZEUS detector in 1995 are used. These data correspond to an integrated luminosity of 6.3 pb^{-1}. In this section the online and offline selection of the dijet photoproduction sample is discussed. Candidate events are selected online with the ZEUS three-level trigger system. After the selected events have been corrected for detector effects, as described in chapter 5, the final selection cuts are applied.

The selection criteria are designed to select dijet events and to reject at the same time as many background events as possible. Different processes are a potential source of background. We distinguish two classes:

- non-physics background processes. These are:
  - proton beam gas interactions occurring upstream in the proton beam,
  - positron beam gas interactions occurring upstream in the positron beam,
  - halo muons travelling collinear to the proton beam,
  - cosmic muons entering the detector from above.

  Non-physics backgrounds are rejected efficiently when a reconstructed interaction vertex is required, near the nominal interaction point and when the timing information of the event is required to be consistent with an ep interaction,

- background contributions that do originate from an ep interaction. These physics backgrounds are:
  - neutral current deep inelastic scattering (NC-DIS) events. Most of these events are rejected by a cut on the difference between the total energy and longitudinal momentum of the event ($E - P_z$), which is twice the positron beam energy in a NC-DIS event and only twice the energy of the exchanged photon in a photoproduction event, because in the latter type of event the scattered positron escapes undetected. Most of the remaining NC-DIS events can be rejected when a scattered positron candidate is identified in the calorimeter;

– charged current deep inelastic scattering (CC-DIS) dijet events. These are rejected by a cut on the missing transverse momentum in the event.

Event displays of background events are shown in figure 6.1. In the display the histogram on the left shows the transverse energy deposited in the CAL as a function of η and ϕ, while on the right cross sectional views of the inner tracking detectors and the CAL are shown. Each event satisfies the dijet selection cuts of the analysis presented in this thesis, with the exception of the cuts specifically designed to reject the type of background to which the shown event belongs. The background rejection cuts are discussed hereafter. The events shown in the figures are:

- a proton beam gas interaction. These events typically have a high track multiplicity and many tracks are not associated with an interaction vertex,
- a cosmic muon. The event shown is a typical example of a muon traversing the detector. There is only one track and there are energy deposits on opposite sides of the BCAL,
- a NC-DIS event. The event shown is a genuine dijet event, but not a photoproduction event. This is clear from the scattered positron, observed in the RCAL,
- a CC-DIS event, which is recognised by the large missing transverse momentum in the event, which has been carried away by the neutrino.

6.1 Online event selection

The ZEUS three-level trigger system is used to preselect a sample of dijet photoproduction candidates. Selection criteria are applied at each of the three trigger levels.

6.1.1 First Level Trigger

At the FLT the summed energies of different sections of the calorimeter[1] are compared to threshold values. Furthermore crude track information is available. The requirements made at the FLT to select dijet candidate events are the following:

- $E^{CAL} > 15$ GeV or $E^{CAL}_{EMC} > 10$ GeV or $E^{BCAL}_{EMC} > 3.4$ GeV or $E^{RCAL}_{EMC} > 2$ GeV,
- at least one good track was found, where a good track is defined as a track for which the z position in the first superlayer of the CTD is between -50 cm and 80 cm.

Furthermore events are vetoed at the FLT based on information from various detectors:

- the C5 timing information is used to veto events that have a beam gas timing and no physics timing in one or both C5 scintillator counters,

[1]For the determination of calorimeter energy sums at the FLT the cells closest to the beam pipe are excluded. Furthermore the energy is subjected to a coarse digitisation which makes the energy resolution rather poor.

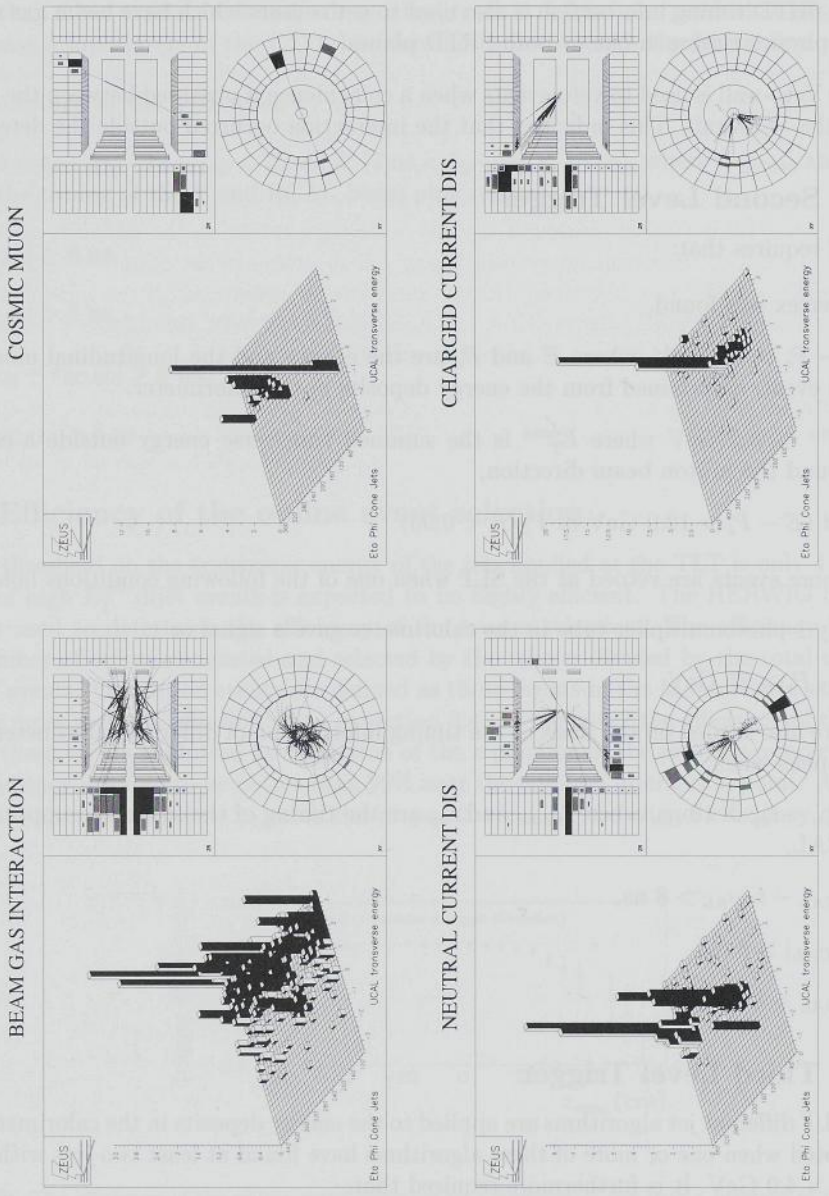

Figure 6.1: Examples of backgrounds to the dijet photoproduction selection.

- the SRTD timing information is also used to veto events which have beam gas timing and no physics timing in one or both SRTD planes,
- the Veto-wall is used to veto events when a coincidence is observed between the two planes of the Veto-wall. This indicates that the interaction occurred outside the detector.

6.1.2 Second Level Trigger

The SLT requires that:

- a vertex was found,
- $E - P_z > 8.0$ GeV, where E and P_z are the energy and the longitudinal momentum of the event, determined from the energy deposits in the calorimeter.
- $E_T^{cone} > 8.0$ GeV where E_T^{cone} is the summed transverse energy outside a cone of 10° around the proton beam direction,
- and ($E - P_z > 12.0$ GeV or $P_z/E < 0.95$).

Furthermore events are vetoed at the SLT when one of the following conditions holds:

- only 1 photomultiplier tube in the calorimeter gave a signal or
- $E - P_z > 75$ GeV.

Events are also vetoed on the basis of the timing information of different calorimeter sections[2]. This happens when:

- $t_{down} - t_{up} > 10$ ns, where t_{down} and t_{up} are the timing of the lower and upper half of the BCAL,
- $t_{FCAL} - t_{RCAL} > 8$ ns,
- $|t_{RCAL}| > 8$ ns,
- $t_{FCAL} > 8$ ns.

6.1.3 Third Level Trigger

At the TLT different jet algorithms are applied to the energy deposits in the calorimeter. Events are accepted when one or more of these algorithms have found at least two jets with $\eta^{jet} < 2.5$ and $E_T^{jet} > 4.0$ GeV. It is furthermore required that:

- the z position of the reconstructed interaction vertex is within ± 60 cm from the nominal interaction point

[2]Events can only be vetoed on the basis of the timing information of a calorimeter section when at least 1 GeV (2 GeV for the FCAL) of energy was deposited in that section. This requirement ensures that the timing was measured accurately (this requirement is also made for the timing cuts applied at the TLT)

- less than 6 bad tracks are found, where a bad track is defined as a track that has traversed at least 3 superlayers of the CTD, but does not point towards the interaction vertex.

Events are vetoed at the TLT when[3]:

- $(7 \text{ ns} < t_{FCALbp} - t_{RCALbp} < 15 \text{ ns})$ & $(7 \text{ ns} < t_{RCALbp} < 15 \text{ ns})$, where t_{FCALbp} and t_{RCALbp} are the timing of the F and RCAL beam pipe regions,
- $|t_{RCAL}| > 6$ ns,
- $|t_{FCAL}| > 8$ ns,
- $|t_{FCAl} - t_{RCAL}| > 8$ ns,
- $|t_{totalCAL}| > 8$ ns.

6.1.4 Efficiency of the online event selection

Since the threshold on the transverse energy of the jets applied at the TLT is only 4 GeV, the selection of high E_T^{jet} dijet events is expected to be highly efficient. The HERWIG 5.9 Monte Carlo was used to determine the efficiency of the trigger selection. The efficiency is defined as the number of events generated and selected by the trigger divided by the total number of generated events. Generated events are defined as those events in the Monte Carlo sample that satisfy the cross section definition given in section 3.4. In figure 6.2 the efficiency of the trigger to accept these events is plotted as a function of the z position of the primary interaction. The trigger efficiency is found to be better than 99% near the nominal interaction point. Away from the nominal interaction point, in particular at positive z_{vertex}, the trigger efficiency degrades.

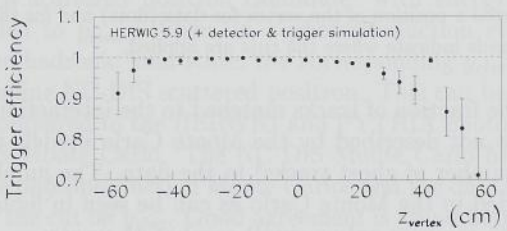

Figure 6.2: The efficiency of the online event selection as a function of the true z position of the primary interaction. The efficiency has been determined from the HERWIG 5.9 Monte Carlo.

[3]In reality the conditions applied at the TLT are more complicated since they take into account the timing resolution. E.g. the condition $|t_{RCAL}| > 6$ ns is in reality $|t_{RCAL}| > max(6 \text{ ns}, 3\sigma_{t_{RCAL}})$, where $\sigma_{t_{RCAL}}$ is the timing resolution.

6.2 The offline event selection

After correction for detector effects, the data is subjected to more stringent selection criteria. The cuts made on different observables are motivated by comparing data and Monte Carlo. In all figures the numbers of events observed in the data are compared to the corresponding numbers of events in the Monte Carlo, which has been scaled to the luminosity of the 1995 run. Each distribution is submitted to all selection criteria described in this section, excluding the cut on the observable that is plotted. Only the statistical errors on the data are shown.

To remove background due to proton beam gas interactions or cosmic showers, cuts are applied on the z position of the reconstructed interaction vertex and on the relative number of tracks that can be matched to this vertex. In figure 6.3 the distribution of the z position of the vertex is compared to the Monte Carlo, which describes the data well. The requirement made on the vertex position is:

$$-40\,\text{cm} < z_{vertex} < 40\,\text{cm}\,. \tag{6.1}$$

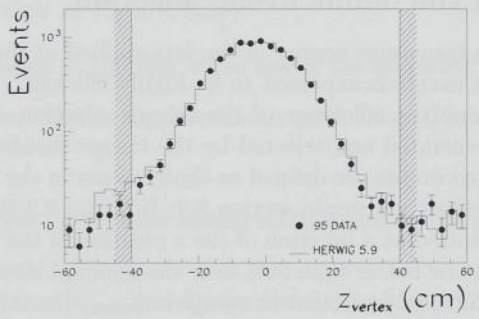

Figure 6.3: The reconstructed z position of the vertex for data (dots) and for the HERWIG 5.9 Monte Carlo (histogram). The hatched bands indicate where the cuts are applied.

The distribution of the fraction of tracks matched to the interaction vertex is given in figure 6.4a. The distribution is not described by the Monte Carlo models to which it is compared. This is due to a larger number of ghost tracks[4] in the data. The number of tracks matched to the vertex is well described in the Monte Carlo as can be seen in figure 6.4b. The cut applied to the distribution in 6.4a removes only a small number of events:

$$\frac{\text{number of vertex fitted tracks}}{\text{total number of tracks}} > 0.1\,. \tag{6.2}$$

The rejection of NC-DIS events is based on the different reconstruction methods for the variable y. If the scattered positron is detected, its energy and scattering angle can be used to

[4]ghost tracks are tracks which do not correspond to the trajectory of a physical particle but occur because of the combination of hits from different particles or noise hits.

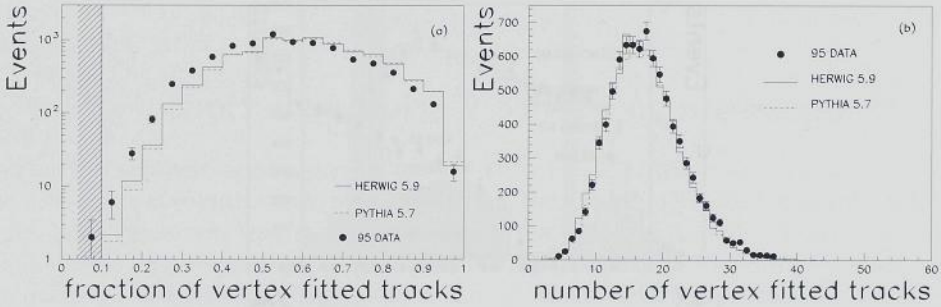

Figure 6.4: Figure (a) shows the fraction of vertex fitted tracks in the data (dots) and in HERWIG 5.9 and PYTHIA 5.7. The hatched band indicates where the cut is applied. Figure (b) shows the absolute number of vertex fitted tracks for data and Monte Carlo.

determine y, using the formula:

$$y_{elec} = 1 - \frac{E'_e}{2E_e}(1 - \cos\theta'_e) \; . \tag{6.3}$$

The variable y can also be reconstructed from the hadronic final state, using the Jacquet-Blondel formula [74]:

$$y_{JB} = \frac{\sum_{hadrons}(E - P_z)}{2E_e} \, , \tag{6.4}$$

where the sum runs over all objects in the hadronic final state. Since in photoproduction events the scattered positron escapes detection in the central detectors, the hadronic final state is taken to be the sum over all ZUFOs.

For events in which a scattered positron candidate[5] with energy greater than 5 GeV is identified, a cut is applied to y_{elec}. When, in a photoproduction event, an electromagnetic cluster is identified in the hadronic final state, the corresponding y_{elec} value will in general be higher than that of a genuine NC-DIS scattered positron. This can be seen in figure 6.5 where the y_{elec} distribution is compared to the HERWIG and PYTHIA photoproduction Monte Carlo models and to a NC-DIS Monte Carlo. The NC-DIS Monte Carlo has been subjected to the same selection cuts as the photoproduction Monte Carlos and the data, i.e. to all cuts described in this section except for the cut on y_{elec}. Good agreement is found between data and HERWIG 5.9 at high y_{elec} values. At low y_{elec} values NC-DIS events dominate. PYTHIA 5.7 predicts less scattered positrons than are observed, this effect will be discussed in more detail in section 6.3.2. Events are rejected when:

$$y_{elec} < 0.7 \, . \tag{6.5}$$

In figure 6.6 the y_{JB} distribution is compared to the two Monte Carlo models. Below $y_{JB} = 0.85$ both are in good agreement with the data. As y_{JB} approaches 1 the contribution

[5]Electromagnetic candidates identified by the electron finding algorithm described in [77] are considered for this cut.

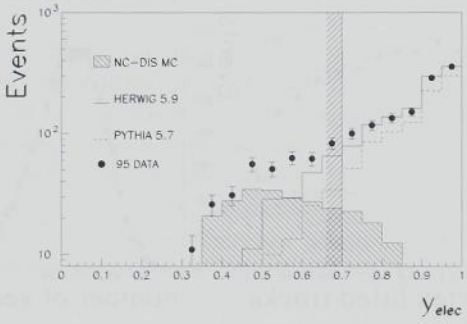

Figure 6.5: y_{elec} spectrum for events in which a scattered positron candidate was identified with energy greater than 5 GeV. The hatched band indicates where the cut is applied.

of NC-DIS events becomes important. For NC-DIS events y_{JB} peaks around 1, because the energy of the scattered positron is taken as a part of the hadronic final state in the calculation of y_{JB}. For the event selection it is required that

$$0.20 < y_{JB} < 0.85\,. \tag{6.6}$$

This removes NC-DIS events, for which y_{JB} peaks near 1 and beam gas interactions which have mostly low y_{JB} values.

The rejection of NC-DIS events using the cuts on y_{elec} and y_{JB} makes use of the fact that the scattered positron energy is deposited in the CAL, while for photoproduction events the positron escapes detection, due to its smaller scattering angle. The effective cut on the scattering angle of the positron and therefor on the virtuality of the exchanged photon is determined by the geometry of the beam pipe hole in the RCAL. Effectively, the cuts on y_{elec} and y_{JB} restrict the range of the virtuality of the exchanged photon to $Q^2 \lesssim 1$ GeV^2, with a median Q^2 of 10^{-3} GeV^2.

To remove CC-DIS events, a cut is applied on the missing transverse momentum, which has been scaled with the inverse square root of the deposited energy to account for the calorimeter resolution. The distribution of $P_T/\sqrt{E_T}$, to which the missing momentum cut is applied, is shown in figure 6.7. Data and Monte Carlo are in good agreement. Events are rejected when:

$$\frac{P_T}{\sqrt{E_T}} > 1.5\,\sqrt{\text{GeV}}\,. \tag{6.7}$$

Summarising:

- we have applied cuts to the z position of the vertex and to the fraction of tracks matched to the vertex to remove non-physics backgrounds,
- cuts on y_{elec} and y_{JB} remove NC-DIS background and
- CC-DIS background is removed with a cut on the missing transverse momentum.

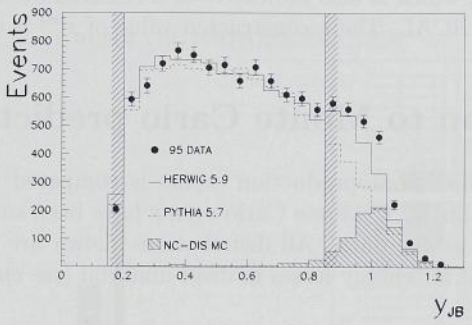

Figure 6.6: y_{JB} spectrum compared to the Monte Carlo predictions. The hatched bands indicate where the cuts are applied.

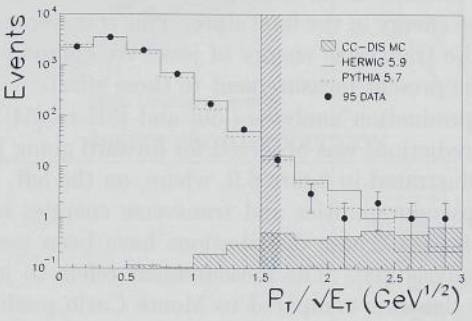

Figure 6.7: The total P_T of events from the data and from the Monte Carlo models, scaled by $1/\sqrt{E_T}$. The hatched band indicates where the cut is applied.

To the selected sample of dijet candidate events we apply the k_T clustering jet reconstruction algorithm. A sample of 8690 events is selected in which at least two jets are found with:

- $-1 < \eta^{jet} < 2$,
- $E^{jet}_{T\,leading} > 14$ GeV, where $E^{jet}_{T\,leading}$ is the transverse energy of the highest transverse energy jet,
- $E^{jet}_{T\,second} > 11$ GeV, where $E^{jet}_{T\,second}$ is the transverse energy of the second highest transverse energy jet.

In figure 6.8 examples of a resolved and a direct dijet event are shown. Both events have a clear two jet signature. In the resolved photoproduction event, hadronic energy is deposited near the RCAL beam pipe. This energy is associated with the photon remnant. The value of

x_γ^{obs} for this event is 0.74, which is also indicative of a resolved event. For the direct event no energy is observed in the RCAL. The reconstructed value of x_γ^{obs} is 0.96.

6.3 Comparison to Monte Carlo predictions

The selected sample of dijet photoproduction events is compared to the Monte Carlo event samples described in section 3.3.1. Monte Carlo events have been subjected to the same online and offline selection cuts as the data. All distributions shown are determined using ZUFOs, which have been corrected for energy losses in dead material (see chapter 5).

6.3.1 Multi-parton scattering effects

In resolved photoproduction, like in hadroproduction, interactions, in addition to the hard partonic scattering, can occur between partons inside the colliding particles or their remnants. These processes, usually referred to as underlying events or multi-parton interactions (MI), cause additional transverse energy in the final state. This transverse energy enters as a pedestal in the determination of the transverse energy of jets. We compare data and Monte Carlo to study the sensitivity of the present measurement to these effects.

In previous jet photoproduction analyses ([30] and [51] to [54]) an excess of events with respect to Monte Carlo predictions was observed for forward going jets, or correspondingly for low x_γ^{obs} values. This is illustrated in figure 6.9, where, on the left, the transverse energy flow around jets at different pseudorapidities and transverse energies is shown and on the right, the x_γ^{obs} distribution is shown. These distributions have been measured in the ZEUS 1994 photoproduction dijet analysis [53]. The measurement refers to jets with transverse energy greater than 6 GeV. The data are compared to Monte Carlo predictions with and without a simulation of multi-parton interactions. The transverse energy flow around jets is plotted as a function of the distance in pseudorapidity with respect to the jet axis and is integrated between $\phi^{jet}-1$ and $\phi^{jet}+1$. They show that for low transverse energy jets a Monte Carlo without multi-parton interactions underestimates the energy flow around the jets. The inclusion of a model simulating these effects in the Monte Carlo improves the description of the data. Similarly for x_γ^{obs} it is clear that the Monte Carlo model without MI underestimates the jet cross section for $x_\gamma^{obs} < 0.3$. When multi-parton interactions are included the description is improved, although the data is still underestimated.

In the 1994 dijet analysis, and also in other analyses, it has thus been demonstrated that Monte Carlo models, including a simulation of multi-parton interactions, describe the data better in the regions most sensitive to these effects. In the present analysis, where jets are studied at much higher transverse energies, we will show that there are no indications that multi-parton interactions play a role in the determination of jet cross sections.

In figure 6.10 the transverse energy flow around jets is shown as a function of the distance in pseudorapidity to η^{jet}, integrated between $\phi^{jet}-1$ and $\phi^{jet}+1$. The transverse energy flows are shown in bins of E_T^{jet} and x_γ^{obs}. The jets are strongly collimated, with relatively little transverse energy outside the jets. Comparisons to the HERWIG predictions show a reasonable agreement even though no simulation of multi-parton interactions has been included in the Monte Carlo.

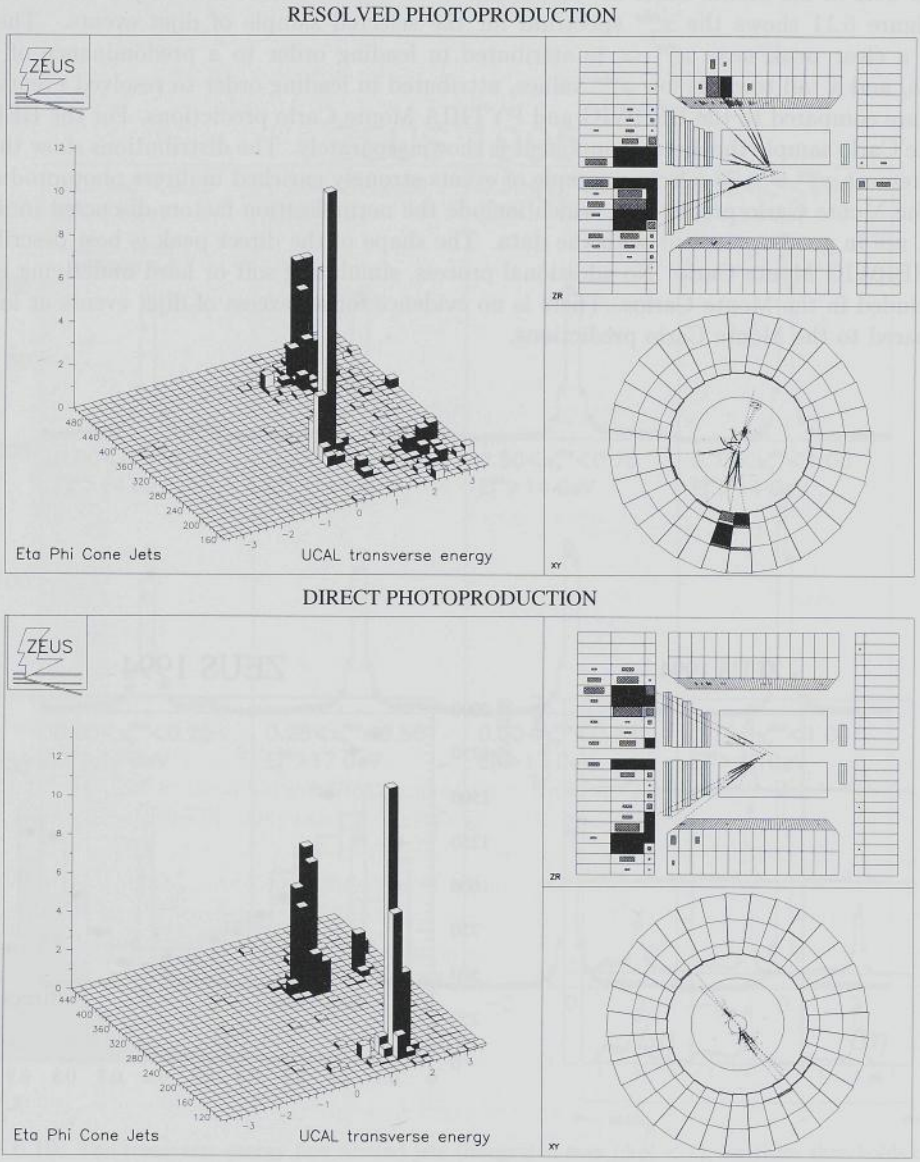

Figure 6.8: Examples of resolved and direct photoproduction events.

Only at low x_γ^{obs} values the energy flow outside jets is slightly underestimated by the Monte Carlo. Jets in the Monte Carlo are also found to be slightly narrower than jets in the data.

Figure 6.11 shows the x_γ^{obs} spectrum for the selected sample of dijet events. The data show a clear peak near $x_\gamma^{obs} \approx 1$, attributed in leading order to a predominance of direct events, and a tail towards low x_γ^{obs} values, attributed in leading order to resolved events. The data are compared to the HERWIG and PYTHIA Monte Carlo predictions. For the HERWIG Monte Carlo sample the direct component is shown separately. The distributions show that the requirement $x_\gamma^{obs} > 0.75$ selects a sample of events strongly enriched in direct photoproduction.

The Monte Carlo predictions, which include the normalisation factors discussed in section 3.3.1, are in good agreement with the data. The shape of the direct peak is best described in the HERWIG Monte Carlo. No additional process, simulating soft or hard underlying events, is included in the Monte Carlos. There is no evidence for an excess of dijet events at low x_γ^{obs} compared to the Monte Carlo predictions.

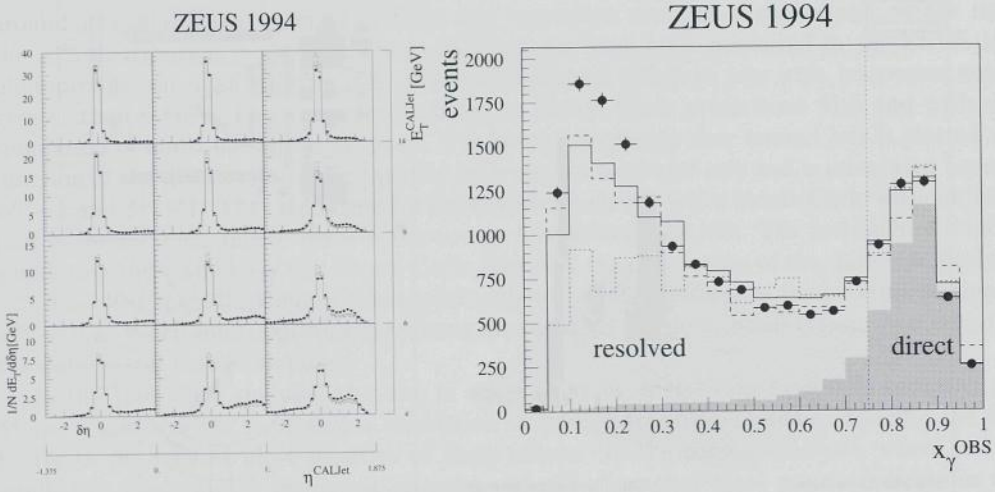

Figure 6.9: The left plot shows the transverse energy flow around jets from the 1994 dijet analysis, integrated over $|\Delta\phi| < 1$ and in bins of the pseudorapidity and the transverse energy of the jet. The data (dots) are compared to HERWIG with (full histogram) and without MI (dashed histogram). In the right plot the x_γ^{obs} distribution is shown. The data (dots) are compared to the following Monte Carlo predictions: HERWIG without MI (dotted histogram) and HERWIG (full histogram) and Pythia (dashed histogram) with MI.

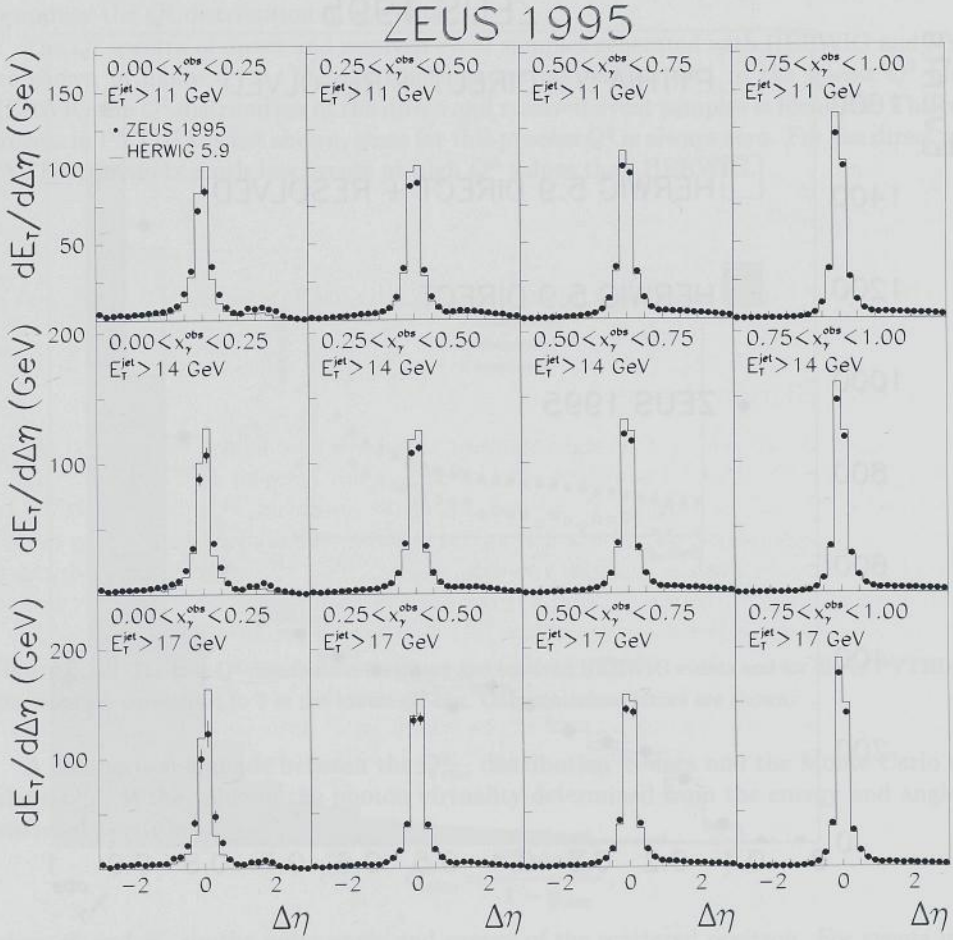

Figure 6.10: The transverse energy flow around jets (integrated over $|\Delta\phi| < 1$), for three thresholds on the transverse energy of the jet and in four bins in x_γ^{obs}. The data are compared to the HERWIG 5.9 predictions. For the data only statistical errors are shown.

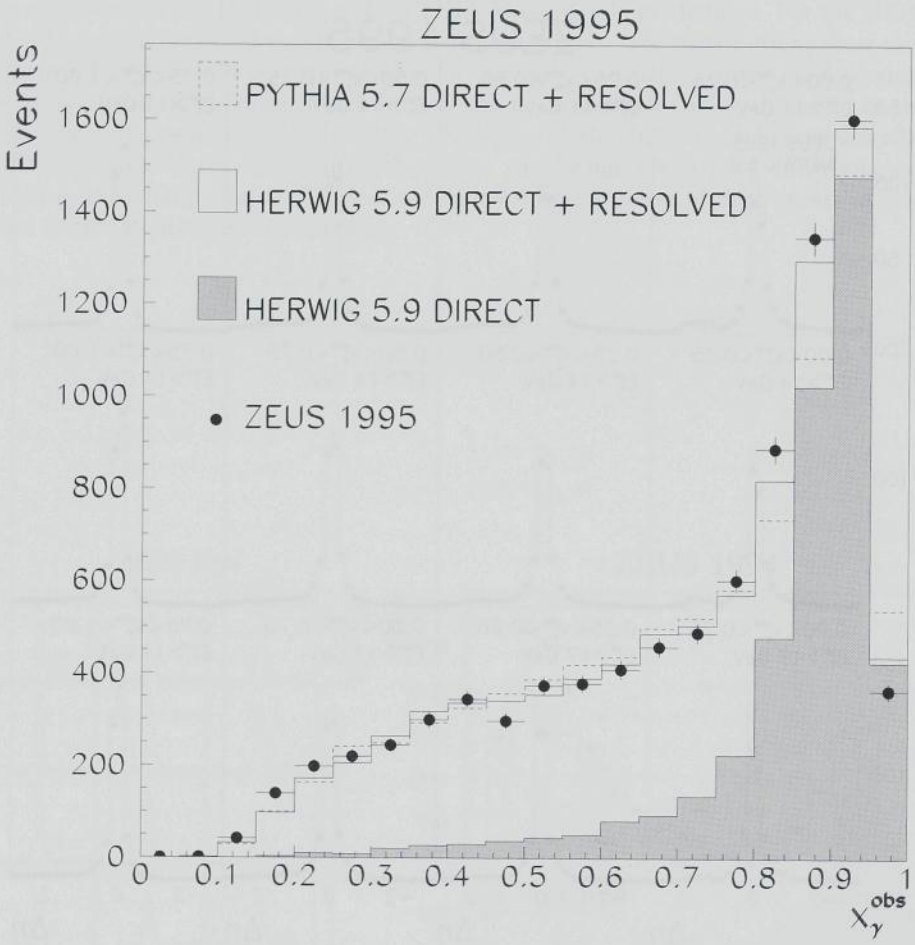

Figure 6.11: The x_γ^{obs} spectrum of the selected dijet sample, compared to the HERWIG 5.9 and the PYTHIA 5.7 Monte Carlo predictions. The direct component from the HERWIG Monte Carlo is shown separately as the shaded histogram. Only statistical errors are shown.

6.3.2 The Q^2 distribution

As discussed earlier in this chapter, the selection cuts on y_{elec} and y_{JB} effectively form a restriction on the photon virtuality Q^2. In section 3.3.1 it was mentioned that the Monte Carlo models used in this analysis have a somewhat different approach to the generation of the photon spectrum radiated from the incoming positron beam. We therefore study how well the models reproduce the Q^2 distribution in the data.

The Q^2 spectra of direct and resolved event samples generated with HERWIG and PYTHIA are shown in figure 6.12. The distributions are normalised to 1 in the lowest Q^2 bin. For HERWIG the Q^2 distribution of the direct and resolved event samples is identical. The resolved process in PYTHIA is not shown, since for this process Q^2 is always zero. For the direct process, PYTHIA predicts much less events at high Q^2 values than HERWIG.

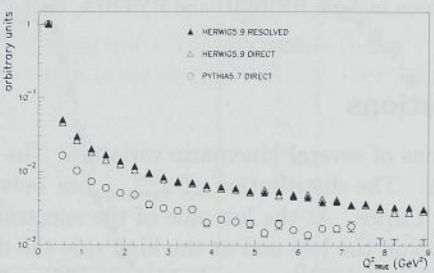

Figure 6.12: The true Q^2 distribution for direct and resolved HERWIG events and for direct PYTHIA events. The plots are normalised to 1 in the lowest Q^2 bin. Only statistical errors are shown.

A comparison is made between the Q^2_{elec} distribution in data and the Monte Carlo models, where Q^2_{elec} is the value of the photon virtuality determined from the energy and angle of the scattered positron.

$$Q^2_{elec} = \frac{E'^2_e \sin \theta'^2_e}{1 - y_{elec}}, \tag{6.8}$$

where θ'_e and E'_e are the polar angle and energy of the scattered positron. For events in which a scattered positron candidate, with $E'_e > 5$ GeV and $\theta'_e > 140°$, is found, the Q^2_{elec} distribution is plotted (figure 6.13). For this study the dijet selection cuts on y_{elec} and y_{JB} have not been applied. As expected from the true Q^2 spectra PYTHIA predicts much less positrons observed in the calorimeter than HERWIG. The HERWIG prediction agrees best with the data, although it overestimates the number of scattered positrons observed.

The effect of a poor simulation of the Q^2 spectrum on the unfolding of the cross section (see section 7) was tested by changing the HERWIG Q^2 distribution to that of PYTHIA, and was found to be very small.

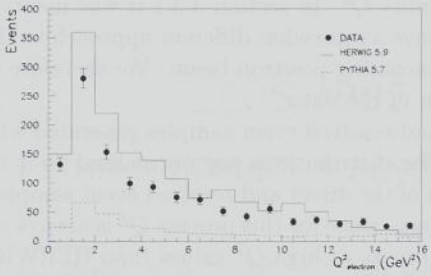

Figure 6.13: The Q^2_{elec} distribution in data, HERWIG and PYTHIA. Only the statistical errors for data are shown.

6.3.3 Other distributions

Figure 6.14 shows distributions of several kinematic variables. The figures (a) and (b) are the x_γ^{obs} and x_{proton}^{obs} distributions. The distribution of x_{proton}^{obs} lies between 10^{-2} and 10^{-1} and is well described by the Monte Carlos. At the low side of the spectrum, x_{proton}^{obs} is limited by the transverse energy requirement on the jets and at the high side the distribution reflects the fast decrease of the proton's parton densities towards high x. The x_γ^{obs} spectrum was discussed in detail above already. In figures (c) and (d) the average pseudorapidity of the jets and the absolute pseudorapidity difference between the jets is plotted. The average pseudorapidity is well described by both models. The pseudorapidity difference is described well by HERWIG, while PYTHIA predicts a broader distribution. The figures (e) and (f) show the transverse energy distributions of the leading jet and of the second jet. Both distributions fall rapidly with increasing E_T and are well described by the Monte Carlo models.

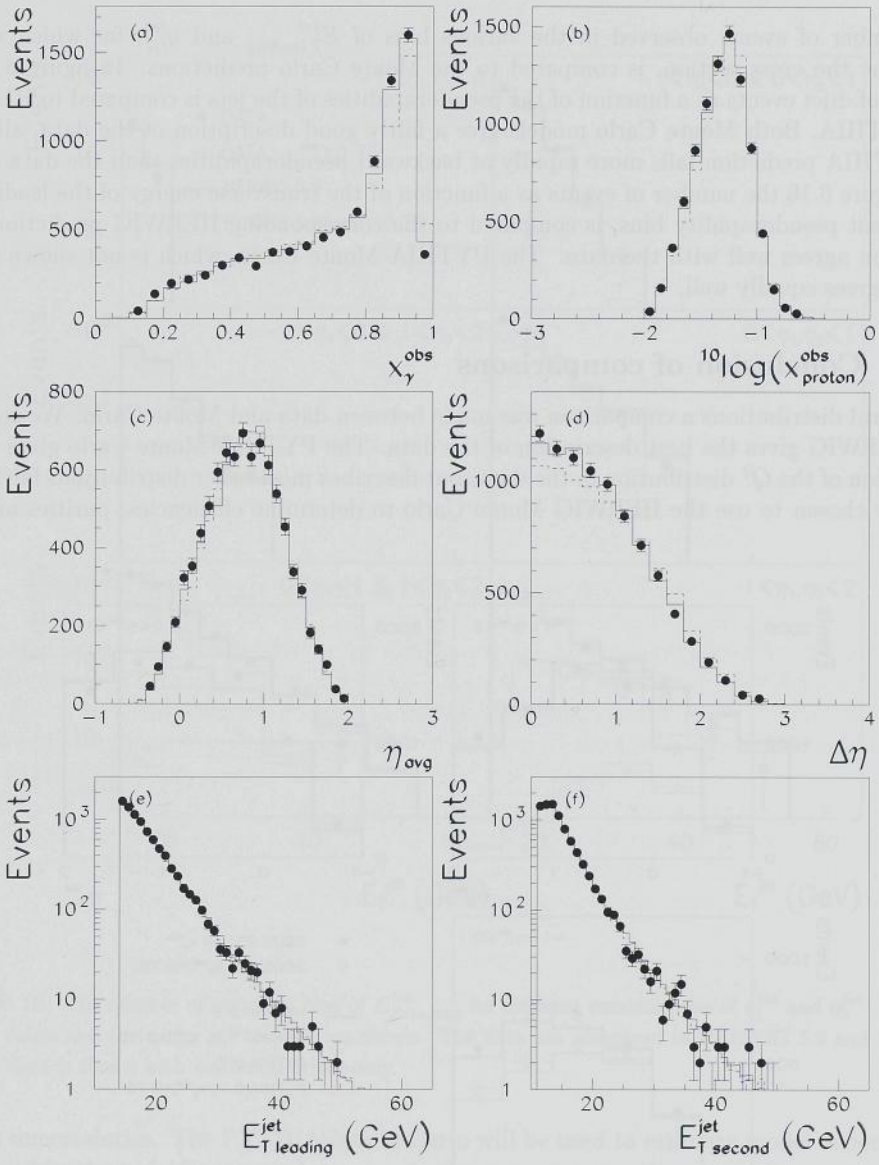

Figure 6.14: Distributions of: x_γ^{obs} (a), x_{proton}^{obs} (b), the average pseudorapidity of the jets (c), the absolute pseudorapidity difference between the jets (d) and the transverse energy of the highest (e) and second highest (f) transverse energy jet. The data are compared to the distributions in HERWIG 5.9 (full histograms) and PYTHIA 5.7 (dashed histograms).

6.3.4 The uncorrected cross sections

The number of events observed in the various bins of $E_{T\,leading}^{jet}$ and $\eta_{1,2}^{jet}$, for which we will determine the cross section, is compared to the Monte Carlo predictions. In figure 6.15 the number of dijet events as a function of the pseudorapidities of the jets is compared to HERWIG and PYTHIA. Both Monte Carlo models give a fairly good description of the data, although the PYTHIA prediction falls more rapidly at backward pseudorapidities than the data.

In figure 6.16 the number of events as a function of the transverse energy of the leading jet, in different pseudorapidity bins, is compared to the corresponding HERWIG prediction. The prediction agrees well with the data. The PYTHIA Monte Carlo, which is not shown on the figure, agrees equally well.

6.3.5 Conclusion of comparisons

For several distributions a comparison was made between data and Monte Carlo. We conclude that HERWIG gives the best description of the data. The PYTHIA Monte Carlo gives a poor description of the Q^2 distribution in the data, but describes most other distributions fairly well. We have chosen to use the HERWIG Monte Carlo to determine efficiencies, purities and sys-

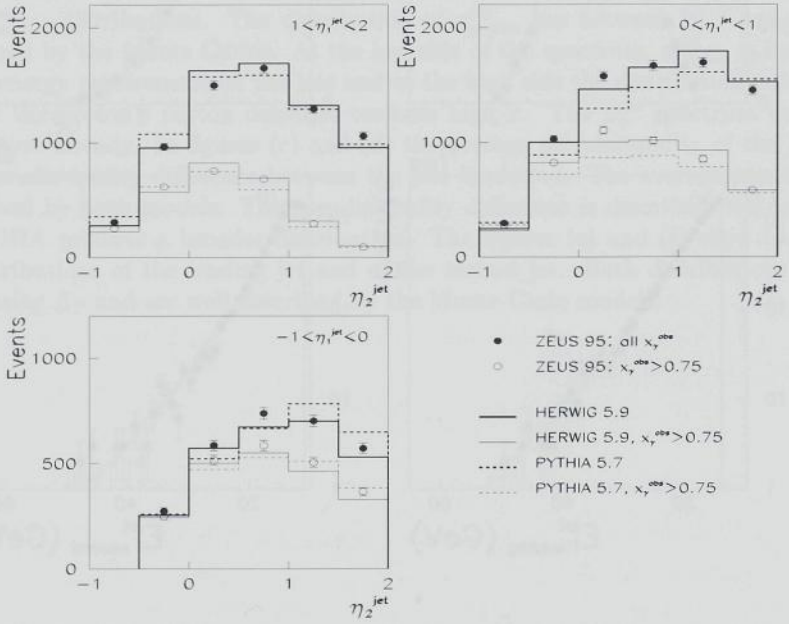

Figure 6.15: The number of events in bins of η_2^{jet} for fixed η_1^{jet}, for the full x_γ^{obs} range and for $x_\gamma^{obs} > 0.75$. The data are compared to HERWIG 5.9 and PYTHIA 5.7. The data is shown with statistical errors only.

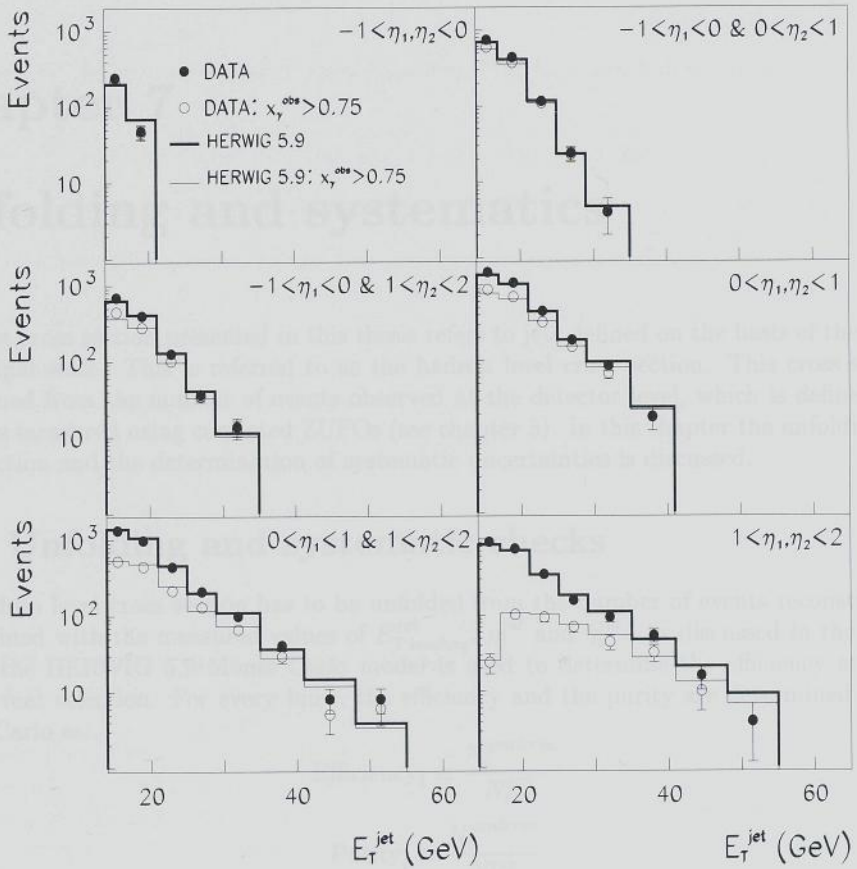

Figure 6.16: The number of events in bins of $E_{T\,leading}^{jet}$ for different combinations of η_1^{jet} and η_2^{jet}. Both the full x_γ^{obs} range and the range $x_\gamma^{obs} > 0.75$ are shown. The data are compared to HERWIG 5.9 and PYTHIA 5.7. The data is shown with statistical errors only.

tematic uncertainties. The PYTHIA Monte Carlo will be used to estimate model dependencies introduced in the unfolding procedure.

Chapter 7

Unfolding and systematics

The dijet cross section presented in this thesis refers to jets defined on the basis of the hadrons in the final state. This is referred to as the hadron level cross section. This cross section is determined from the number of events observed at the detector level, which is defined by the variables measured using corrected ZUFOs (see chapter 5). In this chapter the unfolding of the cross section and the determination of systematic uncertainties is discussed.

7.1 Unfolding and systematic checks

The hadron level cross section has to be unfolded from the number of events reconstructed in bins defined with the measured values of $E_{T\,leading}^{jet}$, η_1^{jet} and η_2^{jet}. As discussed in the previous section the HERWIG 5.9 Monte Carlo model is used to determine the efficiency and purity of the event selection. For every bin i, the efficiency and the purity are determined from the Monte Carlo as:

$$\text{Efficiency}_i \equiv \frac{N_i^{gen\&rec}}{N_i^{gen}} \tag{7.1}$$

$$\text{Purity}_i \equiv \frac{N_i^{gen\&rec}}{N_i^{rec}} \tag{7.2}$$

where N_i^{gen}, N_i^{rec} are the number of events generated or reconstructed in bin i and $N_i^{gen\&rec}$ is the number of events generated and reconstructed in bin i. In a bin-by-bin unfolding procedure the number of events in hadron level bin i is estimated from the number of events observed in the corresponding detector level bin i, using the formula:

$$N_i^{true} = N_{i\,data}^{rec} \left(\frac{\text{Purity}_i}{\text{Efficiency}_i} \right)_{Monte\ Carlo} = N_{i\,data}^{rec} \times \left(\frac{N_i^{gen}}{N_i^{rec}} \right)_{Monte\ Carlo} \tag{7.3}$$

The outcome of the unfolding procedure can depend on the Monte Carlo model. When this model does not describe the data, the correction for bin-to-bin migrations becomes model dependent. For the cross section presented here the uncertainty related to the Monte Carlo model has been estimated by making the following variations in the unfolding procedure:

- a different Monte Carlo generator, PYTHIA 5.7, was used,

- another parametrisation of the parton densities in the photon was used in HERWIG,
- the HERWIG Monte Carlo was used without the direct and resolved normalisation factors discussed in section 3.3.1.

To determine further systematic uncertainties the event selection was varied. The variations include:

- a variation of the vertex range between ± 30 cm and ± 50 cm,
- the cut on the fraction of vertex fitted tracks was raised to 0.2 and was removed,
- the cut on the missing transverse momentum was varied between $\frac{P_T}{\sqrt{E_T}} < 1.2\sqrt{\mathrm{GeV}}$ and $\frac{P_T}{\sqrt{E_T}} < 1.8\sqrt{\mathrm{GeV}}$,
- the cut on y_{elec} was varied between $y_{elec} > 0.8$ and $y_{elec} > 0.6$.

There is also a systematic uncertainty related to the fact that the measured (and corrected) values of y_{JB} and E_T^{jet} have a bias with respect to the true values (see also the figures in section 5). To estimate the effect this may have on the unfolded cross sections the reconstructed:

- y_{JB} was varied by $\pm 5\%$,
- E_T of the jets was varied by $\pm 3\%$,

These variations are applied to both data and Monte Carlo.

To estimate the systematic uncertainty related to a possible hadronic energy scale difference between data and Monte Carlo, the reconstructed transverse jet energies and y_{JB}, in the Monte Carlo, have been varied by $\pm 3\%$ simultaneously and by $\pm 2\%$ separately.

The effect on the cross section due to these variations is shown, for every bin, in figures 7.1 to 7.3. Each variation corresponds to a bin on the x axis of the plotted figures, as indicated on the first figure. The largest systematic fluctuations are due to the energy scale uncertainty and the use of PYTHIA instead of HERWIG in the unfolding procedure. Since the energy scale uncertainty is strongly correlated from bin to bin, it is shown as an error band on the cross section figures. The positive (and negative) fluctuations, resulting from all other variations, are added in quadrature to yield the total positive (and negative) systematic uncertainty. The total systematic uncertainty and the energy scale uncertainty band are shown in figure 7.4 and 7.5. We find that over most of the kinematic regime, with an exception of the highest transverse energy bins, the systematic uncertainties are between 10 and 20%.

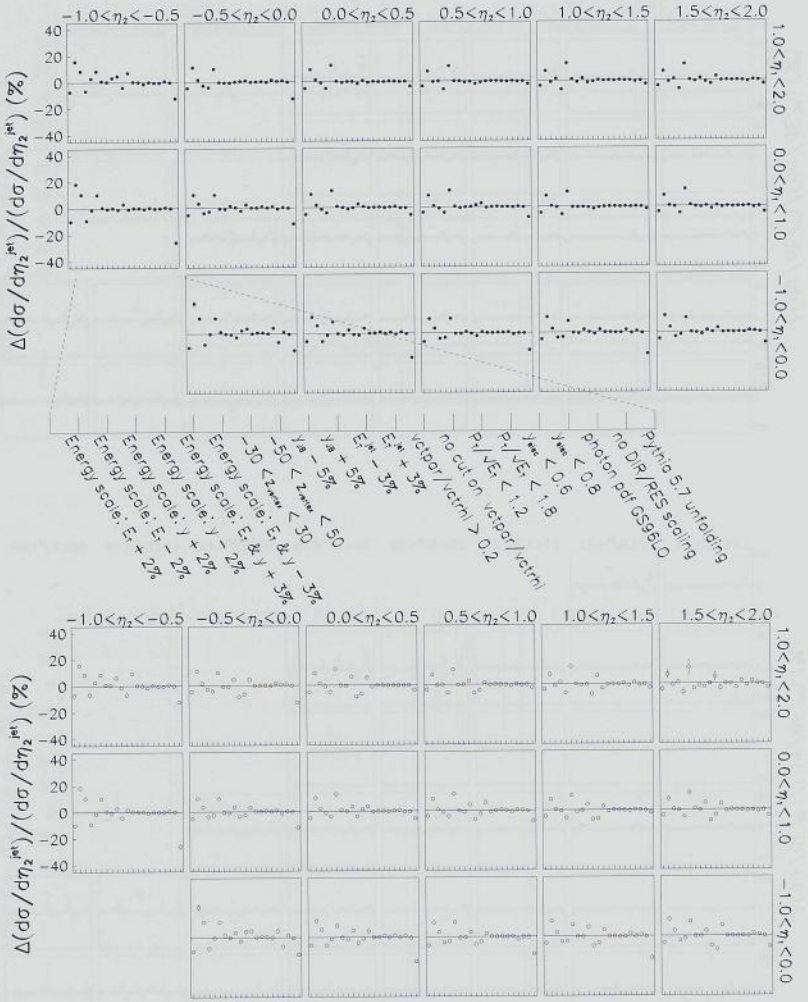

Figure 7.1: The relative effect of various systematic variations in the analysis on the cross section $d\sigma/d\eta_2^{jet}$ for $0.20 < y < 0.85$. The upper plots correspond to the cross section over the full x_γ^{obs} range and the lower plots correspond to the range $x_\gamma^{obs} > 0.75$.

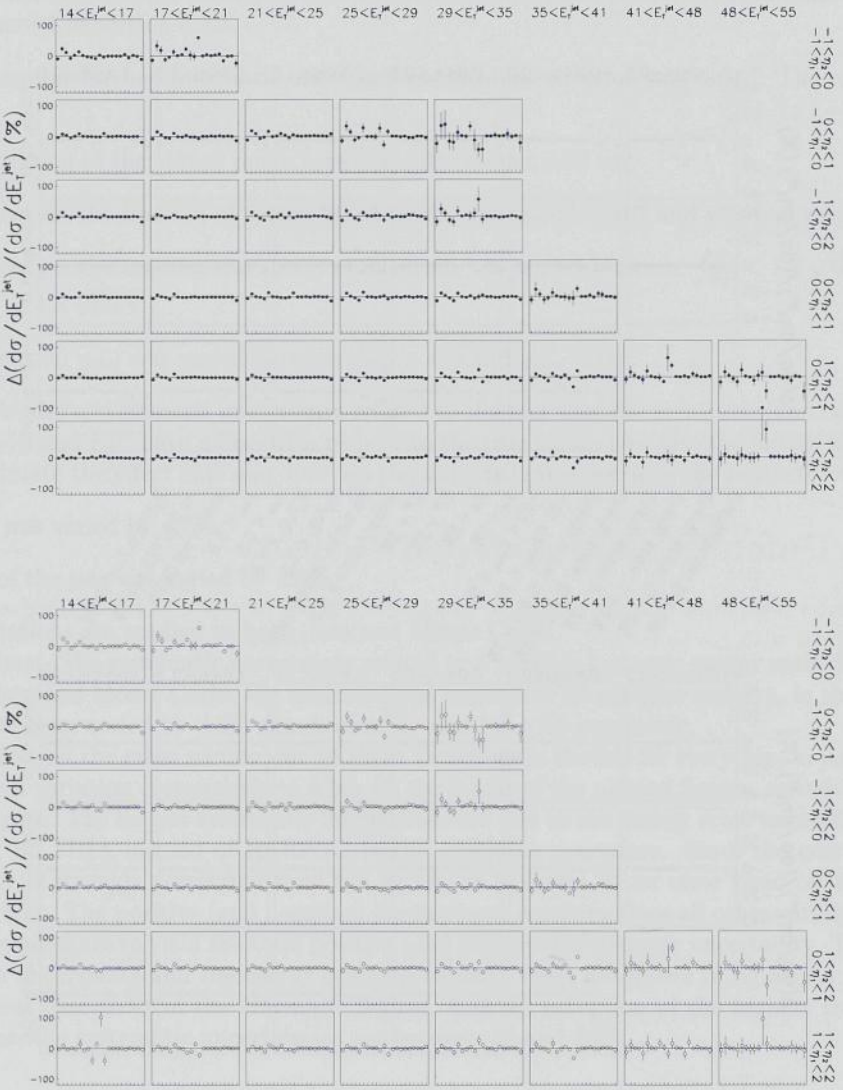

Figure 7.2: The relative effect of various systematic variations (see figure 7.1) in the analysis on the cross section $d\sigma/dE_T^{jet}$ for $0.20 < y < 0.85$. The upper plots correspond to the cross section over the full x_γ^{obs} range and the lower plots correspond to the range $x_\gamma^{obs} > 0.75$.

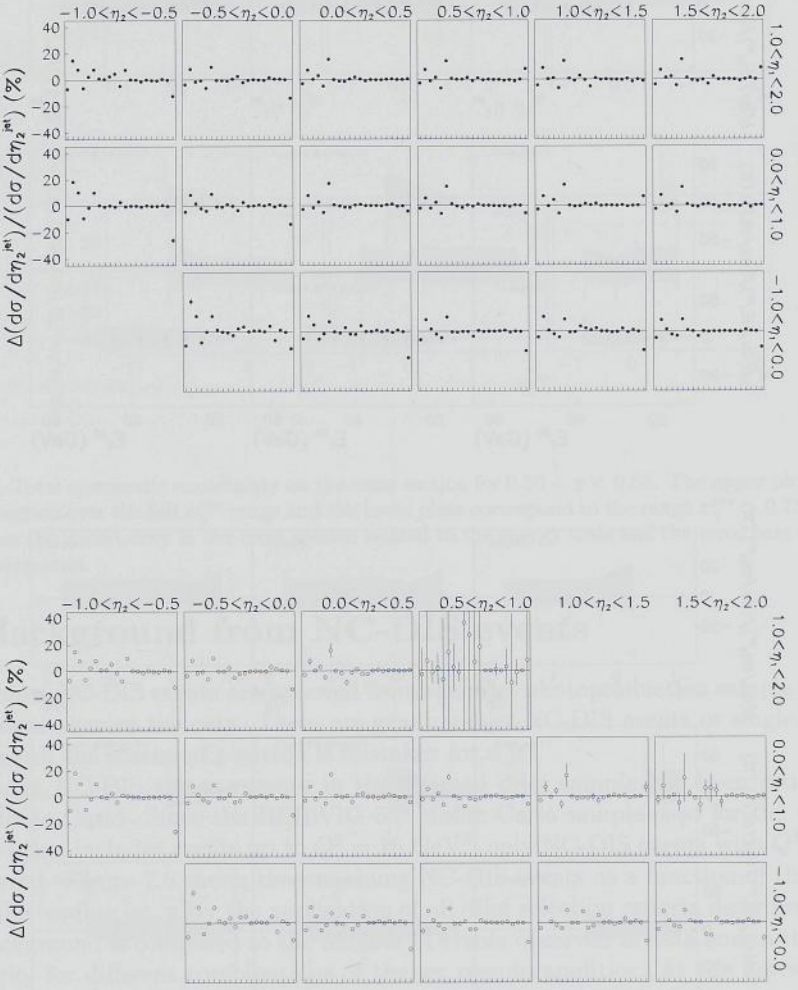

Figure 7.3: The relative effect of various systematic variations (see figure 7.1) in the analysis on the cross section $d\sigma/d\eta_2^{jet}$ for $0.50 < y < 0.85$. The upper plots correspond to the cross section over the full x_γ^{obs} range and the lower plots correspond to the range $x_\gamma^{obs} > 0.75$.

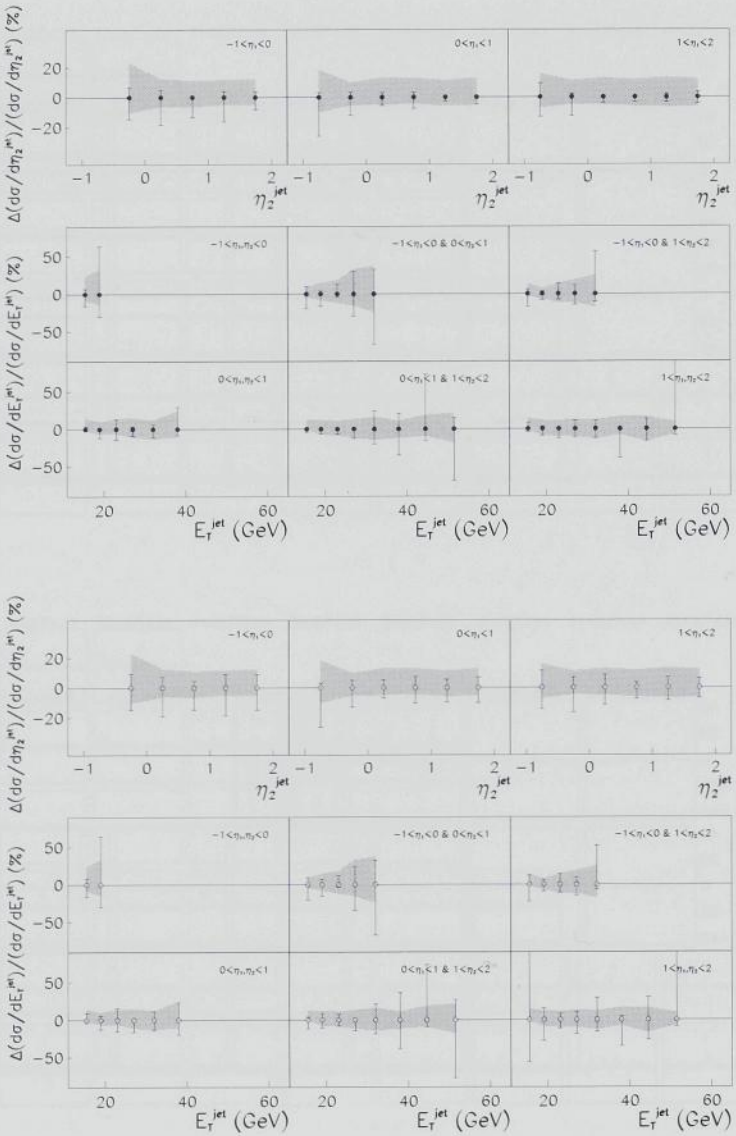

Figure 7.4: Total systematic uncertainty on the cross section for $0.20 < y < 0.85$. The upper plots correspond to the cross section over the full x_γ^{obs} range and the lower plots correspond to the range $x_\gamma^{obs} > 0.75$. The shaded band indicates the uncertainty on the cross section related to the energy scale and the error bars correspond to the other systematics.

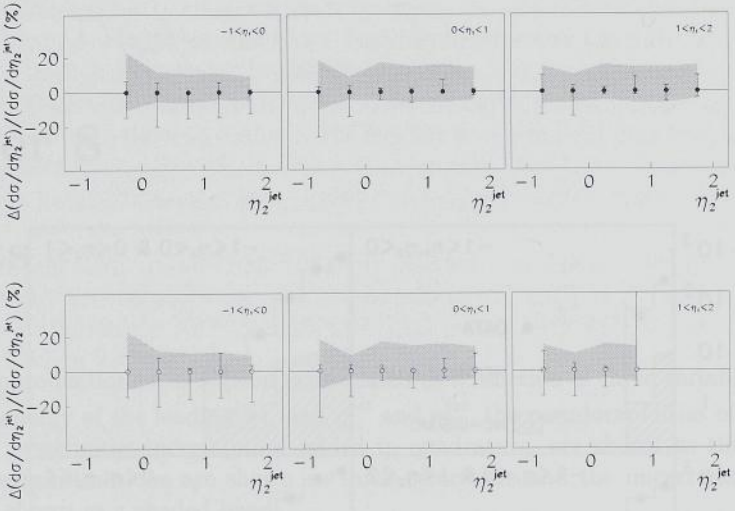

Figure 7.5: Total systematic uncertainty on the cross section for $0.50 < y < 0.85$. The upper plots correspond to the cross section over the full x_γ^{obs} range and the lower plots correspond to the range $x_\gamma^{obs} > 0.75$. The shaded band indicates the uncertainty in the cross section related to the energy scale and the error bars correspond to the other systematics.

7.2 Background from NC-DIS events

Although most NC-DIS events are removed from the dijet photoproduction sample in the event selection, some survive the cuts. These are genuine dijet NC-DIS events or single jet NC-DIS events in which the scattered positron is mistaken for a jet.

How many NC-DIS events remain in the selected dijet sample has been estimated from NC-DIS Monte Carlo. Since the HERWIG 5.9 Monte Carlo sample used for the unfolding of the cross section includes events up to $Q^2 = 16$ GeV^2, only NC-DIS events with $Q^2 > 16$ GeV^2 are considered. Figure 7.6 shows the remaining NC-DIS events as a function of the transverse energy of the leading jet, after the application of all dijet selection criteria described in chapter 6. This background is compared to the number of events observed in data and in the HERWIG Monte Carlo, for different combinations of the jet pseudorapidities. At the lowest transverse energies the background from NC-DIS events is less than 1%. With increasing transverse energies the background contamination increases up to 10-15% in the highest transverse energy bins. In these bins, however, statistical and systematic uncertainties are much larger than 20%, therefore no subtraction of the NC-DIS background was performed.

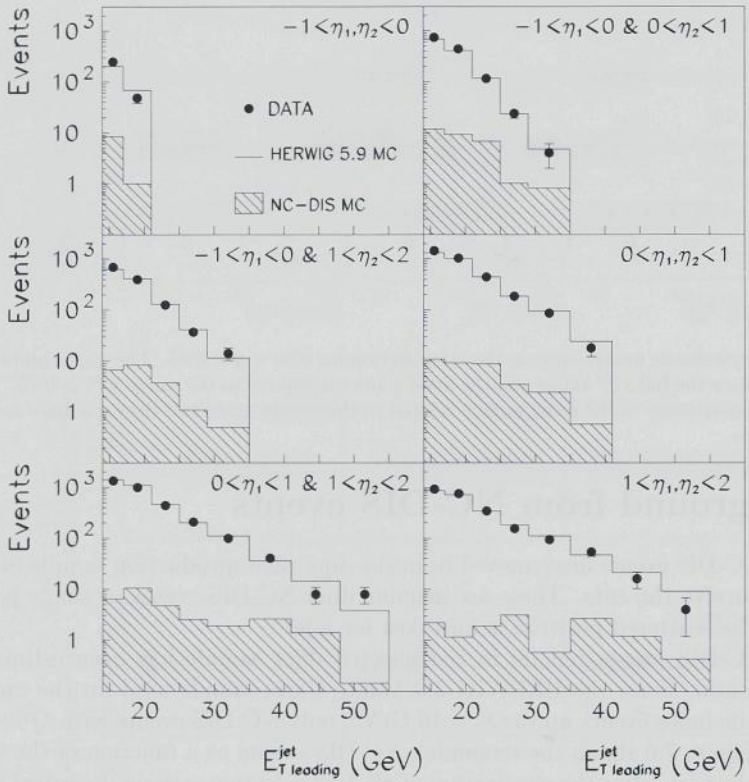

Figure 7.6: The number of events as a function of $E^{jet}_{T\,leading}$ in different ranges of the pseudorapidities of the jets, for data (dots) and for the HERWIG (open histogram) and NC-DIS (hatched histogram) Monte Carlo models, after application of the selection criteria described in chapter 6.

Chapter 8

Results

The dijet photoproduction cross section is presented as a function of three variables: $E_{T\,leading}^{jet}$, the transverse energy of the leading jet, and η_1^{jet} and η_2^{jet}, the pseudorapidities of the two jets. Statistical and systematic uncertainties, added in quadrature, are shown as thin error bars. Statistical uncertainties alone are shown as thick error bars and the uncertainty due to the energy scale is shown as a shaded band.

8.1 Cross sections for $134 < W_{\gamma p} < 277$ GeV

The dijet cross section as a function of the transverse energy of the leading jet is presented for six different ranges in jet pseudorapidity. These cross sections have been determined both for the full x_γ^{obs} range and for $x_\gamma^{obs} > 0.75$. Numerical values for the cross sections and the uncertainties are given in tables 8.1 and 8.2. The results are plotted in figure 8.1 and 8.2. The dijet cross section falls rapidly with increasing transverse energy of the leading jet. The steepest slopes occur when both jets are in the most backward pseudorapidity bin, $-1 < \eta_{1,2}^{jet} < 0$. High x_γ^{obs} events dominate the cross section at backward angles of the jets and at high transverse energies of the jets. This behaviour is expected on kinematic grounds, since high x_γ^{obs} values give access to the highest transverse jet energies and to the most backward pseudorapidities.

The data are compared to NLO QCD calculations (see chapter 3). Since the calculations from different groups are very similar [47], as will be shown in figure 8.3 and 8.4, only one set of calculations is shown here. These calculations use the GRV-HO [22, 23] parametrisation for the parton densities in the photon, which, in comparison to other parametrisations, corresponds to the highest cross section. In general, the slopes and the absolute cross section are well described by the NLO QCD calculations. However, for events with forward jets, $1 < \eta_{1,2}^{jet} < 2$, and $E_{T\,leading}^{jet} < 25$ GeV the data lie above the predictions and for events with very backward jets, $-1 < \eta_{1,2}^{jet} < 0$, the measurement lies below the calculations. The Monte Carlo studies, discussed in chapter 3, show that fragmentation effects decrease the measured cross section in the latter pseudorapidity region. It is therefore to be expected that the NLO QCD calculations, in which no parton-to-hadron fragmentation is included, predict a higher cross section than that observed in this region.

The dijet cross section is also presented as a function of the pseudorapidity of one of the

jets while confining the other jet to specific pseudorapidity ranges. Numerical values for the cross section and the uncertainties are given in tables 8.3 and 8.4 and are plotted in figure 8.3. The cross section peaks for events with η_2^{jet} near 1 and falls rapidly for events with $\eta_2^{jet} < 0$.

The measurements are again compared to NLO QCD calculations, but now using three different parametrisations for the parton densities in the photon. For the full x_γ^{obs} range, at central and forward pseudorapidities of the jets, the data lie above all predictions. At backward pseudorapidities, as for the cross section as a function of $E_{T\,leading}^{jet}$, the data lie below the calculations. In the high x_γ^{obs} region general agreement is observed between the data and the predictions.

Figure 8.3d shows a comparison between the NLO QCD results from four different groups for the range $0 < \eta_1^{jet} < 1$. Each calculation uses the same parton density distributions for the proton, CTEQ4M [42], and the photon, GRV-HO [22, 23]. The calculations from Aurenche et al., Frixione et al., Harris et al. and Klasen et al. agree to within a few percent (see also [47]).

In conclusion: it has been shown that NLO QCD calculations generally describe the measured cross sections. However, for backward pseudorapidities the data are below the calculations, which is expected to be due to fragmentation effects, while for forward and central pseudorapidities the data are above the NLO predictions. In the latter kinematic region theoretical uncertainties are expected to be small. This observation will be discussed in more detail in section 8.3.

8.2 Cross sections for $212 < W_{\gamma p} < 277$ GeV

The pseudorapidity dependence of the cross section has also been determined for events in a narrower region in y, which corresponds to a narrower range in $W_{\gamma p}$, the photon-proton CM energy. In such a region the sensitivity to the photon structure is expected to be larger. This follows from the relation between y, x_γ^{obs} and the pseudorapidities of the jets (see formula 3.5). Using a narrower range of y values implies that the cross section for specific pseudorapidities of the jets corresponds to a narrower range of x_γ^{obs} values. It is natural to select a narrow region of high y values rather than a narrow region of low y values, since in the latter case, events with low x_γ^{obs} would fall out of the range of jet pseudorapidities, $-1 < \eta^{jet} < 2$.

Using a range of $0.50 < y < 0.85$, the cross section is presented as a function of the pseudorapidity of one of the jets while confining the other jet to specific pseudorapidity ranges. Values for the cross section and the uncertainties are given in tables 8.5 and 8.6 and are shown in figure 8.4. The cross section for this high y region peaks at more backward pseudorapidities than the cross section for the full y range, as observed in a previous ZEUS study [54], and also the peak is more pronounced than for the full y range. This observation is consistent with the expected closer correlation between η^{jets} and x_γ^{obs} when the y range is constricted. The peak in the cross sections at backward pseudorapidities reflects the peak near $x_\gamma^{obs} \approx 1$ in figure 6.11 and the tail towards positive pseudorapidities corresponds to low x_γ^{obs} values.

The measurements are again compared to NLO QCD calculations using the GRV-HO, AFG-HO and GS96-HO parametrisations of the photon structure. The NLO predictions show an enhanced sensitivity to the choice of parametrisation for the photon structure. In particular in the region $1 < \eta_1^{jet} < 2$ there are clear differences in shape between the NLO predictions

corresponding to different parton densities in the photon. In the most backward bins, where $\eta_2^{jet} < -0.5$ or where $\eta_{1,2}^{jet} < 0$, the data again lie below the calculations, but, as stated above, fragmentation effects are large in this region. At central and forward pseudorapidities, both for the full and for the high x_γ^{obs} range, the data lie above the NLO calculations.

In figure 8.4d a comparison is again made between the NLO QCD results from different groups. The calculations agree to within a few percent (see also [47]).

The fact that the cross sections, measured in the region where jets are produced at central and forward pseudorapidities and where theoretical uncertainties are expected to be small, lie above the NLO QCD predictions, suggests that in this kinematic region the parton densities in the photon are too small in the available parametrisations. The disagreement between the data and the calculations is observed for the full x_γ^{obs} range and to a lesser extent also for $x_\gamma^{obs} > 0.75$. It is strongest at central pseudorapidities. This region corresponds to values of x_γ that lie roughly between 0.5 and 1.

8.3 Conclusions

A measurement of dijet photoproduction, in the range $0.20 < y < 0.85$, $Q^2 < 1$ GeV^2, $-1 < \eta^{jet} < 2$, $E_{T\,leading}^{jet} > 14$ GeV and $E_{T\,second}^{jet} > 11$ GeV, has been presented. Jets are defined in the hadronic final state by applying the k_T-clustering jet algorithm. The cross section has been compared to NLO QCD predictions.

For the full y region, $0.20 < y < 0.85$, corresponding to $134 < W_{\gamma p} < 277$ GeV, the dijet cross section has been measured as a function of the transverse energy of the leading jet and as a function of the pseudorapidities of the jets. The dependence on the transverse energy of the leading jet is generally well described by the NLO QCD calculations, although for events with two forward going jets and $E_{T\,leading}^{jet} < 25$ GeV the data lie above the NLO QCD calculations. Also, the cross section as a function of the pseudorapidities of the jets lies above the NLO QCD calculations at central and forward pseudorapidities. In the region of $x_\gamma^{obs} > 0.75$, the cross section agrees with the calculations.

In the high y region, $0.50 < y < 0.85$ ($212 < W_{\gamma p} < 277$ GeV), where a stronger sensitivity to the photon structure is expected, the cross section at central and forward pseudorapidities lies even higher above the predictions than for the full y range.

Since theoretical uncertainties are expected to be small in most of the kinematic regime of the present analysis, as was discussed in the chapters 3 and 6.3, the discrepancies observed between the data and the NLO QCD calculations suggest that, in the kinematic region of the present analysis, the available parametrisations of the parton densities in the photon are too small.

The results presented in this thesis cover a kinematic region where both x_γ^{obs} and E_T^{jet}, which acts as the factorisation scale, are high. This region has not been studied in F_2^γ measurements at e^+e^- colliders. It remains to be established whether the parton density functions in the photon can be modified to describe the present data while remaining consistent with the existing F_2^γ data from e^+e^- experiments. Inclusion of the data presented in this thesis in NLO QCD fits, used to determine parton density functions in the photon, will clarify this issue.

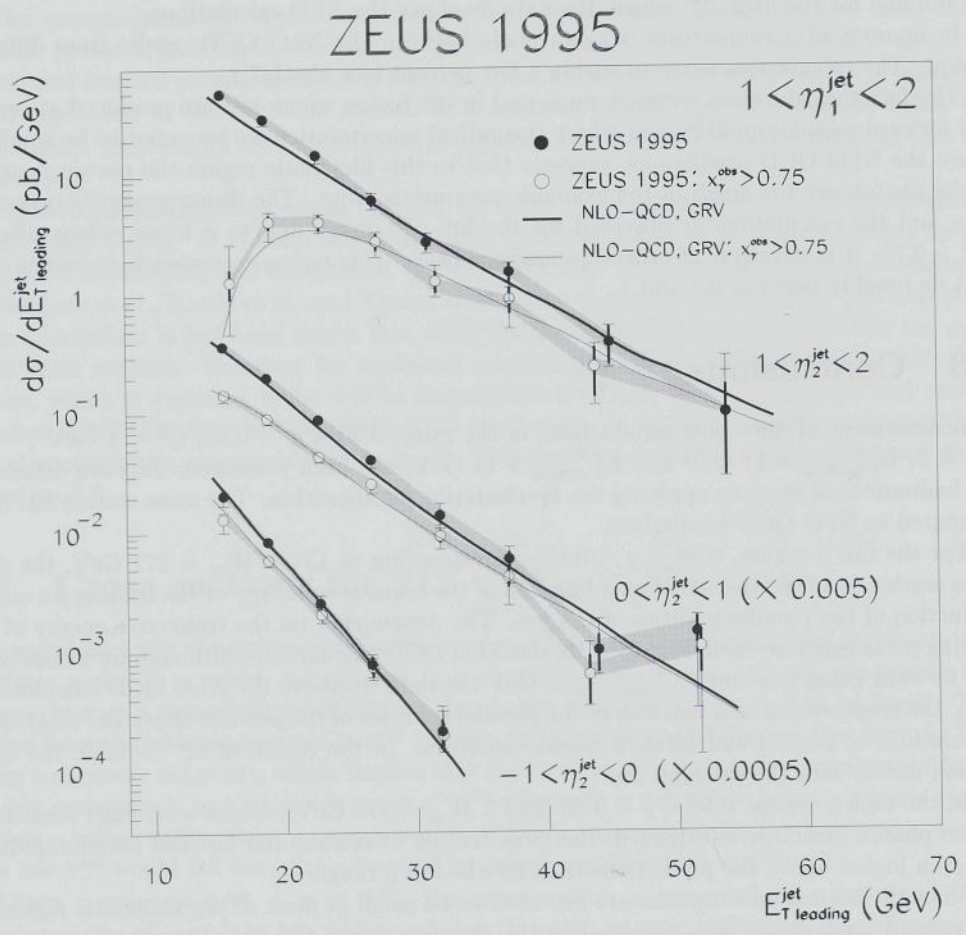

Figure 8.1: Dijet cross section as a function of $E_{T\,leading}^{jet}$ for η_1^{jet} between 1 and 2, in three regions of η_2^{jet}. For convenience of comparison the results for $-1 < \eta_2^{jet} < 0$ and $0 < \eta_2^{jet} < 1$ have been scaled by the factors indicated in the figure. The filled circles correspond to the entire x_γ^{obs} range while the open circles correspond to events with $x_\gamma^{obs} > 0.75$. The shaded band indicates the uncertainty related to the energy scale. The thick error bar indicates the statistical uncertainty and the thin error bar indicates the systematic and statistical uncertainties added in quadrature. The data are compared to NLO QCD calculations, using the GRV-HO parametrisation for the photon structure.

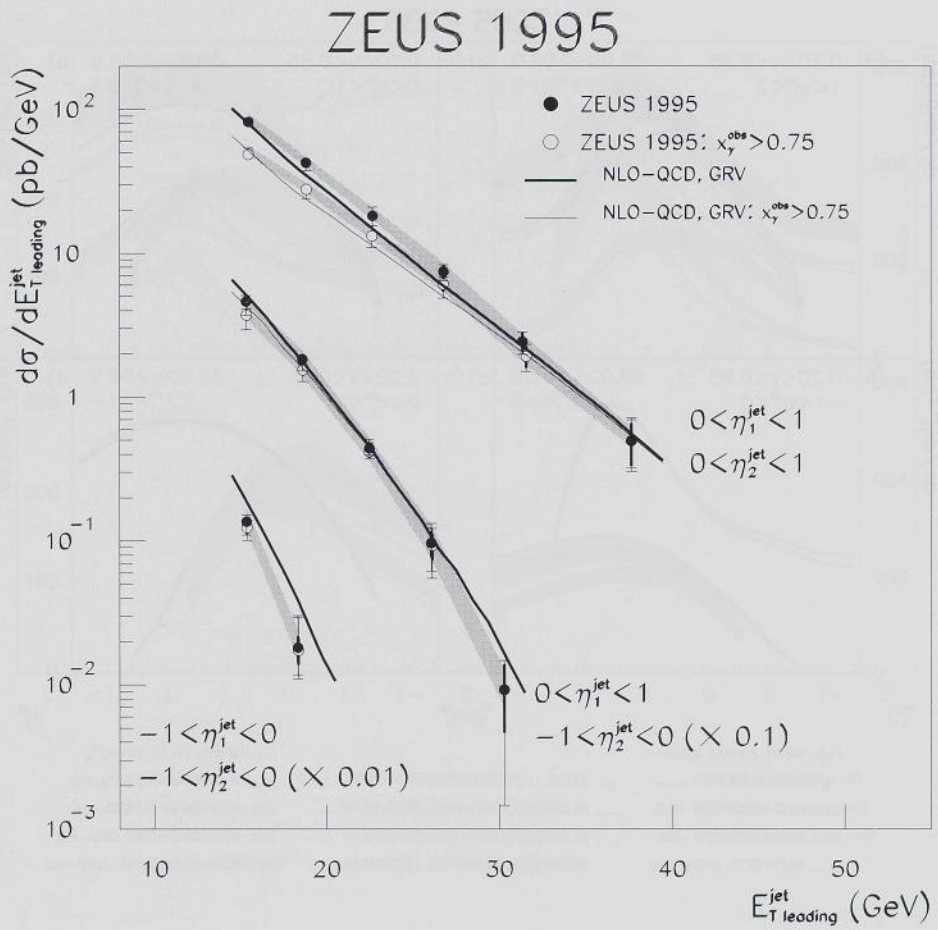

Figure 8.2: Dijet cross section as a function of $E_{T\,leading}^{jet}$. For the two upper sets of data η_1^{jet} lies between 0 and 1 and for the lower set of data η_1^{jet} lies between -1 and 0. The η_2^{jet} regions are indicated the figure. For convenience of comparison the two lower sets of data are scaled by the factors indicated in the figure. The filled circles correspond to the entire x_γ^{obs} range while the open circles correspond to events with $x_\gamma^{obs} > 0.75$. The shaded band indicates the uncertainty related to the energy scale. The thick error bar indicates the statistical uncertainty and the thin error bar indicates the systematic and statistical uncertainties added in quadrature. The data are compared to NLO QCD calculations, using the GRV-HO parametrisation for the photon structure.

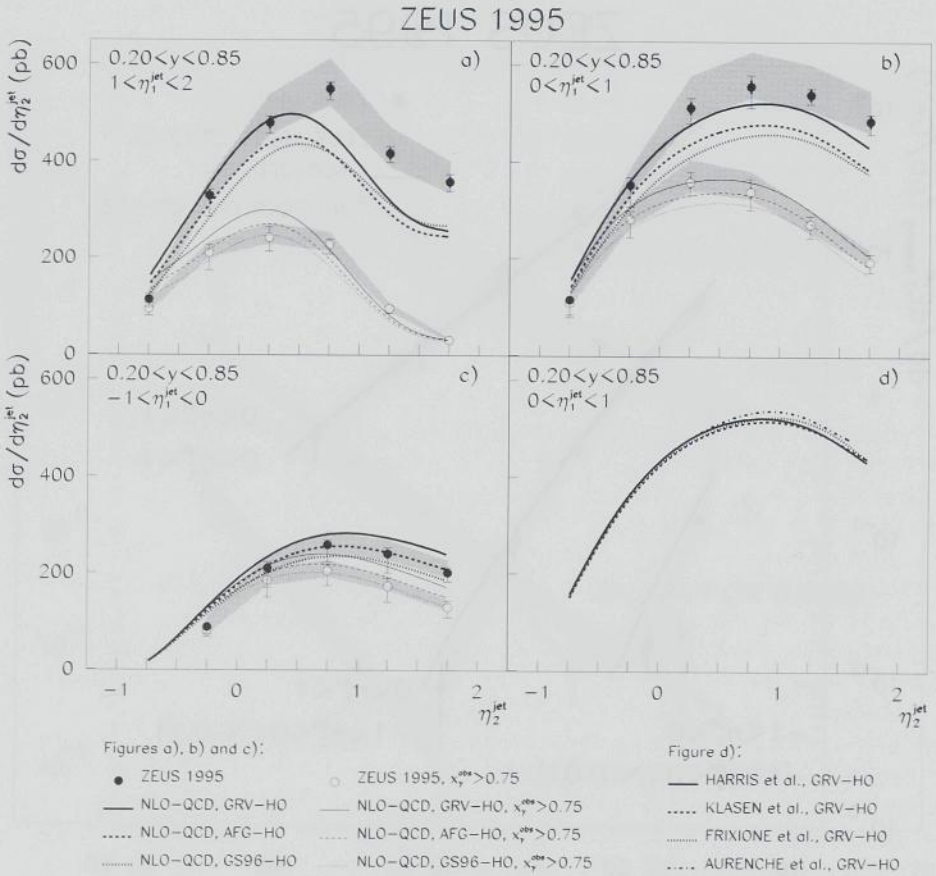

Figure 8.3: Figures a), b) and c) show the dijet cross section as a function of η_2^{jet} in bins of η_1^{jet}. The filled circles correspond to the entire x_γ^{obs} range while the open circles correspond to events with $x_\gamma^{obs} > 0.75$. The shaded band indicates the uncertainty related to the energy scale. The thick error bar indicates the statistical uncertainty and the thin error bar indicates the systematic and statistical uncertainties added in quadrature. The full, dotted and dashed curves correspond to NLO QCD calculations, using the GRV-HO, GS96-HO and the AFG-HO parametrisations for the photon structure, respectively. In d) the NLO QCD results for the cross section when $0 < \eta_1^{jet} < 1$ and for a particular parametrisation of the photon structure are compared.

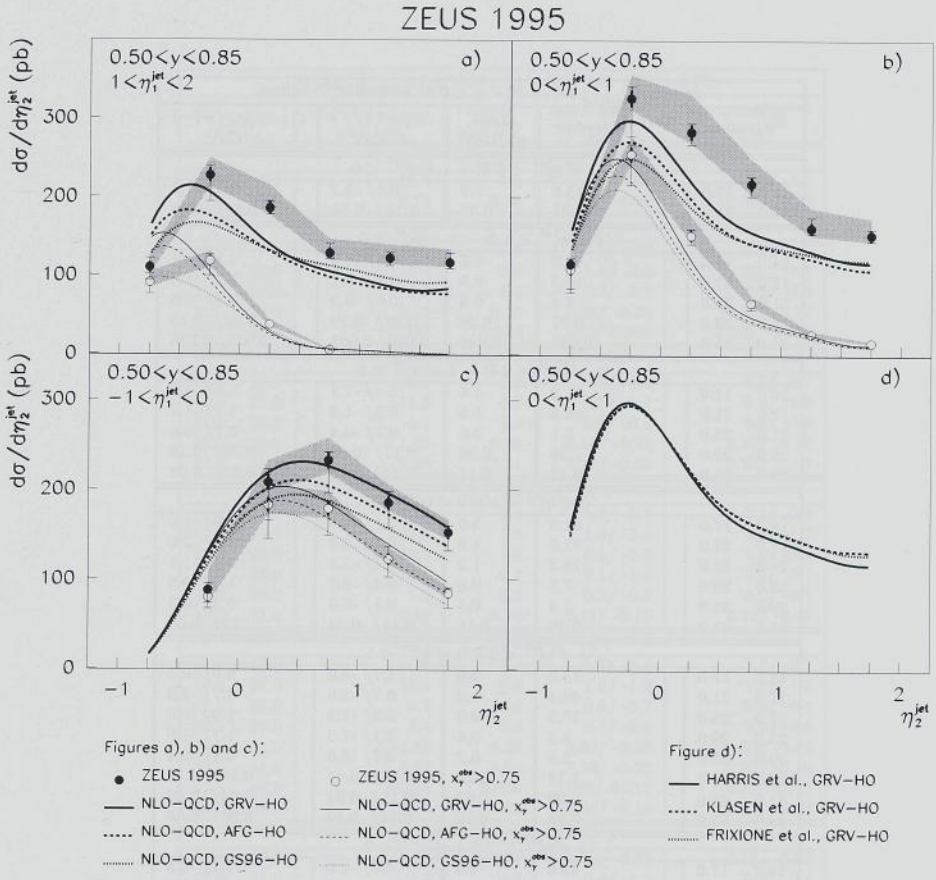

Figure 8.4: Figures a), b) and c) show the dijet cross section as a function of η_2^{jet} in bins of η_1^{jet} and for $0.50 < y < 0.85$. The filled circles correspond to the entire x_γ^{obs} range while the open circles correspond to events with $x_\gamma^{obs} > 0.75$. The shaded band indicates the uncertainty related to the energy scale. The thick error bar indicates the statistical uncertainty and the thin error bar indicates the systematic and statistical uncertainties added in quadrature. The full, dotted and dashed curves correspond to NLO QCD calculations, using the GRV-HO, GS96-HO and the AFG-HO parametrisations for the photon structure, respectively. In d) the NLO QCD results for the cross section when $0 < \eta_1^{jet} < 1$ and for a particular parametrisation of the photon structure are compared.

$d\sigma/dE^{jet}_{T\,leading}$ for: $0.20 < y < 0.85$ and all x_γ^{obs} values				
$E^{jet}_{T\,leading}$ GeV	$d\sigma/dE^{jet}_{T\,leading}$ pb/GeV	Δ_{stat} pb/GeV	Δ_{syst} (+/−) pb/GeV	$\Delta_{E-scale}$ (+/−) pb/GeV
$-1 < \eta_1^{jet} < 0$ & $-1 < \eta_2^{jet} < 0$				
14.0 .. 17.0	13.6	1.2	0.9/ -2.2	3.2/ -1.2
17.0 .. 21.0	1.81	0.37	1.16/ -0.54	0.60/ -0.26
$0 < \eta_1^{jet} < 1$ & $-1 < \eta_2^{jet} < 0$				
14.0 .. 17.0	46.2	1.7	4.4/ -8.9	4.1/ -2.1
17.0 .. 21.0	18.3	0.9	0.7/ -3.1	2.7/ -1.5
21.0 .. 25.0	4.4	0.4	0.6/ -0.2	0.8/ -0.5
25.0 .. 29.0	0.97	0.20	0.29/ -0.29	0.32/ -0.15
29.0 .. 35.0	0.093	0.046	0.030/-0.063	0.035/-0.023
$1 < \eta_1^{jet} < 2$ & $-1 < \eta_2^{jet} < 0$				
14.0 .. 17.0	41.2	1.6	2.4/ -7.1	5.8/ -1.0
17.0 .. 21.0	16.9	0.8	0.5/ -1.4	1.2/ -1.2
21.0 .. 25.0	5.1	0.5	0.7/ -0.4	0.7/ -0.6
25.0 .. 29.0	1.56	0.26	0.17/ -0.23	0.29/ -0.19
29.0 .. 35.0	0.42	0.11	0.24/ -0.05	0.10/ -0.08
$0 < \eta_1^{jet} < 1$ & $0 < \eta_2^{jet} < 1$				
14.0 .. 17.0	81.8	3.0	3.1/ -1.8	11.9/ -1.6
17.0 .. 21.0	42.5	1.9	0.5/ -4.8	4.1/ -2.6
21.0 .. 25.0	18.2	1.2	2.4/ -2.5	2.6/ -1.1
25.0 .. 29.0	7.5	0.8	0.3/ -0.7	1.1/ -0.8
29.0 .. 35.0	2.4	0.4	0.1/ -0.3	0.3/ -0.3
35.0 .. 41.0	0.49	0.16	0.14/ -0.04	0.12/ -0.05
$1 < \eta_1^{jet} < 2$ & $0 < \eta_2^{jet} < 1$				
14.0 .. 17.0	73.7	2.0	1.7/ -3.0	9.0/ -0.5
17.0 .. 21.0	40.4	1.3	0.7/ -2.6	4.7/ -2.9
21.0 .. 25.0	17.9	0.9	0.2/ -1.3	1.9/ -1.6
25.0 .. 29.0	8.2	0.6	0.1/ -1.0	1.1/ -1.0
29.0 .. 35.0	2.8	0.3	0.7/ -0.6	0.4/ -0.4
35.0 .. 41.0	1.18	0.18	0.25/ -0.41	0.13/ -0.14
41.0 .. 48.0	0.20	0.07	0.15/ -0.03	0.04/ -0.02
48.0 .. 55.0	0.28	0.10	0.04/ -0.19	0.06/ -0.05
$1 < \eta_1^{jet} < 2$ & $1 < \eta_2^{jet} < 2$				
14.0 .. 17.0	49.6	2.3	4.0/ -2.0	7.1/ -0.8
17.0 .. 21.0	30.4	1.6	1.0/ -2.9	3.4/ -2.7
21.0 .. 25.0	15.0	1.1	0.5/ -1.9	1.6/ -1.5
25.0 .. 29.0	6.2	0.7	0.7/ -0.7	0.8/ -0.6
29.0 .. 35.0	2.8	0.4	0.3/ -0.3	0.3/ -0.4
35.0 .. 41.0	1.53	0.29	0.05/ -0.60	0.25/ -0.12
41.0 .. 48.0	0.39	0.14	0.05/ -0.06	0.06/ -0.07
48.0 .. 55.0	0.099	0.070	0.183/-0.009	0.009/-0.007

Table 8.1: The dijet cross section for the full x_γ^{obs} range and $0.20 < y < 0.85$, as a function of $E^{jet}_{T\,leading}$ in bins of the jet pseudorapidities.

$d\sigma/dE^{jet}_{T\,leading}$ for: $0.20 < y < 0.85$ and $x_\gamma^{obs} > 0.75$				
$E^{jet}_{T\,leading}$ GeV	$d\sigma/dE^{jet}_{T\,leading}$ pb/GeV	Δ_{stat} pb/GeV	Δ_{syst} (+/−) pb/GeV	$\Delta_{E-scale}$ (+/−) pb/GeV
$-1 < \eta_1^{jet} < 0$ & $-1 < \eta_2^{jet} < 0$				
14.0 .. 17.0	12.4	1.2	1.0/ -2.0	2.9/ -1.1
17.0 .. 21.0	1.74	0.36	1.12/ -0.52	0.58/ -0.25
$0 < \eta_1^{jet} < 1$ & $-1 < \eta_2^{jet} < 0$				
14.0 .. 17.0	37.1	1.5	3.5/ -7.7	3.3/ -1.7
17.0 .. 21.0	15.4	0.8	1.1/ -2.5	2.3/ -1.3
21.0 .. 25.0	4.2	0.4	0.5/ -0.2	0.8/ -0.5
25.0 .. 29.0	0.93	0.19	0.22/ -0.32	0.30/ -0.14
29.0 .. 35.0	0.093	0.046	0.030/-0.063	0.035/-0.023
$1 < \eta_1^{jet} < 2$ & $-1 < \eta_2^{jet} < 0$				
14.0 .. 17.0	26.2	1.2	3.2/ -5.9	3.7/ -0.7
17.0 .. 21.0	11.8	0.7	0.7/ -1.1	0.9/ -0.9
21.0 .. 25.0	4.1	0.4	0.6/ -0.5	0.6/ -0.5
25.0 .. 29.0	1.48	0.25	0.13/ -0.22	0.27/ -0.18
29.0 .. 35.0	0.39	0.11	0.20/ -0.02	0.10/ -0.07
$0 < \eta_1^{jet} < 1$ & $0 < \eta_2^{jet} < 1$				
14.0 .. 17.0	48.6	2.3	4.4/ -2.1	7.1/ -0.9
17.0 .. 21.0	27.8	1.5	1.6/ -3.5	2.7/ -1.7
21.0 .. 25.0	13.2	1.0	2.1/ -2.0	1.9/ -0.8
25.0 .. 29.0	6.1	0.7	0.1/ -1.0	0.9/ -0.7
29.0 .. 35.0	1.9	0.3	0.2/ -0.3	0.2/ -0.3
35.0 .. 41.0	0.49	0.16	0.11/ -0.10	0.12/ -0.05
$1 < \eta_1^{jet} < 2$ & $0 < \eta_2^{jet} < 1$				
14.0 .. 17.0	29.0	1.3	1.1/ -3.4	3.6/ -0.2
17.0 .. 21.0	18.4	0.9	1.6/ -1.9	2.1/ -1.3
21.0 .. 25.0	8.7	0.6	0.6/ -0.7	0.9/ -0.8
25.0 .. 29.0	5.1	0.4	0.1/ -0.8	0.7/ -0.6
29.0 .. 35.0	1.85	0.23	0.39/ -0.35	0.30/ -0.26
35.0 .. 41.0	0.83	0.15	0.30/ -0.32	0.09/ -0.10
41.0 .. 48.0	0.125	0.056	0.092/-0.012	0.023/-0.012
48.0 .. 55.0	0.21	0.09	0.06/ -0.16	0.05/ -0.04
$1 < \eta_1^{jet} < 2$ & $1 < \eta_2^{jet} < 2$				
14.0 .. 17.0	1.28	0.37	1.32/ -0.73	0.18/ -0.02
17.0 .. 21.0	4.2	0.6	0.6/ -1.2	0.5/ -0.4
21.0 .. 25.0	4.1	0.6	0.3/ -0.5	0.4/ -0.4
25.0 .. 29.0	2.8	0.5	0.3/ -0.5	0.4/ -0.3
29.0 .. 35.0	1.29	0.28	0.38/ -0.21	0.16/ -0.16
35.0 .. 41.0	0.91	0.23	0.05/ -0.32	0.15/ -0.07
41.0 .. 48.0	0.24	0.11	0.07/ -0.06	0.04/ -0.04
48.0 .. 55.0	0.099	0.070	0.096/-0.009	0.009/-0.007

Table 8.2: The dijet cross section for $x_\gamma^{obs} > 0.75$ and $0.20 < y < 0.85$, as a function of $E^{jet}_{T\,leading}$ in bins of the jet pseudorapidities.

$d\sigma/d\eta^{jet}$ for: $0.20 < y < 0.85$ and all x_γ^{obs} values				
η_2^{jet}	$d\sigma/d\eta_2^{jet}$ pb	Δ_{stat} pb	Δ_{syst} (+/−) pb	$\Delta_{E-scale}$ (+/−) pb
$-1 < \eta_1^{jet} < 0$				
-0.5 .. 0.0	88	5	6/ -13	20/ -9
0.0 .. 0.5	209	9	10/ -39	26/ -13
0.5 .. 1.0	258	9	4/ -34	28/ -17
1.0 .. 1.5	240	9	9/ -39	28/ -12
1.5 .. 2.0	201	8	7/ -17	25/ -10
$0 < \eta_1^{jet} < 1$				
-1.0 .. -0.5	115	7	4/ -30	21/ -12
-0.5 .. 0.0	353	11	11/ -44	35/ -19
0.0 .. 0.5	513	13	16/ -29	66/ -25
0.5 .. 1.0	558	14	19/ -43	71/ -23
1.0 .. 1.5	541	13	1/ -15	61/ -32
1.5 .. 2.0	486	13	6/ -23	63/ -25
$1 < \eta_1^{jet} < 2$				
-1.0 .. -0.5	113	6	10/ -15	18/ -8
-0.5 .. 0.0	328	11	7/ -42	36/ -15
0.0 .. 0.5	479	12	4/ -19	60/ -25
0.5 .. 1.0	549	14	1/ -18	63/ -33
1.0 .. 1.5	416	12	9/ -14	54/ -28
1.5 .. 2.0	358	11	12/ -15	43/ -23

Table 8.3: The dijet cross section, for all x_γ^{obs} values and $0.20 < y < 0.85$, as a function of η_2^{jet}, for η_1^{jet} fixed.

$d\sigma/d\eta^{jet}$ for: $0.20 < y < 0.85$ and $x_\gamma^{obs} > 0.75$				
η_2^{jet}	$d\sigma/d\eta_2^{jet}$ pb	Δ_{stat} pb	Δ_{syst} (+/−) pb	$\Delta_{E-scale}$ (+/−) pb
$-1 < \eta_1^{jet} < 0$				
-0.5 .. 0.0	80	5	8/ -12	18/ -8
0.0 .. 0.5	185	8	13/ -35	23/ -11
0.5 .. 1.0	204	8	9/ -30	23/ -13
1.0 .. 1.5	173	8	15/ -32	20/ -9
1.5 .. 2.0	129	7	12/ -19	16/ -7
$0 < \eta_1^{jet} < 1$				
-1.0 .. -0.5	109	7	3/ -29	20/ -11
-0.5 .. 0.0	283	10	14/ -37	28/ -15
0.0 .. 0.5	359	11	19/ -25	46/ -18
0.5 .. 1.0	339	11	26/ -35	43/ -14
1.0 .. 1.5	273	9	15/ -27	31/ -16
1.5 .. 2.0	195	8	14/ -20	25/ -10
$1 < \eta_1^{jet} < 2$				
-1.0 .. -0.5	94	6	11/ -13	15/ -7
-0.5 .. 0.0	210	8	14/ -35	23/ -9
0.0 .. 0.5	241	9	20/ -27	30/ -12
0.5 .. 1.0	227	9	7/ -18	26/ -14
1.0 .. 1.5	95	6	6/ -8	12/ -6
1.5 .. 2.0	30	3	2/ -2	4/ -2

Table 8.4: The dijet cross section for $x_\gamma^{obs} > 0.75$ and $0.20 < y < 0.85$, as a function of η_2^{jet}, for η_1^{jet} fixed.

$d\sigma/d\eta^{jet}$ for: $0.50 < y < 0.85$ and all x_γ^{obs} values				
η_2^{jet}	$d\sigma/d\eta_2^{jet}$ pb	Δ_{stat} pb	Δ_{syst} (+/−) pb	$\Delta_{E-scale}$ (+/−) pb
$-1 < \eta_1^{jet} < 0$				
-0.5 .. 0.0	88	5	6/ -13	20/ -9
0.0 .. 0.5	208	9	12/ -41	25/ -11
0.5 .. 1.0	232	9	2/ -35	25/ -14
1.0 .. 1.5	185	8	11/ -26	20/ -8
1.5 .. 2.0	152	7	2/ -19	14/ -8
$0 < \eta_1^{jet} < 1$				
-1.0 .. -0.5	115	7	4/ -30	21/ -12
-0.5 .. 0.0	326	11	11/ -47	29/ -15
0.0 .. 0.5	284	10	6/ -13	48/ -14
0.5 .. 1.0	218	9	3/ -13	32/ -13
1.0 .. 1.5	162	7	12/ -2	26/ -10
1.5 .. 2.0	153	7	3/ -3	21/ -8
$1 < \eta_1^{jet} < 2$				
-1.0 .. -0.5	110	6	10/ -15	16/ -8
-0.5 .. 0.0	227	9	8/ -32	22/ -14
0.0 .. 0.5	186	8	4/ -4	29/ -9
0.5 .. 1.0	128	6	11/ -3	18/ -8
1.0 .. 1.5	122	6	4/ -7	17/ -8
1.5 .. 2.0	117	6	11/ -5	17/ -5

Table 8.5: The dijet cross section, for all x_γ^{obs} values and $0.50 < y < 0.85$, as a function of η_2^{jet}, for η_1^{jet} fixed.

$d\sigma/d\eta^{jet}$ for: $0.50 < y < 0.85$ and $x_\gamma^{obs} > 0.75$				
η_2^{jet}	$d\sigma/d\eta_2^{jet}$ pb	Δ_{stat} pb	Δ_{syst} (+/−) pb	$\Delta_{E-scale}$ (+/−) pb
$-1 < \eta_1^{jet} < 0$				
-0.5 .. 0.0	80	5	8/ -12	18/ -8
0.0 .. 0.5	183	8	15/ -37	22/ -10
0.5 .. 1.0	178	8	4/ -29	19/ -11
1.0 .. 1.5	122	6	13/ -18	13/ -5
1.5 .. 2.0	84	5	3/ -15	8/ -4
$0 < \eta_1^{jet} < 1$				
-1.0 .. -0.5	108	7	4/ -29	20/ -11
-0.5 .. 0.0	255	9	9/ -38	23/ -12
0.0 .. 0.5	152	7	5/ -9	26/ -8
0.5 .. 1.0	66	5	0/ -7	10/ -4
1.0 .. 1.5	27	3	2/ -1	4/ -2
1.5 .. 2.0	15	2	2/ -1	2/ -1
$1 < \eta_1^{jet} < 2$				
-1.0 .. -0.5	91	6	10/ -13	13/ -6
-0.5 .. 0.0	118	6	5/ -18	12/ -7
0.0 .. 0.5	37	3	0/ -4	6/ -2
0.5 .. 1.0	5.0	1.2	2.5/ -0.5	0.7/ -0.3

Table 8.6: The dijet cross section for $x_\gamma^{obs} > 0.75$ and $0.50 < y < 0.85$, as a function of η_2^{jet}, for η_1^{jet} fixed.

Chapter 9

Outlook on future analyses

In this section preliminary results are presented of a first analysis of the data collected with the ZEUS detector in 1996 and 1997. A more detailed analysis is being performed in parallel to the writing of this thesis. These data correspond to a luminosity of 37.9 pb^{-1}, which is more than six times the data collected in 1995. With such a large gain in statistics the measurement of dijet photoproduction can be extended to higher transverse energies of the jets and the errors in the already measured regions will be reduced significantly. This means the confrontation of the theory with these data becomes more challenging due to the reduced experimental uncertainties and because at higher transverse energies theoretical uncertainties are expected to be reduced.

9.1 The 1996 and 1997 analysis

The analysis of the 1996 and 1997 data is to a large extent identical to the 1995 analysis. The main differences are the following:

- some modifications were made to the detector in the shutdown period between 1995 and 1996, the most important of which was the removal of the vertex detector (VXD) which reduced the amount of material near the interaction point,
- modifications were made to the online trigger selection of dijet photoproduction candidate events. In particular on the TLT it was required that: at least two jets were found with $\eta^{jet} < 1.5$ and $E_T^{jet} > 4$ GeV or at least two jets with $\eta^{jet} < 2.5$ and $E_T^{jet} > 6$ GeV. Like the TLT requirement applied in 1995 this requirement is highly efficient.
- because of the modifications to the detector and the trigger it was necessary to produce new samples of Monte Carlo events corresponding to the years 1996 and 1997,
- the determination of energy correction functions for ZUFOs from a kinematically constrained fit, as discussed in section 5.2, was repeated using 1996 and 1997 NC-DIS data and Monte Carlo samples.

Between 1996 and 1997 no changes were made to the detector and to the trigger selection, which makes the combination of data from 1996 and 1997 in one single analysis relatively straightforward.

The same offline selection procedure, as described in chapter 6, is applied.

After all selection cuts 49312 events remain. Figure 9.1 shows various kinematic distributions for these events. The distributions are compared to the HERWIG 5.9 Monte Carlo. Good agreement is found between data and Monte Carlo, as was the case for the 1995 data (see chapter 6.3). With the gain in statistics the study of jets with transverse energies up to 80 GeV is accessible.

In figure 9.2 the highest transverse energy dijet event observed in the ZEUS detector until the end of 1997 is shown. The event is a direct photoproduction event with: $E_{T\,leading}^{jet} = 81.3$ GeV, $E_{T\,second}^{jet} = 70.8$ GeV, $x_{\gamma}^{obs} = 0.98$ and $y_{JB} = 0.53$.

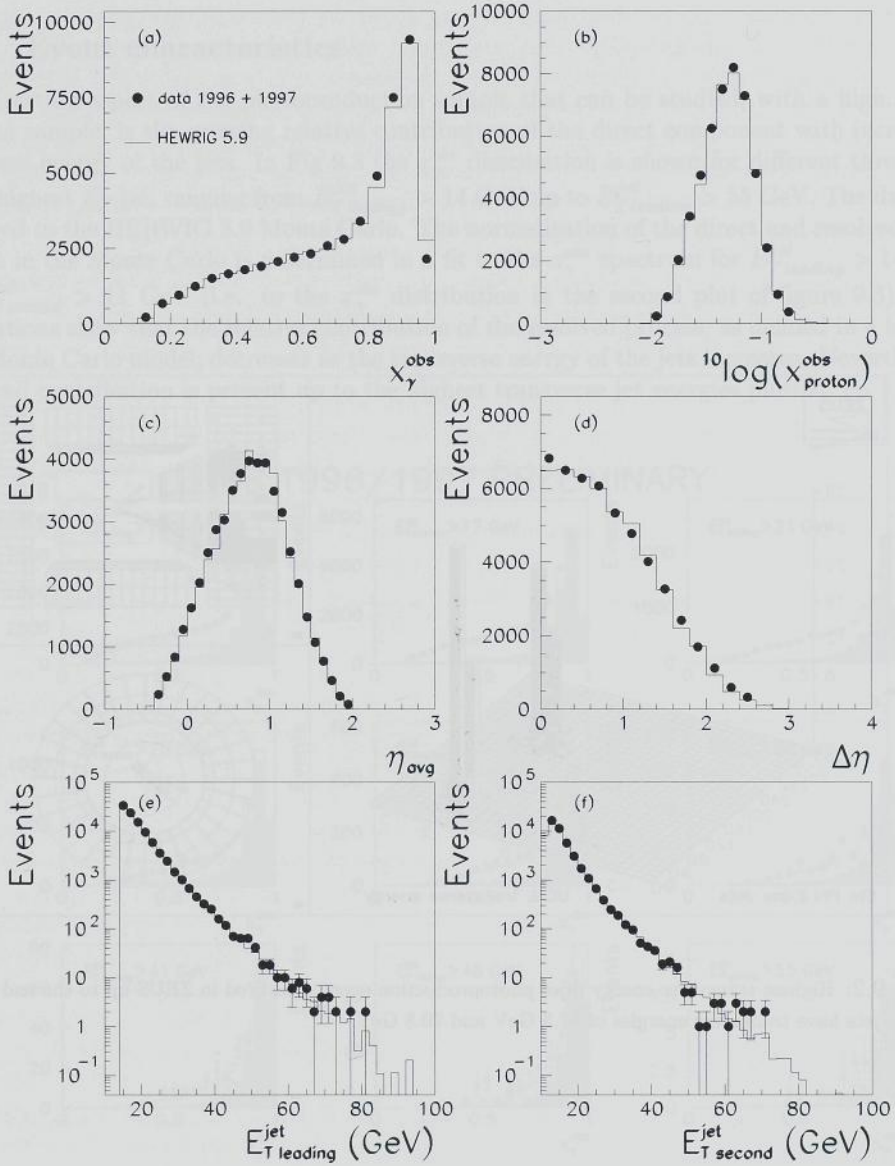

Figure 9.1: Detector level distributions of x_γ^{obs} (a), x_{proton}^{obs} (b), the average pseudorapidity (c), the absolute pseudorapidity difference between the jets (d) and the transverse energy of the highest (e) and second highest (f) E_T jet. The data are compared to HERWIG 5.9 (histogram). The data are shown with statistical errors only.

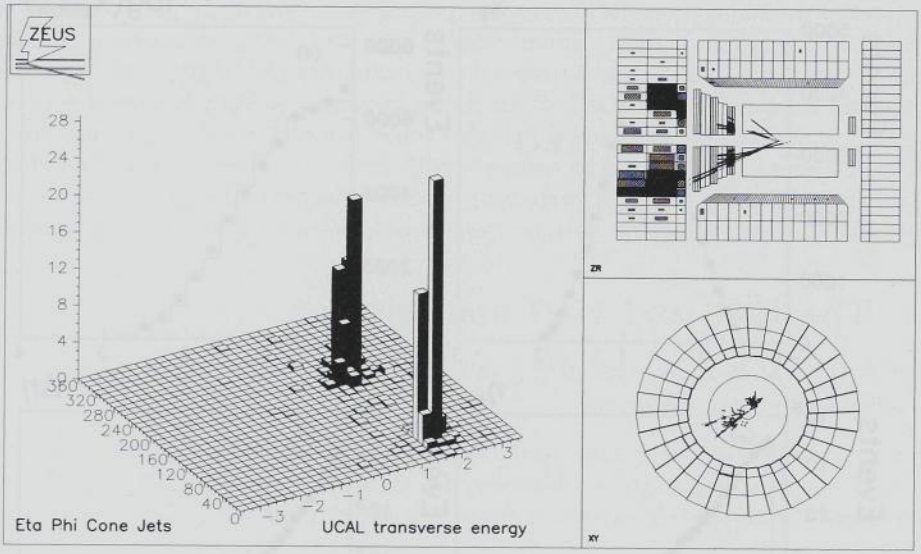

Figure 9.2: Highest transverse energy dijet photoproduction event measured in ZEUS up to the end of 1997. The two jets have transverse energies of 81.3 GeV and 70.8 GeV.

9.2 Preliminary results of the 1996 and 1997 data

9.2.1 Event characteristics

An interesting aspect of the photoproduction sample that can be studied, with a high statistics data sample, is the growing relative contribution of the direct component with increasing transverse energy of the jets. In Fig 9.3 the x_γ^{obs} distribution is shown for different thresholds on the highest E_T jet, ranging from $E_{T\,leading}^{jet} > 14$ GeV up to $E_{T\,leading}^{jet} > 55$ GeV. The data are compared to the HERWIG 5.9 Monte Carlo. The normalisation of the direct and resolved components in the Monte Carlo is determined in a fit to the x_γ^{obs} spectrum for $E_{T\,leading}^{jet} > 14$ GeV and $E_{T\,second}^{jet} > 11$ GeV (i.e. to the x_γ^{obs} distribution in the second plot of figure 9.3). The distributions show that the relative contribution of the resolved process, as defined in a leading order Monte Carlo model, decreases as the transverse energy of the jets increases. Nevertheless, a resolved contribution is present up to the highest transverse jet energies plotted.

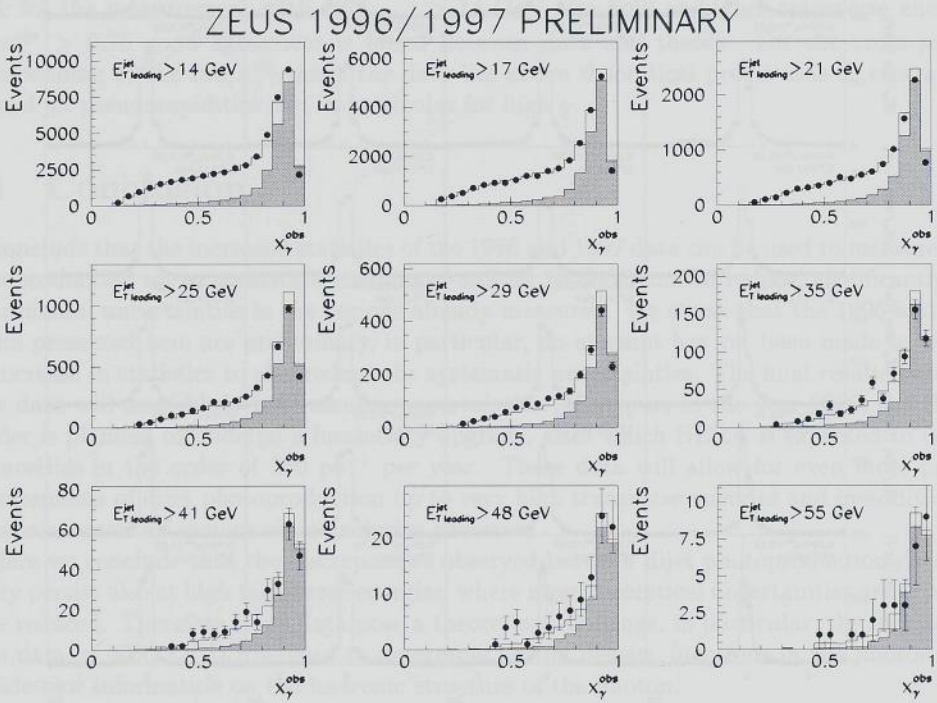

Figure 9.3: Distributions of x_γ^{obs} for different thresholds on the highest transverse energy jet. The second jet is always required to have $E_{T\,second}^{jet} > 11$ GeV. The dots are the combined 1996 and 1997 data, the open histogram is the prediction of the HERWIG 5.9 Monte Carlo and the shaded histogram is the direct component of this Monte Carlo. The data are shown with statistical errors only.

It is also interesting to study the transverse energy flow around jets, as a function of the transverse jet energy. These distributions were shown in section 6.3 for jets with transverse energy greater than 11, 14 and 17 GeV and found to be in good agreement with the Monte Carlo predictions, with an exception only for the lowest x_γ^{obs} bins. With the 1996 and 1997 data we are able to extend this measurement up to jets with transverse energy greater than 21, 25 and 29 GeV, as is shown in figure 9.4. At the highest transverse jet energies virtually no energy flow is observed at $|\Delta\eta| > 1$. This means that the measurement of a jet cross section becomes more and more insensitive to issues like underlying events or the jet definition, as the transverse energy of the jets increases.

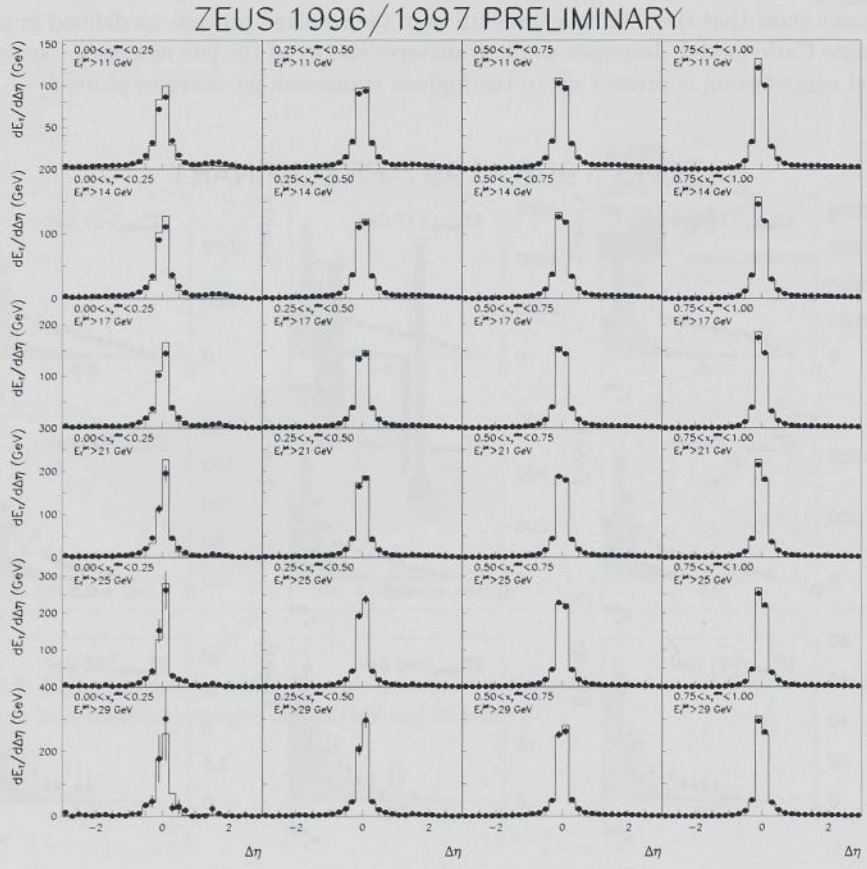

Figure 9.4: The transverse energy flow around jets (integrated over $|\Delta\phi| < 1$), for six thresholds on the transverse energy of the jet and in four bins in x_γ^{obs}. The data are compared to the HERWIG 5.9 predictions. For the data only statistical errors are shown.

9.2.2 Cross sections

The measurement of the dijet cross section as a function of the transverse energy of the leading jet, determined from the combined 1996 and 1997 data, is presented for six ranges of the jet pseudorapidities in figures 9.5 and 9.6. The cross sections have been determined for the full x_γ^{obs} range and for $x_\gamma^{obs} > 0.75$. In comparison to the 1995 measurement one or two transverse energy bins have been added in each pseudorapidity range. The highest transverse energy bin for which the cross section is measured corresponds to 65 GeV $< E_{T\,leading}^{jet} <$ 75 GeV, as compared to 48 GeV $< E_{T\,leading}^{jet} <$ 55 GeV for the 1995 analysis.

The 1996 and 1997 data was also used to determine the cross section as a function of the jet pseudorapidities for different thresholds on the highest transverse energy jet, which has been set at 14 GeV, like in 1995, but also at 17, 21, 25 and 29 GeV. This cross section has been measured for the full x_γ^{obs} range and for $x_\gamma^{obs} > 0.75$, and in two ranges of y. The results for $0.20 < y < 0.85$ and for $0.50 < y < 0.85$ are shown in figure 9.7 and 9.8, respectively. The data are compared to NLO QCD predictions using the CTEQ4M and AFG-HO parametrisations of the proton and the photon structure, respectively. The figures show that the observations made for the measurement with $E_{T\,leading}^{jet} > 14$ GeV also hold at higher transverse energies. For $x_\gamma^{obs} > 0.75$ good agreement is found between data and theory. For the cross section corresponding to the full x_γ^{obs} range the data lies above theoretical predictions at central and forward jet pseudorapidities and in particular for high y.

9.3 Conclusion

We conclude that the increased statistics of the 1996 and 1997 data can be used to measure dijet photoproduction up to transverse energies of around 70 GeV, and to reduce, significantly, the experimental uncertainties in the regions already measured. We stress that the 1996 and 1997 results presented here are preliminary, in particular, no attempt has yet been made to exploit the increase in statistics to also reduce the systematic uncertainties. The final results based on these data will most likely have smaller uncertainties. Moreover, in the year 2000, the HERA collider is planned to undergo a luminosity upgrade, after which HERA is expected to deliver luminosities in the order of 250 pb^{-1} per year. These data will allow for even more precise measurements of dijet photoproduction up to very high transverse energies and in addition for the measurement of various more exclusive processes.

Here we conclude that the discrepancies observed between dijet photoproduction data and theory persist also at high transverse energies, where most theoretical uncertainties are expected to be reduced. Therefore these data pose a theoretical challenge, in particular, the inclusion of these data in NLO QCD fits, used to determine parton density functions in the photon, may provide new information on the hadronic structure of the photon.

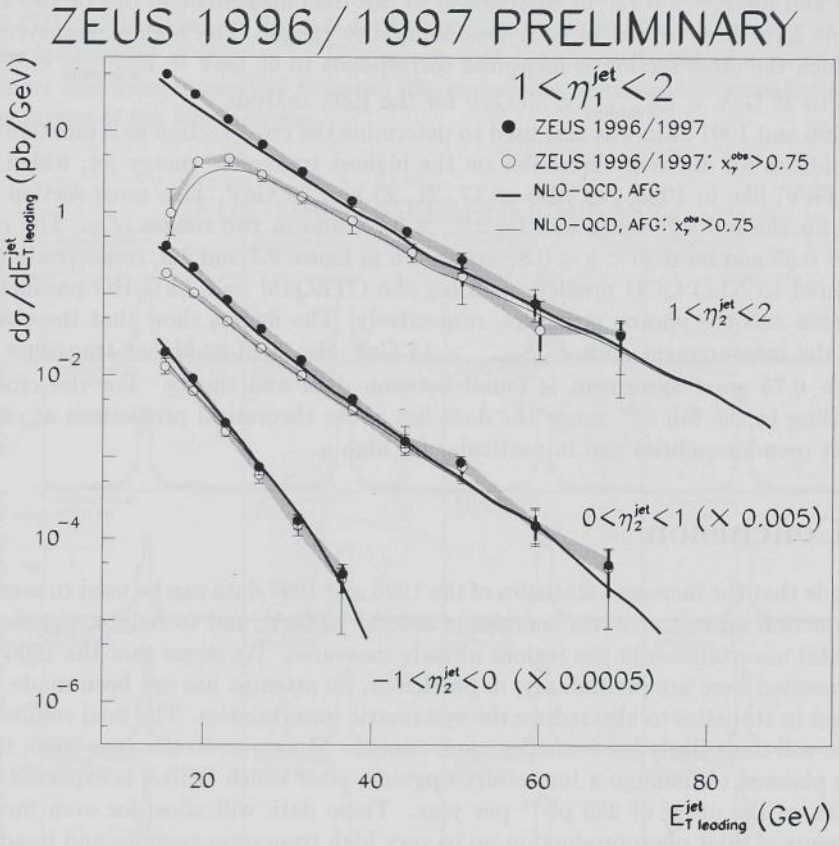

Figure 9.5: Inclusive dijet cross section as a function of $E_{T\,leading}^{jet}$ for η_1^{jet} between 1 and 2, in three regions of η_2^{jet} (as indicated on the plot). For convenience of comparison the results for $-1 < \eta_2^{jet} < 0$ and $0 < \eta_2^{jet} < 1$ have been scaled by the factors indicated on the plot. The filled circles correspond to the entire x_γ^{obs} range while the open circles correspond to events with $x_\gamma^{obs} > 0.75$. The shaded band indicates the uncertainty related to the energy scale. The thick error bar indicates the statistical error and the thin error bar indicates the systematic and statistical errors added in quadrature. The data are compared to NLO QCD calculations, using the AFG-HO parametrisation for the photon structure.

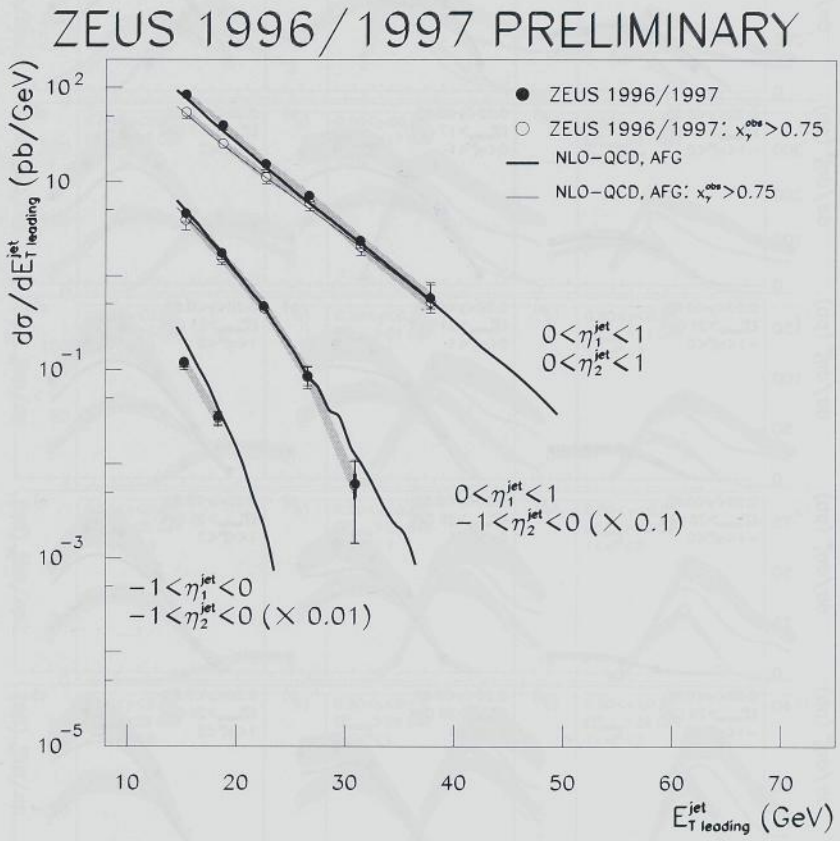

Figure 9.6: Inclusive dijet cross section as a function of $E_{T\,leading}^{jet}$. For the two upper sets of data η_1^{jet} lies between 0 and 1 and for the lower set of data η_1^{jet} lies between -1 and 0. The η_2^{jet} regions are indicated on the plot. For convenience of comparison the two lower sets of data are scaled as indicated on the plot. The filled circles correspond to the entire x_γ^{obs} range while the open circles correspond to events with $x_\gamma^{obs} > 0.75$. The shaded band indicates the uncertainty related to the energy scale. The thick error bar indicates the statistical error and the thin error bar indicates the systematic and statistical errors added in quadrature. The data are compared to NLO QCD calculations, using the AFG-HO parametrisation for the photon structure.

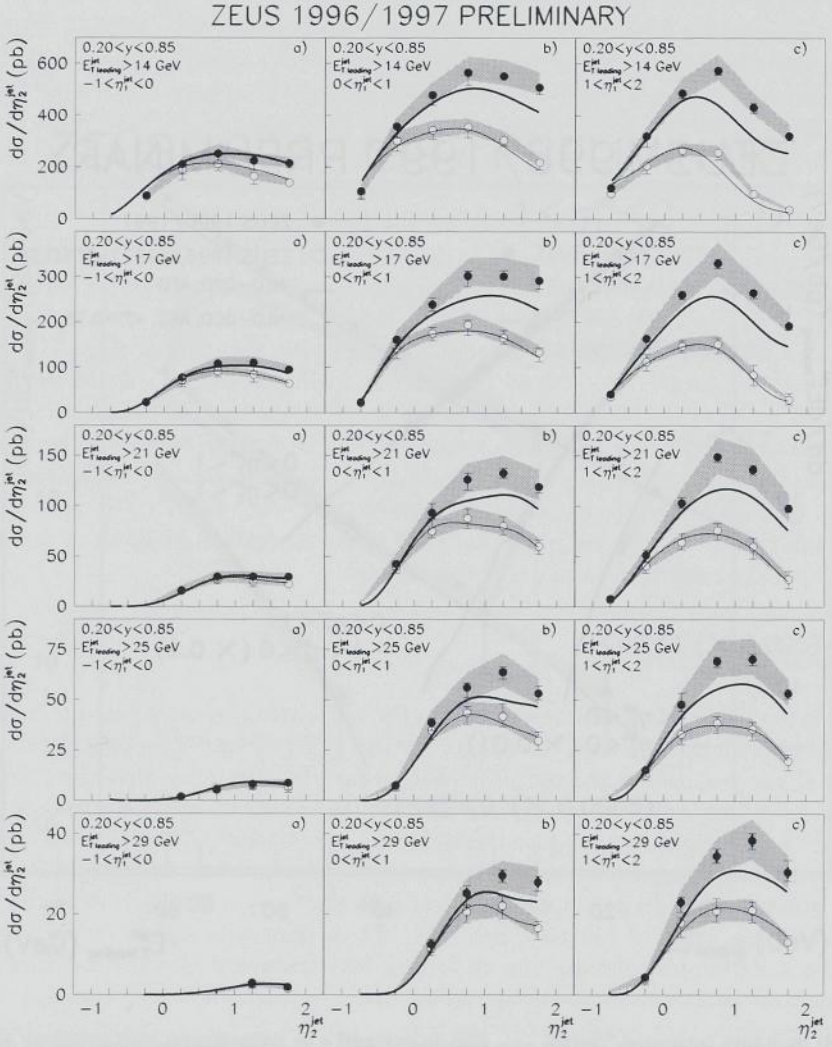

Figure 9.7: Figures a), b) and c) show the dijet cross section as a function of η_2^{jet} in bins of η_1^{jet}. From top to bottom the figures correspond to different thresholds on the highest transverse energy jet which are: 14, 17, 21, 25 and 29 GeV. The filled circles correspond to the entire x_γ^{obs} range while the open circles correspond to events with $x_\gamma^{obs} > 0.75$. The shaded band indicates the uncertainty related to the energy scale. The thick error bar indicates the statistical uncertainty and the thin error bar indicates the systematic and statistical uncertainties added in quadrature. The curves correspond to NLO QCD calculations, using the AFG-HO parametrisation for the photon structure.

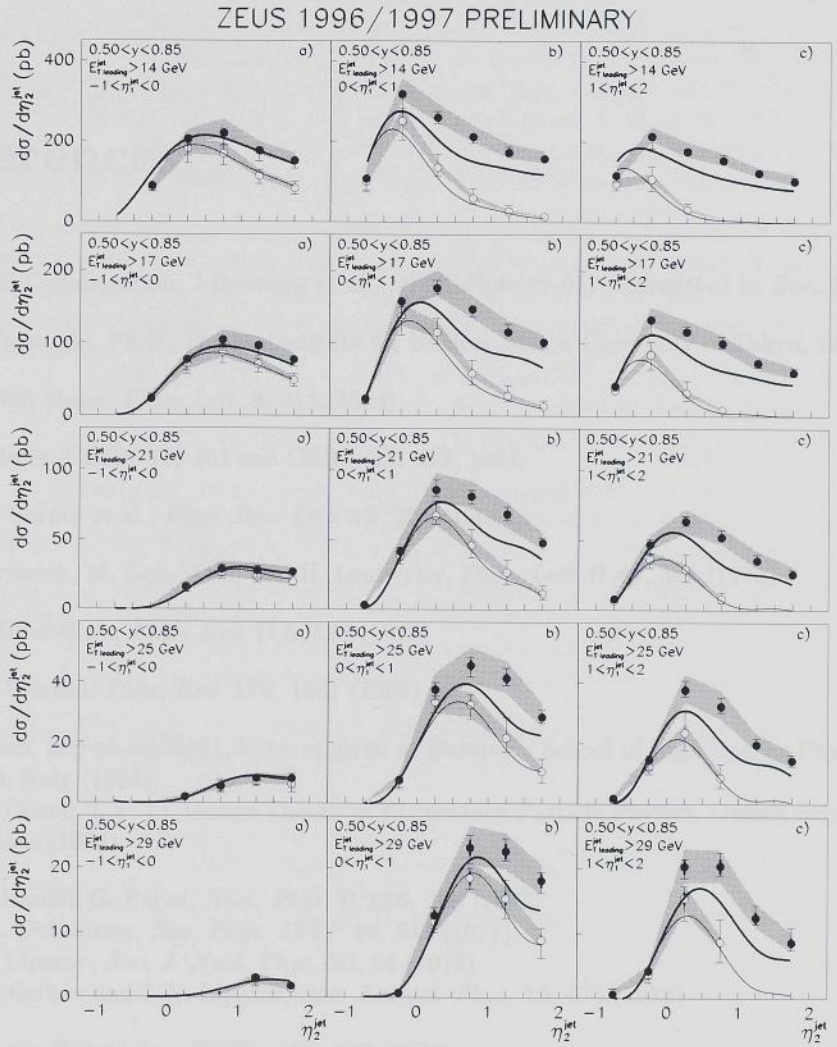

Figure 9.8: Figures a), b) and c) show the dijet cross section as a function of η_2^{jet} in bins of η_1^{jet} and for $0.50 < y < 0.85$. From top to bottom the figures correspond to different thresholds on the highest transverse energy jet which are: 14, 17, 21, 25 and 29 GeV. The filled circles correspond to the entire x_γ^{obs} range while the open circles correspond to events with $x_\gamma^{obs} > 0.75$. The shaded band indicates the uncertainty related to the energy scale. The thick error bar indicates the statistical uncertainty and the thin error bar indicates the systematic and statistical uncertainties added in quadrature. The curves correspond to NLO QCD calculations, using the AFG-HO parametrisation for the photon structure.

References

[1] ZEUS Collaboration, J.Breitweg et al., DESY-Note 99-057, Submitted to *Eur. Phys. J.*

[2] Y. Yamazaki, Ph.D. Thesis, Institute for Nuclear Study, University of Tokyo, 1996

[3] M. Gell-Mann, *Phys. Lett.* **8**, 214 (1964)

[4] G. Zweig, CERN-TH 401 and CERN-TH 412, 1964

[5] V.E. Barnes et al., *Phys. Rev. Lett.* **12**, 204 (1964)

[6] H. Fritzsch, M. Gell-Mann and H. Leutwyler, *Phys. Lett.* B **47**, 365 (1973)

[7] G. Miller et al., *Phys. Rev.* D **5**, 528 (1972)

[8] J.D. Bjorken, *Phys. Rev.* **179**, 1547 (1969)

[9] A. Pich, hep-ph/9505231, lectures given at European School of High Energy Physics, Sorrento, Italy (1994);
T.P. Cheng, L.F. Li, Gauge Theory of Elementary Particle Physics, Oxford Science Publications (1984)

[10] G. Altarelli, G. Parisi, *Nucl. Phys.* B **126**, 298 (1977)
Yu.L. Dokshitzer, *Sov. Phys. JETP* **46**, 641 (1977)
L.N. Lipatov, *Sov. J. Nucl. Phys.* **20**, 94 (1975)
V.N. Gribov and L.N. Lipatov, *Sov. J. Nucl. Phys.* **15**, 675 (1972)

[11] C.F. von Weizsäcker, *Z. Phys.* **88**, 612 (1934);
E.J. Williams, *Phys. Rev.* **45**, 729 (1934);
S. Frixione, M.L. Mangano, P. Nason and G. Ridolfi, *Phys. Lett.* B **319**, 339 (1993)

[12] J.J. Sakurai, *Phys. Rev. Lett.* **22**, 981 (1969)

[13] E. Witten, *Nucl. Phys.* B **120**, 189 (1977)

[14] R.M. Godbole, *Pramana* **51**, 217 (1998)

[15] S. Söldner-Rembold, proceedings of the 13th Lake Louise Winter Institute, 261 (1998)

[16] L3 Collaboration, M. Acciarri et al., *Phys. Lett.* B **436**, 403 (1998);
L3 Collaboration, M. Acciarri et al., *Phys. Lett.* B **447**, 147 (1999);
DELPHI Collaboration, P. Abreu et al., *Z. Phys.* C **69**, 223 (1996);
OPAL Collaboration, K. Ackerstaff et al., *Phys. Lett.* B **412**, 225 (1997);
OPAL Collaboration, K. Ackerstaff et al., *Phys. Lett.* B **411**, 387 (1997);
OPAL Collaboration, K. Ackerstaff et al., *Z. Phys.* C **74**, 33 (1997);
OPAL Collaboration, R. Akers et al., *Z. Phys.* C **61**, 199 (1994)

[17] TOPAZ Collaboration, K. Muramatsu et al., *Phys. Lett.* B **332**, 477 (1994);
AMY Collaboration, T. Kojima et al., *Phys. Lett.* B **400**, 395 (1997);
AMY Collaboration, S.K. Sahu et al., *Phys. Lett.* B **346**, 208 (1995);
AMY Collaboration, T. Sasaki et al., *Phys. Lett.* B **252**, 491 (1990)

[18] TPC/2γ Collaboration, J. Steinman et al., Ph.D. Thesis, UCLA, 1988;
TPC/2γ Collaboration, H. Aihara et al., *Z. Phys.* C **34**, 1 (1987);
TPC/2γ Collaboration, H. Aihara et al., *Phys. Rev. Lett.* **58**, 97 (1987)

[19] CELLO Collaboration, H.J. Behrend et al., *Phys. Lett.* B **126**, 391 (1983);
JADE Collaboration, W. Bartel et al., *Z. Phys.* C **24**, 231 (1984);
JADE Collaboration, W. Bartel et al., *Phys. Lett.* B **121**, 203 (1983);
TASSO Collaboration, M. Althoff et al., *Z. Phys.* C **31**, 527 (1986);
PLUTO Collaboration, Ch. Berger et al., *Nucl. Phys.* B **281**, 365 (1987);
PLUTO Collaboration, Ch. Berger et al., *Phys. Lett.* B **142**, 111 (1984);
PLUTO Collaboration, Ch. Berger et al., *Phys. Lett.* B **107**, 168 (1981)

[20] ZEUS Collaboration, J.Breitweg et al., EPJ **6**, 67 (1999)
ZEUS Collaboration, J.Breitweg et al., *Phys. Lett.* B **401**, 192 (1997)

[21] H1 Collaboration, S. Aid et al., *Nucl. Phys.* B **472**, 32 (1996)

[22] M. Glück, E. Reya and A. Vogt, *Phys. Rev.* D **45**, 3986 (1992)

[23] M. Glück, E. Reya and A. Vogt, *Phys. Rev.* D **46**, 1973 (1992)

[24] Ch. Berger and W. Wagner, *Phys. Rev.* **146**, 1 (1987);
M. Glück, E. Reya and A. Vogt, *Z. Phys.* C **53**, 651 (1992)

[25] L.E. Gordon and J.K. Storow, *Nucl. Phys.* B **489**, 405 (1997)

[26] AMY Collaboration, B.J. Kim et al., *Phys. Lett.* B **325**, 248 (1994);
TOPAZ Collaboration, K. Muramatsu et al., *Phys. Lett.* B **332**, 477 (1994);
TOPAZ Collaboration, H. Hayahashii et al., *Phys. Lett.* B **314**, 149 (1993)

[27] W.A. Bardeen, A.J. Buras, D.W. Duke and T. Muta, *Phys. Rev.* D **18**, 3998 (1978)

[28] P. Aurenche, J. Guillet, M. Fontannaz, *Z. Phys.* C **64**, 621 (1994)

[29] P. Aurenche, R. Baier, M. Fontannaz, M.N. Kienzle-Focacci and M. Werlen, *Phys. Lett.* B **233**, 517 (1989)

[30] ZEUS Collaboration, M.Derrick et al., *Phys. Lett.* B **348**, 665 (1995)

[31] F. Abe et al, *Phys. Rev.* D **45**, 1448 (1992)

[32] S. Catani, Yu.L. Dokshitzer, M.H. Seymour and B.R. Webber, *Nucl. Phys.* B **406**, 187 (1993)

[33] S.D. Ellis and D.E. Soper, *Phys. Rev.* D **48**, 3160 (1993)

[34] M.H. Seymour, hep-ph/9707349, Contributed to 11th Les Rencontres de Physique de la Vallee d'Aoste: Results and Perspectives in Particle Physics, La Thuile, Italy, 2-8 Mar 1997.;
J.M. Butterworth, L. Feld, M. Klasen and G. Kramer, Proceedings of the Workshop "Future Physics at HERA", 554 (1996)

[35] S.D. Ellis, Z. Kunszt and D.E. Soper, *Phys. Rev. Lett.* **69**, 3615 (1992)

[36] M. Klasen, T. Kleinwort and G. Kramer, *Eur. Phys. J.* C **1**, 1 (1998)

[37] G.Marchesini , B.R.Webber, G.Abbiendi, I.G.Knowles, M.H.Seymour and L.Stanco, *Comput. Phys. Commun.* **67**, 465 (1992)

[38] G.Marchesini , B.R.Webber, G.Abbiendi, I.G.Knowles, M.H.Seymour and L.Stanco, hep-ph/9607393

[39] H.U.Bengtsson and T.Sjöstrand, *Comput. Phys. Commun.* **46**, 1987 (43)

[40] T.Sjöstrand, *Comput. Phys. Commun.* **82**, 1994 (74)

[41] H.L. Lai et al., *Phys. Rev.* D **51**, 4763 (1995)

[42] H.L. Lai et al., *Phys. Rev.* D **55**, 1280 (1997)

[43] M. Klasen and G. Kramer, *Z. Phys.* C **76**, 67 (1997)

[44] B.W. Harris and J.F. Owens, *Phys. Rev.* D **56**, 4007 (1997)

[45] S. Frixione, *Nucl. Phys.* B **507**, 295 (1997)

[46] P. Aurenche, L. Bourhis, M. Fontannaz and J.Ph. Guillet, Proceedings of the Workshop "Future Physics at HERA", 570 (1996)

[47] B.W. Harris, M. Klasen and J. Vossebeld, hep-ph/9905348

[48] M. Klasen and G. Kramer, *Z. Phys.* C **72**, 107 (1996)

[49] L.J. Bergmann, Ph.D. Thesis, Florida State University, 1989

[50] S. Frixione, Z. Kunszt and A. Signer, *Nucl. Phys.* B **467**, 399 (1996)

[51] ZEUS Collaboration, M. Derrick et al., *Phys. Lett.* B **342**, 417 (1995)

[52] H1 Collaboration, S. Aid et al., *Z. Phys.* C **70**, 17 (1996)

[53] ZEUS Collaboration, J.Breitweg et al., *Eur. Phys. J.* C **1**, 109 (1998)

[54] ZEUS Collaboration, J.Breitweg et al., *Eur. Phys. J.* C **4**, 591 (1998)

[55] ZEUS Collaboration, J. Breitweg et al., *Phys. Lett.* B **443**, 394 (1998)

[56] M. Klasen and G. Kramer, *Phys. Lett.* B **366**, 385 (1996)
S. Frixione and G. Ridolfi, *Nucl. Phys.* B **507**, 315 (1997)

[57] W.T. Giele, E.W.N. Glover and D.A. Kosower, *Phys. Rev. Lett.* **73**, 2019 (1994)

[58] B.W. Harris and J.F. Owens, *Phys. Rev.* D **57**, 5555 (1998)

[59] M. Klasen, G. Kramer, S.G. Salesch, *Z. Phys.* C **68**, 113 (1995)

[60] BCDMS Collaboration, A.C. Benvenuti et al., *Phys. Lett.* B **223**, 485 (1990);
NMC Collaboration, M. Arneodo et al., *Nucl. Phys.* B **483**, 3 (1997);
H1 Collaboration, S. Aid et al., *Nucl. Phys.* B **470**, 3 (1996);
ZEUS Collaboration, M. Derrick et al., *Z. Phys.* C **72**, 399 (1996)

[61] CDF Collaboration, F. Abe et al., *Phys. Rev. Lett.* **77**, 438 (1996);
DØ Collaboration, B. Abbott et al., *Phys. Rev. Lett.* **82**, 2451 (1999);
CDF Collaboration, F. Abe et al., *Phys. Rev. Lett.* **70**, 1376 (1993)

[62] G.C. Blazey, FERMILAB-CONF-98-367-E, To be published in the proceedings of the 29th ICHEP conference, Vancouver, Canada, 1998;
G.C. Blazey and B.L. Flaugher, FERMILAB-PUB-99-038-E, Submitted to *Ann. Rev. Nucl. Part. Sci.*;
J. Huston, hep-ph/9901352, To be published in the proceedings of the 29th ICHEP conference, Vancouver, Canada, 1998.

[63] A.D. Martin, R.G. Roberts, W.J. Stirling and R.S. Thorne, *Eur. Phys. J.* C **4**, 463 (1998)

[64] The ZEUS Detector, Status Report (1993), DESY 1993

[65] N. Harnew et al., *Nucl. Instrum. Methods* A **279**, 290 (1989)
B. Foster et al., *Proc. Suppl. Nucl. Phys.* B **32**, 181 (1993)
B. Foster et al., *Nucl. Instrum. Methods* A **338**, 254 (1994)

[66] ZEUS Collaboration, M.Derrick et al., *Nucl. Instrum. Methods* A **309**, 77 (1991)

[67] A. Andresen et al., *Nucl. Instrum. Methods* A **309**, 101 (1991);
A. Bernstein et al., *Nucl. Instrum. Methods* A **336**, 23 (1993)

[68] ZEUS Presampler Group, *Nucl. Instrum. Methods* A **382**, 419 (1996)

[69] H. Bethe and W. Heitler, *Proc. Roy. Soc.* A **146**, 83 (1934)

[70] M. van der Horst, Ph.D. Thesis, University of Amsterdam, 1990

[71] L. Suszycki et al., Proceedings of the HERA workshop, 1987, Vol. 2, 505.

[72] G. Briskin and A. Caldwell, ZEUS-Note 95-035;
M. Vreeswijk, Ph.D. Thesis, University of Amsterdam, 1996

[73] G.M. Briskin, Ph.D. Thesis, Tel Aviv University, 1998

[74] F. Jacquet, A. Blondel, Proceedings of the Study of an *ep* Facility for Europe, DESY-Note 79-048 (1979) 391

[75] S. Bentvelsen, J. Engelen, P. Kooijman, Proceedings of the Workshop on Physics at HERA, DESY (1992), 23.

[76] CERN Application Software Group, CERN Program Library Long Writeup D506

[77] H. Abramowicz, A. Caldwell and R. Sinkus, *Nucl. Instrum. Methods* A **365**, 508 (1995)

Summary

In this thesis, we have presented an analysis of dijet photoproduction, based on data collected with the ZEUS detector in 1995. In performing the analysis, which refers to jets with relatively high transverse energies, care has been taken to minimise the theoretical uncertainties involved in the comparison of theory and experiment. These uncertainties, which include: fragmentation effects, jet finding, scale uncertainties and underlying events, have been studied and were found to be under control (typically less than 10%), in most of the kinematic region of the measurement, presented in this thesis.

To improve on the experimental precision obtained in earlier measurements, a new method was applied to reconstruct kinematic variables. This method involves the use of combined information from the ZEUS calorimeter and inner tracking detectors. To correct for energy losses in materials in front of the calorimeter, we have determined energy correction functions from a kinematically constrained fit to NC-DIS events, exploiting the transverse momentum balance between the scattered positron and the hadronic final state.

Event selection cuts have been applied to a sample of dijet candidate events selected at the trigger level. As a result, 8690 dijet photoproduction candidates were selected. The contamination of background processes in this sample was found to be negligible. The selected events are compared to simulated events, produced with photoproduction Monte Carlo programs. Good agreement is found in the shape of various distributions. The normalisation of the cross section is not correctly described, which is expected since the Monte Carlo models include only the leading order matrix elements. The Monte Carlo events are used mainly for the unfolding of the cross section and for the study of systematic effects. For these purposes the agreement of the shapes of the differential cross sections is more important than the agreement of the normalisations. The distributions of x_γ^{obs}, the fractional momentum of the photon participating in the hard interaction, and of transverse energy flows, indicate that the kinematic region chosen for this analysis successfully avoids the region were underlying events affect the measurement. It is also shown that a subsample, strongly enriched with direct photoproduction events, can be selected by requiring $x_\gamma^{obs} > 0.75$.

The cross sections obtained have been confronted with next-to-leading order quantum chromodynamics (NLO QCD) calculations. In general, these calculations give a fairly good description of the data. In particular, for a subsample of events with $x_\gamma^{obs} > 0.75$, data and theory are in good agreement. However, for the full data sample, when the jets have forward or central pseudorapidities, the measured cross sections are above the calculations by up to 30%. This difference becomes even larger when we study the cross section in a restricted kinematic region, where $0.50 < y < 0.85$. The observed discrepancies are much larger than the experimental uncertainties and are also larger than the estimated theoretical uncertainties. It is possible that

they are due to the parametrisations of parton density functions of the photon, being too low in the kinematic region studied. These parton density functions, which are used in the NLO QCD calculations, have been determined by different theoretical groups in fitting procedures to available F_2^γ and $\gamma\gamma^* \longrightarrow jets$ data. These data do not cover the same range in x_γ and correspond to a different factorisation scale, μ_f, as the present study. It must be stressed, however, that parton density functions in different regions of x_γ and μ_f are not independent.

One of the conclusions of this thesis, therefore, is that the procedures to determine the parametrisation of the photon structure should be repeated with the data of the present measurement included. This exercise will establish: a) whether our measurements can be described by NLO QCD once the parton density functions in the photon are modified and b) whether these modifications can be made without spoiling the agreement with existing earlier data, in particular from e^+e^- experiments.

We point out here that long range correlations play an important role in jet photoproduction. For the dijet measurement presented in this thesis we have investigated various non-perturbative effects and found the sensitivity to these effects to be under control. Nevertheless, as yet, our understanding of this type of effects is still limited. Improvements to this understanding are of great importance for the comparisons made between jet photoproduction measurements and the corresponding theoretical predictions.

This thesis ends with an outlook towards the future. With the increasing luminosity delivered by HERA each year, the experimental uncertainty on photoproduction jet measurements will be further reduced, while the kinematic range covered in these measurements will be extended to higher transverse energies. A preliminary analysis of the data collected in 1996 and 1997, presented in the last chapter, shows that the observed discrepancy between data and theory persists up to higher transverse energies, where we believe long range correlation effects to be further reduced. As the discrepancies between data and theory are large, the measurement constitutes a challenge to theory. In particular, the inclusion of these data in NLO QCD fits, used to determine parton density functions in the photon, may provide new information on the hadronic structure of the photon.

Samenvatting

De in dit proefschrift gepresenteerde analyse van twee-jet fotoproductie, is gebaseerd op data verzameld in 1995 met de ZEUS detektor. Bij het uitvoeren van de analyse, die betrekking heeft op jets met relatief hoge transversale energieën, is veel zorg besteed aan het onderdrukken van de theoretische onzekerheden die een rol spelen bij het vergelijken van meting en theorie. Deze onzekerheden, waaronder: fragmentatie effecten, jet definities, schaal-onzekerheden en onderliggende botsingen, zijn bestudeerd en blijken, in het grootste gedeelte van het kinematische gebied waarop de gepresenteerde meting betrekking heeft, onder controle te zijn (typisch minder dan 10%).

Om de experimentele precisie, bereikt in eerdere metingen, te verbeteren, is een nieuwe methode toegepast voor de reconstructie van de kinematische variabelen. Deze methode behelst het combineren van informatie van de ZEUS calorimeter en dradenkamers. Voor de correctie van energieverlies van deeltjes in inaktief materiaal voor de calorimeters, hebben we energie-correctiefuncties bepaald middels een kinematische aanpassing aan diep inelastische positron proton botsingen, gebruik makende van de balans tussen de transversale impuls van het verstrooide positron en de hadronische eindtoestand.

Selectiesneden zijn toegepast op een verzameling twee-jet kandidaat-botsingen, geselecteerd met behulp van het ZEUS trigger systeem. Dit resulteert in 8690 twee-jet fotoproductie kandidaten. De verontreiniging van deze verzameling botsingen door achtergrond processen is verwaarloosbaar. De geselecteerde botsingen zijn vergeleken met gesimuleerde botsingen die geproduceerd zijn met Monte Carlo programma's. De vorm van diverse verdelingen is in overeenkomst met die van de Monte Carlo verdelingen. Voor de normalisatie van de werkzame doorsneden is dit niet het geval. Dit laatste is volgens verwachting, aangezien de Monte Carlo programma's slechts de matrixelementen in laagste orde bevatten. De Monte Carlo botsingen worden hoofdzakelijk gebruikt voor het ontvouwen van de werkzame doorsneden en voor het bestuderen van systematische onzekerheden. Hiervoor is de beschrijving van de vorm van de differentiële werkzame doorsneden meer van belang dan de correcte beschrijving van de normalisatie. De verdelingen in x_γ^{obs}, de fractionele impuls van het foton die bijdraagt aan de harde wisselwerking, en van transversale energie, geven aan dat het voor deze analyse gekozen kinematische gebied met succes het gebied, waar onderliggende botsingen de meting beïnvloeden, vermijdt. De distributie in x_γ^{obs} laat tevens zien dat door te eisen dat $x_\gamma^{obs} > 0.75$ een verzameling botsingen geselecteerd kan worden die sterk verrijkt is met direkte fotoproductie botsingen.

De werkzame doorsneden zijn vergeleken met hogere orde quantum chromodynamica (NLO QCD) berekeningen. In het algemeen geven deze berekeningen een tamelijk goede beschrijving van de data. Met name voor botsingen waarbij $x_\gamma^{obs} > 0.75$, is de overeenkomst tussen data en theorie goed. Voor de gehele verzameling data geldt echter dat, als de jets voor-

waarts geproduceerd worden, de gemeten werkzame doorsneden tot 30% procent hoger zijn dan de berekeningen. Dit verschil wordt nog groter als een begrensd kinematische gebied met $0.50 < y < 0.85$ wordt bestudeerd. De waargenomen verschillen zijn aanzienlijk groter dan de experimentele onzekerheden en zijn tevens groter dan de geschatte theoretische onzekerheden. Een mogelijke oorzaak van deze verschillen zou kunnen zijn dat de parametrisaties van de parton-verdelingsfuncties in het foton te lage waarden geven in het bestudeerde kinematische gebied. Deze parton-verdelingsfuncties, die gebruikt worden in de NLO QCD berekeningen, zijn bepaald door verschillende theoretische groepen middels aanpassings procedures aan beschikbare F_2^γ en $\gamma\gamma^* \longrightarrow jets$ data. Deze data hebben betrekking op een ander gebied in x_γ en een andere factorisatieschaal, μ_f, dan de hier gepresenteerde meting. Het moet echter ook benadrukt worden dat parton-verdelingsfuncties bij verschillende waarden van x_γ and μ_f niet onafhankelijk zijn.

Eén van de conclusies van dit proefschrift is daarom dat de procedures die gebruikt worden om parametrisaties van de parton-verdelingsfuncties in het foton te bepalen herhaald zouden moeten worden, met medeneming van de hier gepresenteerde resultaten. Deze exercitie zal duidelijk maken: a) of onze metingen beschreven kunnen worden door NLO QCD wanneer de parton-verdelingsfuncties in het foton worden aangepast en b) of deze aanpassingen gemaakt kunnen worden zonder de beschrijving van reeds bestaande resultaten te bederven, in het bijzonder de beschrijving van resultaten van e^+e^- experimenten.

We wijzen erop dat niet-perturbatieve effecten een belangrijke rol spelen in de fotoproductie van jets. Voor de gepresenteerde twee-jet meting, hebben we diverse niet perturbatieve effecten onderzocht en gevonden dat de gevoeligheid voor deze effecten beheersbaar is. Desalniettemin, is ons begrip van dit type effecten vooralsnog begrensd. Verdieping van dit begrip is van groot belang voor het vergelijken van jet fotoproductiemetingen en de bijbehorende theoretische voorspellingen.

Dit proefschrift eindigt met een blik naar de toekomst. Met behulp van de toenemende luminositeit die elk jaar geleverd word door HERA, kan de experimentele onzekerheid in jet fotoproductiemetingen verder gereduceerd worden, terwijl het kinematische gebied bestreken door deze metingen uitgebreid kan worden naar hogere transversale energieën. Een voorlopige analyse van data verzameld in 1996 en 1997, die is gepresenteerd in het laatste hoofdstuk, laat zien dat de waargenomen discrepantie tussen data en theorie aanhoudt bij hogere transversale energieën, waar we aannemen dat niet-perturbatieve effecten verder gereduceerd zijn. Aangezien de waargenomen discrepanties tussen data en theorie groot zijn, vormen deze metingen een uitdaging aan het adres van de theorie. In het bijzonder is het mogelijk dat het meenemen van deze data in NLO QCD aanpassingen, die gebruikt worden om parton-verdelingsfuncties in het foton te bepalen, nieuwe informatie zal verschaffen over de hadronische structuur van het foton.

Acknowledgements

The work presented in this thesis was performed in a collaboration consisting of many people from different institutes around the world. Without the effort of these people the results could never have been obtained. I therefore thank all my colleagues in ZEUS, not only for their efforts to build, operate and exploit the ZEUS detector, but also for the pleasant collaboration I enjoyed in the past four years.

Many thanks also to my colleagues in the Nikhef ZEUS group, which I think is an exceptionally pleasant group to work in. It has been great fun to work with you in the past four years. In particular I would like to express my gratitude towards my promotor Jos Engelen and co-promotor Henk Tiecke, for hiring me in the first place and for the valuable guidance they have given me in my work, to Paul Kooijman and Nichol Brümmer from both of whom I have learned a lot on physics and data analysis in many useful discussions. I also thank Wouter Verkerke who taught me all I needed to know about the Nikhef high voltage system used for various detectors in ZEUS and Niels Tuning for smoothly taking over the responsibility for this system from me again.

From the people at DESY I would like to thank Stefan Schlenstedt for our pleasant collaboration on the ZEUS F and RCAL presamplers. Many thanks also to all other members of the presampler group. I owe a great debt of gratitude also to Yuji Yamazaki, who has performed the analysis parallel to the one presented in this thesis. In his own PhD thesis he laid the basis for the measurement presented in this thesis. I have profitted a great deal from his experience and insight into both theoretical and experimental issues. I would also like to thank the coordinators from the ZEUS jets group (known under various names during the past four years), in particular Costas Foudas, Laurel Sinclair and Juan Terron, for their strong guidance and support and Matthew Wing who has made a large effort performing an analysis parallel to the one presented in chapter 9; thanks to this we were allowed to present these measurements as a preliminary result at the 1999 EPS conference. Finally, I thank all others who also contributed to the jets group during the past four years.

I would also like to express my gratitude towards: Michael Klasen, Brian Harris, Stefano Frixione and Michel Fontannaz, first of all for providing the NLO QCD predictions to which we have compared our data, but also for their effort to solve theoretical problems and their preparedness to enlighten me on various theoretical issues.

Finally I would like to thank my parents for the encouragement and support, they have never ceased to give me. Thanks!